THÈSE

Pour obtenir le grade de

DOCTEUR DE L'UNIVERSITÉ GRENOBLE ALPES

Spécialité : Physique de la Matière Condensée et du Rayonnement

Arrêté ministériel : 25 mai 2016

Présentée par

Vitalii KUZNETSOV

Thèse dirigée par **Peter FOUQUET**, Institut Laue-Langevin
et co-encadrée par **Franziska TRAEGER**, Westfälische Hochschule

préparée au sein du **Laboratoire Institut LAUE LANGEVIN**
dans **l'École Doctorale Physique**

Dynamique d'hydrogène dans des réactions élémentaires sur des composés de molybdène

HYDROGEN DYNAMICS IN ELEMENTARY REACTIONS ON MOLYBDENUM COMPOUNDS

Thèse soutenue publiquement le **6 avril 2022**,
devant le jury composé de :

Monsieur PASCAL BRAULT
Directeur de recherche, CNRS CENTRE LIMOUSIN POITOU-CHARENTES, Rapporteur
Monsieur GIL ALEXANDROWICZ
Professeur, Swansea University, Rapporteur
Madame JUDITH PETERS
Professeur des Universités, UNIVERSITE GRENOBLE ALPES, Présidente
Monsieur STEWART PARKER
Docteur en sciences, Rutherford Appleton Laboratory, Examinateur
Madame HOLLY HEDGELAND
Docteur en sciences, University of Cambridge, Examinatrice

Abstract

The design of novel and abundant catalytic materials for water electrolysis is crucial for reaching the carbon neutrality of the global energy system. A deliberate approach to this problem requires both theoretical and experimental knowledge not only of the target reactions, but also of the supplementary mechanisms affecting the catalytic activity. The doctoral project is aimed at revealing the diffusion patterns of hydrogen inside molybdenum sulphide, a promising candidate for the catalysis of the hydrogen evolution reaction. Water electrolysis process, in a broad sense, involves interaction of the catalyst with various hydrogen species, therefore, this study covers not only atomic hydrogen dynamics, but also hydrogen molecules and water. Complementary techniques were utilised in this study to obtain a broad picture from different perspectives. Neutron spectroscopy, supported by molecular dynamics simulations, revealed the picture of hydrogen motion within the bulk of MoS_2. X-ray photoelectron spectroscopy provided information on the hydrogen reaction with the surface, affected also by the bulk H migration towards the surface. Nuclear reaction analysis uncovered hydrogen mobility perpendicular to the basal planes and in longer time-frames. Cyclic and linear voltammetry gave information on the catalytic efficiency.

It was found that hydrogen atoms in MoS_2 diffuse relatively fast with diffusion coefficient $D \approx 1 \cdot 10^{-9}\ m^2/s$. However, room or elevated temperatures are required to induce this migration, which is connected also with the known facility of formation of sulphur vacancies in this material. H_2O molecules cannot traverse the perfect MoS_2 matrix, but are found within volume defects, like voids or cracks. This is essential for water electrolysis, since it shows that H_2O can access the regions where a higher density of edge, and hence, reactive sites is to be anticipated. The MoS_2 crystals, loaded with hydrogen via electrolysis, showed the presence of large quantity of H_2 molecules, formed via recombination in the bulk, which exhibited the fastest observed dynamics among the examined species. Classical molecular dynamics simulations, along with the literature reports, suggest that layer shearing could play an important role in the overall hydrogen transport.

Résumé

La conception de matériaux catalytiques nouveaux et abondants pour l'électrolyse de l'eau est cruciale pour atteindre la neutralité carbone du système énergétique mondial. Une approche délibérée de ce problème nécessite une connaissance à la fois théorique et expérimentale non seulement des réactions cibles, mais également des mécanismes supplémentaires affectant l'activité catalytique. Le projet doctoral vise à révéler les schémas de diffusion de l'hydrogène à l'intérieur du sulfure de molybdène, un candidat prometteur pour la catalyse de la réaction de dégagement d'hydrogène. Le processus d'électrolyse de l'eau, au sens large, implique l'interaction du catalyseur avec diverses espèces d'hydrogène, par conséquent, cette étude couvre non seulement la dynamique de l'hydrogène atomique, mais également les molécules d'hydrogène et l'eau. Des techniques complémentaires ont été utilisées dans cette étude pour obtenir une vue d'ensemble à partir de différentes perspectives. La spectroscopie neutronique, appuyée par des simulations de dynamique moléculaire, a révélé l'image du mouvement de l'hydrogène dans le MoS_2. La spectroscopie photoélectronique à rayons X a fourni des informations sur la réaction de l'hydrogène avec la surface, également affectée par la migration de H vers la surface. L'analyse de la réaction nucléaire a révélé la mobilité de l'hydrogène perpendiculairement aux plans basaux et dans des délais plus longs. La voltamétrie cyclique et linéaire a donné des informations sur l'efficacité catalytique.

Il a été constaté que les atomes d'hydrogène dans MoS_2 diffusent relativement rapidement avec un coefficient de diffusion $D \approx 1 \cdot 10^{-9}\ m^2/s$. Cependant, des températures ambiantes ou élevées sont nécessaires pour induire cette migration, qui est également liée à la facilité connue de formation de lacunes de soufre dans ce matériau. Les molécules H_2O ne peuvent pas traverser la matrice MoS_2 parfaite, mais se trouvent dans des défauts volumiques, comme des vides ou des fissures. Ceci est essentiel pour l'électrolyse de l'eau, car cela montre que H_2O peut accéder aux régions où une densité plus élevée de sites de bord, et donc réactifs, est à prévoir. Les cristaux de MoS_2, chargés d'hydrogène par électrolyse, ont montré la présence d'une grande quantité de molécules de H_2, formées par recombinaison dans la masse, qui présentaient la dynamique observée la plus rapide parmi les espèces examinées. Les simulations classiques de dynamique moléculaire, ainsi que les rapports de la littérature, suggèrent que le cisaillement des couches pourrait jouer un rôle important dans le transport global de l'hydrogène.

Acknowledgements

During the course of this PhD project I have worked with a lot of wonderful people. Many of them directly contributed to the success of this work, and here I would like to express my sincere gratitude to each one of them.

I am thankful to my supervisors, Peter Fouquet and Franziska Traeger, who have been a great help in my scientific life. Since the very start Peter has put me on a right track to dive into the world of neutron spectroscopy, and Franziska patiently answered all of my chemistry related questions, even silly ones. There were so many new things I had to grasp, and my supervisors were always there to help me.

A large part of this work is the result of complex experiments, which cannot be carried out without the assistance from a local instrument responsible. Hence I would like to thank Alexei Nefedov, Norbert Kazamer, Michael Marek Koza, Detlef Rogalla, Hans-Werner Becker, Thomas Strunskus, Eva Kovacevic, Wiebke Lohstroh, Andrea Jagodar, Monica Jimenez Ruiz, Andrea Piovano, Thomas Hansen, Manon Letiche and Ketty Beauvois for their assistance.

My special acknowledgements go to Leran Lu and Alexander Graf for being valuable members of this project. Alexander was involved in electrochemical study of MoS_2 crystals, and Leran was the driving force in the MD simulations. Without Leran the MD part of this work would have never existed, because I did not have enough time to do it on my own. Big thanks to Leran.

I am grateful to Judith Peters, Gil Alexandrowicz, Pascal Brault, Stewart Parker and Holly Hedgeland for agreeing to be members of the jury, and for taking their time to read my manuscript and give extremely valuable comments which contributed significantly to the cleanness, readability and overall quality of the text.

Last but not least, I want to thank my family and friends for keeping a nice company along this journey, especially during the lockdown times. It would be impossible to keep up the good work without their encouragement, support and laughter. Thank you all!

P.S. and thank you, fellow reader. A thesis is meant to be read to spread the knowledge, and you help it fulfil its purpose.

Contents

Acronyms

CV	Cyclic Voltammetry
DDCS	Double differential cross section
DFT	Density functional theory
EISF	Elastic incoherent structure factor
HER	Hydrogen evolution reaction
HWHM	Half-width-at-half-maximum
ILL	Institut Laue-Langevin
LV	Linear Voltammetry
MD	Molecular dynamics
NRA	Nuclear reaction analysis
NSE	Neutron spin echo
QENS	Quasi-elastic neutron scattering
TOF	Time-of-flight
UHV	Ultra-high vacuum
XPS	X-ray photoelectron spectroscopy

Chapter 1

Introduction

Nowadays the harmful impact of the ubiquitous fossil fuel exploitation on our planet becomes evident [1–4]. Fortunately this problem is not left aside, and a lot of advancement has already been made during the last years, both from a technological and social point of view [5]. Wind farms rise everywhere, solar panels are widely used, the use of electric vehicles and public transport is being promoted in the majority of developed countries and people become more conscious about their consumption. However, there still exist some fundamental problems that grow together with the industry, and which may become the stumbling block for future development of green energy. Obviously, weather based renewable resources are too irregular to cover the usually predictable and well time-structured electricity demands of any city. This unavoidably requires us to store energy in some convenient and rational way. No doubt, still rechargeable batteries, and Li-ion batteries in particular, yield the best results in terms of energy storage and release [6, 7]. State-of-the-art accumulators are already on the track to achieve a close to 100 % coulombic efficiency[1] [8]. Nevertheless, such remarkable properties come at a price, and in case of Li based accumulators the flow is literally the monetary price [6]. A large scale deployment of Li-ion batteries for the storage of an ever increasing amount of produced renewable energy would result in enormous demands for lithium. Moreover, the latter should also be produced utilising renewable sources, or else CO_2 costs of its production

[1] Coulombic efficiency or Faraday efficiency - applied to accumulators it shows the ratio of charge generated by the battery during discharging to the total charge inserted into it during charging. In other words, how much less electricity can a battery give us, compared to what we spent on charging.

could diminish the plausible effect of its exploitation. Therefore a search for another energy carrier, more suitable for city-scale electricity needs in terms of its monetary and environmental costs, energy density and transportation ease, is well under way.

One of the promising techniques is energy storage in form of hydrogen gas [9]. Within this concept H_2 gas is usually generated via electrolysis from water with added electrolyte. The produced gas can then be stored in a hydrogen tank for an extended period of time. Although there are still debates about safety of hydrogen storage under high pressure [10], which is required in order to increase energy density, numerous storage solutions are already displayed on the market[2]. At the same time, petrol and car batteries are not 100 % safe either and may cause a fire or an explosion [11], however, they are widely used. The transportation of hydrogen to the end user has several implementation problems if brought to a country's energy demands scale [12], but they are realised and being dealt with. In general, there are two main means of hydrogen transport, namely, in a tube trailer, for a close reach, or via pipeline, over long distances. The ordinary pipelines for natural gas are not really suited for hydrogen, because of its small molecular size, which would cause heavy leaks. However, with mild modifications it is possible to transfer 20/80 % blend of H_2/natural gas [12]. Transportation of pure hydrogen gas over large distances is an existing issue, and it is not yet realised whether it would be more cost efficient to rework the existing pipeline system, or to create a new one.

Reconversion of hydrogen back into electricity can be carried out in a so called fuel cell. In it, incoming hydrogen gas is combined with oxygen from air to generate electricity and water, which is a reverse operation to electrolysis, where under applied potential water is split into hydrogen and oxygen molecules. Fuel cells are available in different sizes, including the ones compact enough to be used in electric vehicles. Given the aforementioned developments, it may look like most of the constituents of hydrogen economy are already there and ready to be deployed, but the major issue lies in the efficiency of the process. Modern fuel cell vehicles run with approximately 60 % efficiency [13]. Combined with around 80 % maximum achieved low temperature electrolysis efficiency [14], the full cycle performance barely reaches 50 %. This value is too small considering the distribution of energy consumption in European Union [15], and must be increased. One

[2]for example: https://www.mahytec.com/en/compressed-hydrogen-storage/

of the main directions for technological enhancement is the development of catalysts for both electrolysis and fuel cells, which we will discuss further in details.

The chemical reactions occurring in a fuel cell are called the oxygen reduction reaction (ORR):

$$Cathode : O_2 + 4H^+ + 4e^- \rightarrow 2H_2O, \tag{1.1}$$

and the hydrogen oxidation reaction (HOR):

$$Anode : H_2 \rightarrow 2H^+ + 2e^-. \tag{1.2}$$

In electrolysis the corresponding processes are the hydrogen evolution reaction (HER):

$$Cathode : 2H^+ + 2e^- \rightarrow 2H_2, \tag{1.3}$$

and the oxygen evolution reaction (OER):

$$Anode : 2H_2O \rightarrow O_2 + 4H^+ + 4e^-. \tag{1.4}$$

For both reactions the conventional catalyst is platinum due to its great performance. However, Pt is also rather expensive [16] and can barely be considered for industrial use in its pure form. Therefore, not surprisingly a large number of academic works are devoted to a search for Pt-based catalysts, which would be, at the same time, more active and less costly due to substitution/intercalation of other elements and various structure modifications [17]. Nevertheless, this approach, apparently, is not the only one. Even if a close to 100 % efficiency is achieved with some Pt-based catalyst, it still remains expensive and its use will probably be targeted at several specific areas where efficiency and size are the major factors, as it is in the fuel cells for cars. In case of a large-scale industry, like hydrogen production from renewable sources, a less active and much more readily available catalyst is favourable. Investigations towards this direction are also under way, and different materials for water electrolysis are studied [18, 19]. Among a number of candidates two can be highlighted, MoS_2 and Mo_2C. Both are commercially available in large quantities, both have shown promising behaviour versus the hydrogen evolution reaction and both are actively studied [18, 20–25]. However, structure-wise the two materials are completely different. Molybdenum disulphide possesses a layered internal arrangement, which promotes its flexibility towards structural modifications. The most frequently occurring MoS_2

formation consists of a number of hexagonally stacked sandwich-like S-Mo-S layers, bound with each other by van-der-Waals forces with an interlayer distance of ≈2 Å [26] (Fig. 1.1). Mo_2C is isostructural to tungsten carbide and has an orthorhombic *Pbcn* unit cell [27]. In this work more emphasis will be given to MoS_2 because of several reasons. First, the understanding of its catalytic activity is well advanced, as MoS_2 has been used in a role of a catalyst for hydrogenation reactions since decades, and has been studied ever since [28]. Second, some of the utilised methods, which will be discussed later, are designed to yield geometrically resolved information, and a layered material is better suited to make use of this feature.

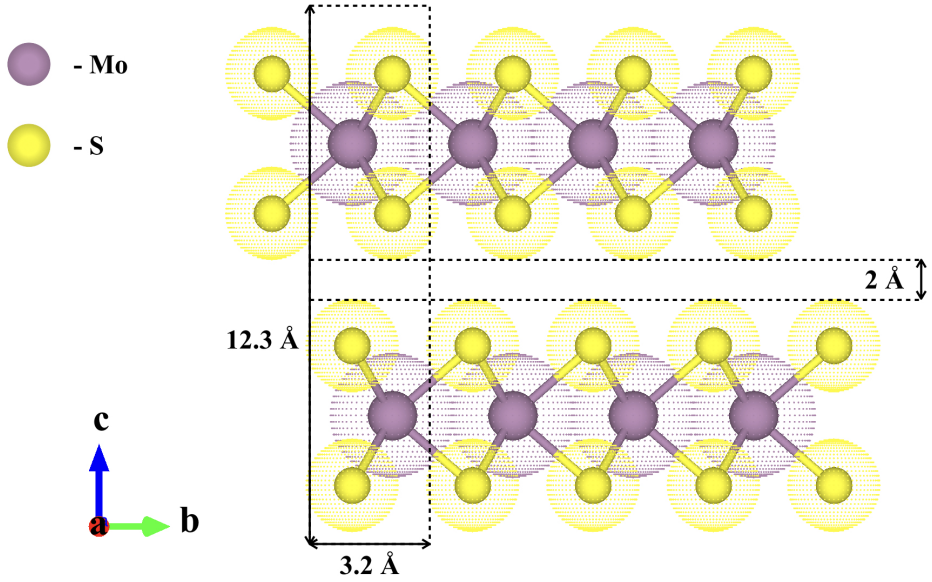

Fig. 1.1: A representation of the structure of 2H MoS_2, view from the side. Molybdenum atoms are coloured purple and sulphur atoms are yellow. The dot surfaces indicate atomic (covalent) radii of the corresponding particles.

Considering the catalytic activity of a compound for electrolysis, there are, in general, two ways to assess it. One is macroscopic, and consists of manufacturing of an electrode with the powder under study and testing its electrochemical activity. This method gives direct measures of catalyst's performance, however, it is largely influenced by a number of factors, such as the quality of an electrode, the choice of electrolyte and the arrangement

of electrodes, to name a few[3]. So in this case the overall environment of the catalyst also plays a role, and some materials may yield poor performance not because of the intrinsic properties, but because of an unsatisfactory polishing of a substrate, for instance. The other technique is microscopic and includes numerical simulations, and density functional theory (DFT) calculations in particular. Obviously, in this case the system under study can be easily modified and a large number of different arrangements/compositions can be investigated. Although the macroscopic parameters, like yielded electric current, for example, can be simulated [29], this approach is more often used to understand the reaction mechanism and get an idea about how the material should be modified in order for its activity to be enhanced [30, 31]. The main issue with this strategy is a lack of experimental information.

DFT calculations may allow one to reconstruct the energetically favourable reaction pathway, which usually includes hydrogen adsorption, diffusion and recombination. The results of the simulations, obviously, depend on the applied approximations, such as the size and quality of the electron functions (plain waves or orbitals) quality of the exchange functionals and integration or not of the van-der-Walls terms. In order to be certain that the utilised set of approximations is valid for a particular system, one inevitably needs supportive experimental information to compare the simulations with. Unfortunately, there is no single experiment that can yield all the required information at once (the properties of hydrogen adsorption, diffusion and recombination), therefore a broad study by means of several direct and indirect techniques with their intra-comparison in necessary to build a foundation for numerical studies. However, due to said complexity, little research has been made in that regard so far. The main tool, which, theoretically, can give almost direct information about hydrogen adsorption sites and diffusion patterns within a material matrix, is the inelastic neutron scattering (INS) [4] [32–34]. We will come back to this technique later in the "Methods" section (2.2.1), but for now it is important to note that neutron scattering is practised only within large scale facilities, which are not many in the world, and the demand is high, therefore each neutron experiment needs to be thoroughly justified in order to take place. In this work we have made an attempt to fill in this experimental knowledge void and understand the diffusion mechanism

[3] A more detailed description will be given later, in the "Methods - Cyclic and linear voltammetry" section (2.5).

[4] Actually, there are several methods that fall under this notation, and at least two are needed in order to achieve the described results.

of hydrogen within MoS_2 by means of several complementary techniques.

Before diving deep into the experimental part, which will be presented later, we would like to give a brief review of what is already known about the hydrogen evolution reaction on MoS_2 from the numerical simulations and electrochemical experiments point of view. First, we can have a look at what is considered an active site for the HER. Earlier studies reported amorphous MoS_2 particles to be the most catalytically active [35], however, later, crystalline nanosheets yielded comparable results [36]. At the same time it was revealed that the metallic 1T phase of MoS_2 is more active as compared to naturally occurring 2H semiconducting phase [36] due to higher electrical conductivity. Later it was shown that adsorbed hydrogen prefers to bind to surface S atoms, rather than to molybdenum [30]. Now, after many more DFT investigations, it is generally accepted that sulphur atoms are the main active sites, along with their vacancies [37], and hydrogen evolution occurs in their vicinity. However, studies aimed at examining the possible reaction near molybdenum atoms are also present [38]. Hence, considering that the HER takes place near S atoms we can start discussing the possible reaction pathways. Hydrogen evolution is assumed to occur in two steps, with the first one being the Volmer step and the second one being either Heyrovsky or Tafel step. The reaction starts with the adsorption of one H atom on the surface of MoS_2:

$$H^+ + e^- \rightarrow H_{ads}, \tag{1.5}$$

where H^+ may be supplied, for example, by the electrolyte during electrolysis. This is called the Volmer step. Next, according to the Heyrovsky mechanism, the adsorbed H atom at the surface of MoS_2 may recombine with H^+ from the electrolyte to form H_2 in gaseous state:

$$H_{ads} + H^+ + e^- \rightarrow H_{2(g)}. \tag{1.6}$$

Another possibility is the Tafel step, which includes the adsorption of the second H atom. Two adsorbed atoms then diffuse around the crystal to finally meat each other and recombine into an H_2 molecule:

$$2H_{ads} \rightarrow H_{2(g)}. \tag{1.7}$$

Simulations usually yield a low energy barrier for the Volmer step on MoS_2, and state that the overall reaction rate is determined by the second

step, where the Volmer-Heyrovsky route is estimated to be an energetically favoured process over the Volmer-Tafel route [30, 38–41]. However, the difference in the reported energy barriers between the Heyrovsky and Tafel step is not great. Moreover, some researchers acquired the opposite results for a particular configuration of MoS_2, with the Volmer step being the rate determining and the Volmer-Tafel route dominating over the Volmer-Heyrovsky route [31]. Therefore, in a real electrolysis experiment, it may as well be that both processes contribute significantly to the overall catalytic activity of the material.

The rates of both Heyrovsky and Tafel step are influenced by the diffusion pattern of hydrogen. For the Tafel step the reason is obvious, two H atoms are not necessarily adsorbed on the neighbouring S atoms, hence their interaction requires diffusion towards each other. The case of the Heyrovsky mechanism is not so straightforward. The reaction can, indeed, occur at the same site, where an H atom was adsorbed, since in this case only a solvated proton is required. However, if the number of active sites is small (consider S edge atoms), then the adsorbed atom needs to migrate to a non-active site in order to free up the space for another atom to be adsorbed, the so called spillover effect. This is especially true when the Volmer step has a relatively small energy barrier as compared to the Heyrovsky step. In fact, this effect applies to the Tafel sub-reaction as well. Although important, the diffusion aspect is not often addressed in the numerical studies aimed at unveiling the HER mechanism, due to computational difficulties. The initial state of the simulated system for the Tafel step is set such that two H atoms are adsorbed on top of two closest sulphur atoms [30, 31], hence no diffusion is required for their interaction. For the Heyrovsky step the adsorbed H atom is surrounded with solution molecules and recombines in place [30].

Nevertheless, the information on hydrogen diffusion in MoS_2 can still be found [42, 43], but these are completely different studies and the number of such papers is very limited. The work by An et. al. [42] reveals that hydrogen transport in the intra-layer space of MoS_2 occurs via jumps from S atom of one layer, to S atom of another layer in a zigzag fashion. These jumps are assisted by the shear modes of the material. Interestingly, this diffusion path does not depend on whether H or H^+ is introduced into MoS_2, because they both seem bind to S atoms with almost the same binding energies [42] due to neutralisation of H^+ upon interacting with the matrix. However, this does not mean that H and H^+ are identical in all aspects of interaction with MoS_2. When bound to sulphur, neutral H atom keeps its electron and does

not disturb the electronegativity or the host atom. A proton, on the other hand, attracts the equivalent of almost one electron and alters local charge in the system. Upon leaving the adsorption site, H atom stays neutral, but previously neutralised H^+ cannot take the attracted electron with it, instead it flies away as a proton and lets the vacated adsorption site return to its initial charge distribution. After a jump the proton binds to a new S atom, perturbing the charge distribution again at a new adsorption site. This may be a reason why the interaction with S vacancies is different for H and H^+. The local environment of a sulphur vacancy acts as a trap for hydrogen atoms, providing higher absolute value of the binding energy, thus, effectively slowing H diffusion. Protons, although attracted to a vacancy, do not fall into the trap and their overall diffusion coefficient remains unchanged. The work of Yong Pan [43] includes the examination of possible pathways for H diffusion through the layers of MoS_2, i.e. perpendicular to the basal planes. Although it was experimentally proven that protons cannot traverse a single MoS_2 layer [44], it appears from first-principles calculations that neutral atoms actually can. The energy barrier for diffusion through the layers of MoS_2 [43] seems to be similar to the one for hydrogen jump from one S atom to another [42].

Clearly, it is unsatisfactory that such a vast amount of information obtained via numerical simulations has to rely on extremely scarce experimental data. In these circumstances it becomes perplexing to decide which method or model would yield the most realistic results, leading to sometimes hard to believe (compare [42] and [43]) or even contradictory results (compare [39] and [31]). Therefore in the current work we decided to extensively investigate the interaction of hydrogen with MoS_2 by means of various experimental techniques, with the emphasis on the diffusion of hydrogen in MoS_2 single crystals. The main text of the thesis commences with an explanation of the methods used throughout the project, and then continues with the experiments carried out and their results. Experiments will be grouped by samples and ordered historically. In the end of the thesis a conclusion chapter is provided, followed by the possible prospects.

Chapter 2

Methods

2.1 Sample preparation, hydrogen loading

2.1.1 Electrolysis

Electrolysis is a technique which uses electric current to induce a particular desired reaction on the electrodes by bringing the ions from the electrolyte to the respective electrodes. A basic electrochemical cell consists of two electrodes, anode (+) and cathode (-), liquid electrolyte and a direct current (DC) power source, which is often controlled via a suitable software on a PC (Fig. 2.1). Usually, the interest lies in only one side reaction, either on cathode, or anode. Therefore the solution is chosen in such a way that the corresponding ion (cation or anion, respectively) is relatively light in terms of molecular mass. This is done because the velocity with which an ion is brought to the respective electrode is inversely proportional to its mass. And hence this selec-

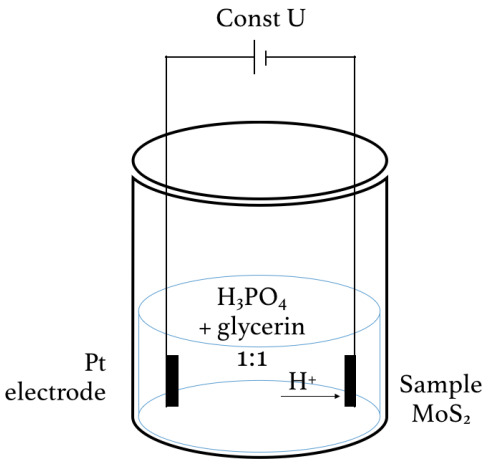

Fig. 2.1: A scheme of the electrolysis layout. In a glass beaker, two electrodes, Pt plate anode and MoS_2 on Ta plate cathode, are immersed in a solution of 1:1 H_3PO_4 and glycerol. Electrodes are connected to a DC power supply.

tion approach insures that a satisfactory reaction rate is achieved with low or moderate voltage.

In the current project the aim is to introduce hydrogen in MoS_2, therefore the layout that has been used is Pt plate as anode, MoS_2 crystals mounted on a Ta plate (using Ta wires) as cathode and phosphoric acid mixed 1:1 with glycerol as electrolyte, with the latter providing the following ions:

$$H_3PO_4 \rightleftharpoons H^+ + H_2PO_4^-.$$

The exposed hydrogen ions subsequently migrate towards MoS_2 crystals and can be adsorbed on a surface, or penetrate the material and settle in the bulk. Although, hydrogen ions in MoS_2 are expected to, in most cases, form -SH groups [42], other H containing species are also possible to be generated. Since the utilized layout for electrolysis was set in air, accumulated oxygen in solution and surface molybdenum oxides may act as a source for H_2O formation. Also, after the loading the electrolyte had to be washed off. It was done using demineralised water, which could leave a trance of H_2O on the surface. Moreover, given the known reactivity of MoS_2 towards the hydrogen evolution reaction, sorbed H atoms may recombine into H_2 molecules over time. Therefore, various hydrogen species can be expected in samples prepared via this method. Two loading techniques that are more specific in terms of hydrogen species and that were used in this work are described below.

2.1.2 Atom beam bombardment

Although electrolysis is the most interesting type of H loading due to its broad use in industry, the ambiguity in H species formation makes it puzzling to analyse hydrogen diffusion in a material, loaded electrochemically. Therefore it is important to back up our studies with more "clean" loading procedures. One of such techniques is atom beam bombardment. In this case a jet of H_2 gas is directed at a specimen, but before it reaches its aim, it needs to pass through an incandescent tungsten filament heated to T $\approx$ 1900 K (Fig. 2.2). The filament splits some of H_2 molecules into atoms, which continue their way towards the sample. Those atoms are then caught by the MoS_2 matrix. The process is carried out under ultra-high vacuum (UHV) in a chamber backfilled with hydrogen gas to 10^{-6} mbar, therefore there is much less ambiguity in the formed H species. The filament temperature was set according to literature

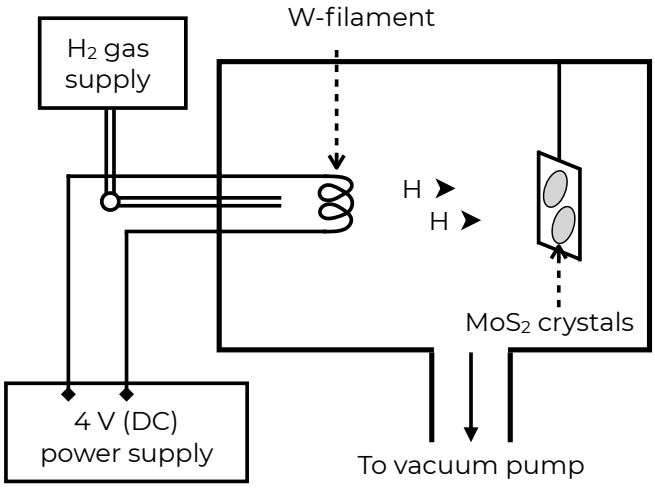

Fig. 2.2: A non-to-scale drawing of an instrument set-up for atom beam bombardment. The main experiment chamber is constantly pumped by a turbo-molecular pump. Hydrogen gas from a bottle is injected into the chamber via a glass capillary, which faces the Ta plate where the MoS_2 crystals are mounted. Inside the chamber, crossing the hydrogen path, a hot W filament is placed, which drives H_2 dissociation into H atoms. The latter subsequently bombard the sample.

[45–47]. Control experiments showed negligible H content in MoS_2 under H_2 flow with the filament switched off, which means that only H atoms enter the material during loading. Nevertheless, the recombination of H atoms into H_2 cannot be excluded. We note, that although the binding strengths of H and H^+ to S atoms are shown to be very close [42], the recombination rates in atom beam and electrolysis loading may be different due to the presence of applied potential in the latter.

The instrument for the atom beam bombardment also allows for heating of a sample. This feature was often exploited throughout the project. The number of MoS_2 single crystals available was limited, so they were frequently reused for different experiments. Thus it was crucial to clean the crystals of any remaining hydrogen. It was proven by nuclear reaction analysis that at temperatures above 750-800 K hydrogen content decays to a background level. Hence the cleaning procedure consisted of 3 cycles of heating the crystals in UHV to 750 K and staying there for 10 min, and one flash heating to 850 K. It should be noted that the atom beam loading was performed

right after the cleaning, in the same chamber. However, for the electrolysis and soaking in water the crystals had to be removed from the instrument, and therefore they were exposed to air for some time.

2.1.3 Soaking in water

Another method to load MoS_2 with a particular hydrogen species is soaking it in distilled water. The method is straightforward and does not require an explicit explanation. Under ambient conditions, MoS_2 crystals are drowned in a beaker with distilled H_2O and are let to infuse for several hours. After that they are taken out of the water and dried gently with a paper cloth to remove any excess water. We are not expecting H or H_2 to be generated this way, at least, within the time frame used in this study, which is from 4 to 24 hours. Therefore, this technique was used to isolate the effect of surface water diffusion on an inelastic neutron spectrum. We note that this method requires a proper cleaning and degasing of the sample to get rid of any surface and, especially, bulk hydrogen, which could be left from previous experiments with the same crystals.

2.2 Quasi-elastic neutron scattering

2.2.1 Theory

We would like to commence methods description with the main technique utilized during this work, which is quasi-elastic neutron scattering (QENS), a particular case of inelastic neutron scattering. Let us start with explaining what neutron scattering is, in general. The neutron is a subatomic particle, carrying a mass of 940 MeV/c^2, no (or an extremely small) electric charge, and a substantial magnetic moment of -1.9 μ_n (nuclear magnetons). In terms of experimental utilization neutrons are similar to photons. In a nutshell, neutron (X-ray) scattering consists of irradiating a specimen with an incoming neutron (X-ray) beam and detecting outcoming, scattered or not, neutrons (photons or electrons), as well as their flight direction and energy. The scattering pattern can then give a vast amount of information about the system under study. There are several techniques which can be realized with both neutrons and X-rays, such as diffraction or imaging. However, photons and neutrons are not the same, as the latter posses mass and mag-

netic moment, thus a number of extra techniques are available to neutron users (though some of the X-ray methods are not accessible with neutrons). The main advantages of neutrons over X-rays, which are widely exploited, are an extreme penetration power, the existence of magnetic moment and an independent of atomic number scattering amplitude. It is important to explain this part in more detail. The penetration length of X-rays lies in the range of μm or mm, while for neutrons it can span up to several meters. This allows for the investigations of the processes occurring in the bulk of a sample. The magnetic moment of a neutron can interact with the sample's magnetic structure, thus making it accessible to study with neutrons. Strictly speaking, the magnetic structure can be defined with X-rays as well. However, the amplitude of magnetic scattering for X-rays is 5 orders of magnitude lower than the one of atomic scattering, while for the neutrons they are similar. The X-ray scattering power of atoms is well defined and is governed by the Z^2 law, where Z is the atomic number (Fig. 2.3). Clearly, in X-ray imaging, such behaviour makes it extremely difficult to distinguish two elements, the atomic numbers of which differ by one, especially for light elements. In case of neutrons, on the other hand, the scattering amplitude behaves like a random process (Fig. 2.3), therefore, close in atom weight elements can differ in amplitude significantly. This property of neutron scattering cross section impacts in different ways all the neutron scattering techniques. Additionally, atoms with different atomic mass, but the same Z (isotopes) also exhibit distinct neutron scattering amplitude, while for X-rays these elements are identical. This fact serves as a foundation for a powerful technique called Isotopic Substitution, the description of which is beyond the scope of the current work.

Neutron properties described above make it a tool of choice for many researchers. The range of problems that can be solved with neutrons is broad, from examining the insides of a meteorite [49] to discovering the size and shape of complex organic compounds [50], from studying the dark matter [51] to defining the magnetic structure of superconductors [52]. And most of the neutron techniques are based on a simple principle: when you irradiate a sample with a beam of neutrons, they scatter, and the way they scatter depends on intrinsic properties of a sample. Therefore our next aim would be to establish a connection between the scattering pattern and the properties of a material.

For a start, we consider a common case of a monochromatic beam of neutrons with an incident energy E_0 and wavevector $\boldsymbol{k_0}$ irradiating a specimen.

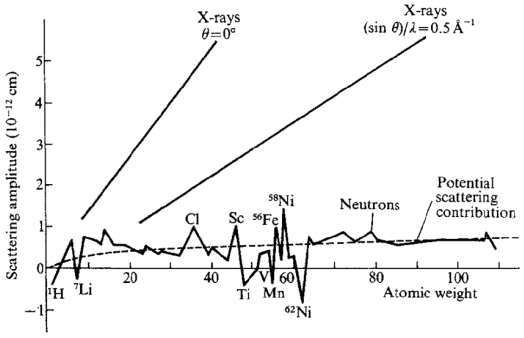

Fig. 2.3: Coherent scattering amplitudes for X-rays and neutrons versus atomic number. For X-rays the dependence on the scattering angle is also depicted. Figure after Bacon [48].

In order to describe the scattering phenomenon a general quantity called a double differential cross section $\frac{\partial^2\sigma}{\partial\mathbf{\Omega}\partial\omega}$ is used. It represents the probability that a neutron is scattered into a solid angle $d\mathbf{\Omega}$ around the direction $\mathbf{\Omega}$, with an energy exchange lying in the range $\{\hbar\omega, \hbar(\omega + d\omega)\}$, where in the absence of energy exchange the scattering is called elastic, and otherwise, inelastic. The basic expression for the double differential cross section can be written as follows [32]:

$$\frac{\partial^2\sigma}{\partial\mathbf{\Omega}\partial\omega} = \frac{k}{k_0}\frac{1}{2\pi N}\times$$
$$\times \sum_i \sum_j \int_{-\infty}^{\infty} \langle b_i b_j \exp(i\boldsymbol{Q}\boldsymbol{R}_i(t)) \exp(-i\boldsymbol{Q}\boldsymbol{R}_j(0))\rangle \exp(-i\omega t)dt. \quad (2.1)$$

Here the summation goes over all the nuclei in the sample and thermal averaging over their position and spin, k is a neutron wavevector after interaction, N is a number of particles in a specimen, b is a neutron scattering length, a tabulated quantity representing the scattering power of a nucleus which depends also on spin, i is an imaginary unit, $\boldsymbol{Q} = \boldsymbol{k_0} - \boldsymbol{k}$ is a momentum transfer vector, $\boldsymbol{R}$ is a vector showing the position of a nucleus and $\hbar\omega$ is an energy exchange. A more strict quantum-mechanical representation of Eq. 2.1, which can be found in [32], would imply the use of $\hat{R}$ operator, however, for simplicity, here we will use a classical representation in terms of vectors. It is common to divide the Eq. 2.1 into two quantities: the coherent $\left(\frac{\partial^2\sigma}{\partial\mathbf{\Omega}\partial\omega}\right)_{coh}$ and incoherent $\left(\frac{\partial^2\sigma}{\partial\mathbf{\Omega}\partial\omega}\right)_{inc}$ double differential cross section

(DDCS), because it allows to differentiate collective effects (coherent constituent), and single particle motion (incoherent constituent). Assuming a system consisting of n different types of atoms and introducing their indices as $\alpha, \beta = \{1, n\}$ we can write the following equations [32, 53]:

$$\left(\frac{\partial^2\sigma}{\partial\boldsymbol{\Omega}\partial\omega}\right)_{coh} = \frac{1}{N}\frac{k}{k_0}\sum_{\alpha=1}^{n}\sum_{\beta=1}^{n} b_\alpha^{coh} b_\beta^{coh}\sqrt{N_\alpha N_\beta} S^{\alpha\beta}(\boldsymbol{Q},\omega), \tag{2.2}$$

where:

$$S_{coh}^{\alpha\beta}(\boldsymbol{Q},\omega) = \frac{1}{2\pi}\frac{1}{\sqrt{N_\alpha N_\beta}}\times \\ \times\int_{-\infty}^{\infty}\sum_{i_\alpha=1}^{N_\alpha}\sum_{j_\beta=1}^{N_\beta}\langle\exp(i\boldsymbol{Q}\boldsymbol{R}_{i_\alpha}(t))\exp(-i\boldsymbol{Q}\boldsymbol{R}_{j_\beta}(0))\rangle\exp(-i\omega t)dt, \tag{2.3}$$

and:

$$\left(\frac{\partial^2\sigma}{\partial\boldsymbol{\Omega}\partial\omega}\right)_{inc} = \frac{1}{N}\frac{k}{k_0}\sum_{\alpha=1}^{n}(b_\alpha^{inc})^2 S_{inc}^{\alpha}(\boldsymbol{Q},\omega), \tag{2.4}$$

where:

$$S_{inc}^{\alpha}(\boldsymbol{Q},\omega) = \frac{1}{2\pi}\frac{1}{N_\alpha}\times \\ \times\int_{-\infty}^{\infty}\sum_{i_\alpha=1}^{N_\alpha}\langle\exp(i\boldsymbol{Q}\boldsymbol{R}_{i_\alpha}(t))\exp(-i\boldsymbol{Q}\boldsymbol{R}_{i_\alpha}(0))\rangle\exp(-i\omega t)dt. \tag{2.5}$$

Here $S(\boldsymbol{Q},\omega)$ is called the dynamic scattering function, the subscripts α and β separate the quantities related to the respective species, and the coherent and incoherent scattering lengths are defined as follows:

$$b_i^{coh} = \langle b_i\rangle, \tag{2.6a}$$

$$b_i^{inc} = \sqrt{\langle b_i^2\rangle - \langle b_i\rangle^2}, \tag{2.6b}$$

where the averaging goes over all the isotopes and spin states of an element.

Now it is a right time to recall the system of concern in the current work, since it will significantly simplify the following derivations. The studied phenomenon is hydrogen diffusion in MoS_2, and therefore we are mostly

interested in the incoherent scattering, since it represents averaged single particle motion. A fascinating fact about hydrogen is that it possesses a huge incoherent scattering length, as compared to the ones of the other elements [54], which allows us to neglect any contribution to the Eq. 2.4 apart from the one, related to hydrogen. Therefore Eq. 2.4 and 2.5 reduce to:

$$\left(\frac{\partial^2\sigma}{\partial\boldsymbol{\Omega}\partial\omega}\right)_{inc} = \frac{1}{N}\frac{k}{k_0}b_{inc}^2 S_{inc}(\boldsymbol{Q},\omega), \tag{2.7}$$

$$\boxed{S_{inc}(\boldsymbol{Q},\omega) = \frac{1}{2\pi}\int_{-\infty}^{\infty} I_{inc}(\boldsymbol{Q},t)\exp(-i\omega t)dt,} \tag{2.8}$$

$$I_{inc}(\boldsymbol{Q},t) = \frac{1}{N}\sum_i \langle \exp(i\boldsymbol{Q}\boldsymbol{R}_i(t))\exp(-i\boldsymbol{Q}\boldsymbol{R}_i(0))\rangle, \tag{2.9}$$

where we introduced the so called intermediate function $I(\boldsymbol{Q},t)$, which is a reverse time-Fourier transform of the scattering function. By going further and performing a space-Fourier transform of the intermediate function one may come up with an auto-correlation function in the following form:

$$\begin{aligned} G_{inc}(\boldsymbol{r},t) &= \frac{1}{(2\pi)^3}\int I_{inc}(\boldsymbol{Q},t)\exp(-i\boldsymbol{Q}\boldsymbol{r})d\boldsymbol{Q} \\ &= \frac{1}{N}\sum_i \int \langle \delta(\boldsymbol{r}-\boldsymbol{r}'+\boldsymbol{R}_i(0))\delta(\boldsymbol{r}'-\boldsymbol{R}_i(t))\rangle d\boldsymbol{r}', \end{aligned} \tag{2.10}$$

where $\delta(x)$ is the Dirac delta function. $G_{inc}(\boldsymbol{r},t)$ can be interpreted as a probability of finding a particle in an infinitesimal vicinity of the position $\boldsymbol{r}$ at time t, given *the same* particle was at the origin at time $t = 0$. The auto-correlation function characterises the system, that is being studied, and can be derived from the very fundamental description of the system in terms of quantum mechanics (solution of the Schrödinger equation), as well as from various microscopic diffusion laws. The latter option is of the greater importance for us. After all, what is usually of interest when doing the quasi-elastic neutron scattering, is the type and properties of molecular diffusion. Whether it is translational or rotational diffusion, continuous or jump-like, 2-fold or 3-fold. For each scenario a diffusion equation either exists [32], or can be derived. From this equation it is possible then to calculate the auto-correlation function $G(\boldsymbol{r},t)$, and by doing the space-time-Fourier transform

one can come up with the scattering function $S(\boldsymbol{Q}, \omega)$, which should be compared to the experiment. Thus we have established a connection between the fundamental laws governing the system and the corresponding inelastic neutron scattering pattern.

The calculation of Eq. 2.10 requires a model which describes the position of a scatterer at any given point in time. A general model that would account for any possible motion is almost impossible to construct, therefore several assumptions must be made that would simplify the calculations. The main motion modes of an atom are vibrations within a molecule, reorientations of a molecule as a whole around its internal axes and translational motion of a molecule or an atom. The vibrations are usually rather fast, with an energy of the order of 100 meV and more, and are observed as a peak in the high transferred energy, $\hbar\omega$, region, while the translations and reorientations are much slower, in the range of a few meV or even μeV, and with a centre at $\hbar\omega = 0$ meV [32]. Therefore, in order to distinguish the energy regions where different motion modes are observed, the notion of the quasi-elastic (QE) region was implemented, which covers the energy transfer values below several meV. Thus, the QENS provides direct access to the molecular translational and rotational motion modes, without the interference from vibrations and other high energy modes.

In a real experiment, which will be discussed later in the Instruments section, the separation between the transferred energy regions can be observed as it is schematically presented in Fig. 2.4. At $\hbar\omega = 0$ there is an elastic line, representing neutrons that did not change their energy after the scattering process. Ideally it should be the Dirac delta function, however, every instrument is not perfect and possesses a resolution function, which, basically, displays the fact that the point $E \equiv \hbar\omega$ contains information from the region $\{E - \Delta E/2, E + \Delta E/2\}$, rather than from one point in the energy space. Therefore in a real experiment at $\hbar\omega = 0$ there is a peak with a finite width ΔE (usually a Gaussian), and not the Dirac delta. The QENS signal is observed as a zero-centred peak superimposed on the elastic line, i.e. as a broadening of the elastic line. The true inelastic signal is usually non-zero centred, since it has a corresponding to the phenomenon's characteristic energy. In general it can occur at any $\hbar\omega$ point, including the QENS region and very close to $\hbar\omega = 0$, where it can be mixed with the QENS signal. For MoS_2, which is studied in the current work, no significant inelastic signal within the QENS region is expected [55, 56], therefore, it will not be discussed further.

Now we can finally start applying the formalism described above to the

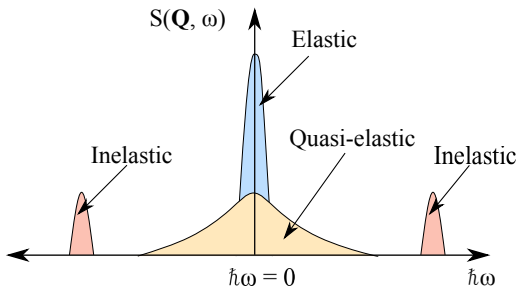

Fig. 2.4: Schematic representation of the transferred energy regions. At $\hbar\omega = 0$ there is an elastic peak with a resolution function width. At small $\hbar\omega$ quasi-elastic scattering is observed in the form of a broad peak centred at $\hbar\omega = 0$. And finally at large $\hbar\omega$ true inelastic effects occur, which are not centred at zero.

system studied in this work, hydrogen in molybdenum sulphide. As it is mentioned above, it is possible to derive the scattering function from an appropriate diffusion equation. A common strategy from textbooks would be to consider Brownian diffusion and easily obtain the $S(Q, \omega)$ function in the form of Lorentzian [32], however, in this work we would like use the Chudley-Elliot model [57] for such kind of example, which is a basic model for diffusion via jumps across a periodic array of sites. It seems more natural given that the system we study is hydrogen within MoS_2. Hence, below we will show how, starting from a rate equation in terms of particle position probability and performing Fourier transforms, to come up with the scattering function in the form of Lorentzian.

The Chudley-Elliot model considers a jump diffusion among the equilibrium sites located over a Bravais lattice. For simplification the available jump sites are restricted to the nearest neighbours only. In this case the rate equation for the probability $P(\boldsymbol{r}, t)$ of finding an atom on a site at a distance $\boldsymbol{r}$ from an arbitrarily chosen origin is:

$$\frac{\partial}{\partial t} P(\boldsymbol{r}, t) = \frac{1}{n\tau} \sum_{\boldsymbol{l}_i} [P(\boldsymbol{r} + \boldsymbol{l}_i, t) - P(\boldsymbol{r}, t)], \tag{2.11}$$

where n is a number of jump sites, τ^{-1} is a jump rate and the summation goes over all the possible jump vectors $\boldsymbol{l}_i$. An example of a jump sites system is depicted in the Fig. 2.5. In order to obtain the self-correlation function

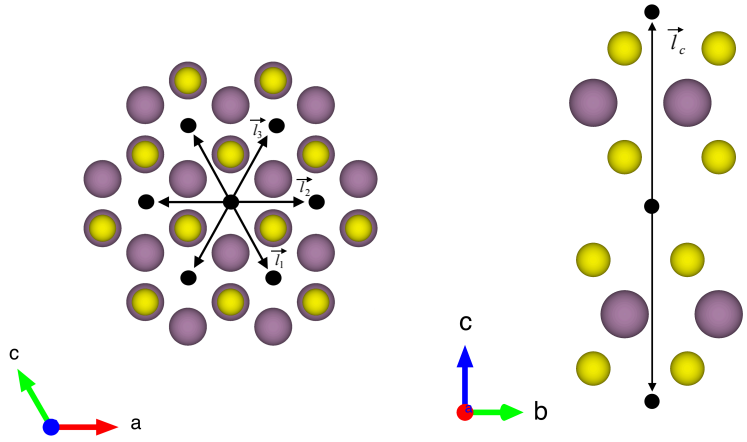

Fig. 2.5: The structure of MoS_2 and a hexagonal jump array applied to it. Molybdenum and sulphur are displayed as purple and yellow spheres, respectively. Jump sites are shown as black balls and jump vectors as black arrows.

it is required to average the Eq. 2.11 over all the possible starting positions. Luckily, in a Bravais lattice all the sites as well as their surroundings are identical, therefore $G_{inc}(\boldsymbol{r},t) \equiv P(\boldsymbol{r},t)$. By replacing $P(\boldsymbol{r},t)$ with $G_{inc}(\boldsymbol{r},t)$ in Eq. 2.11 and performing a space-Fourier transform one may come up with a rate equation for the intermediate function $I_{inc}(\boldsymbol{Q},t)$:

$$\frac{\partial}{\partial t} I_{inc}(\boldsymbol{Q},t) = \frac{1}{n\tau} \sum_{\boldsymbol{l}_i} I_{inc}(\boldsymbol{Q},t)[\exp(-i\boldsymbol{Q}\boldsymbol{l}_i) - 1], \tag{2.12}$$

with the standard boundary condition $I_{inc}(\boldsymbol{Q},0) = 1$. Denoting by

$$\Gamma_{CE}(\boldsymbol{Q}) = \frac{\hbar}{n\tau} \sum_{\boldsymbol{l}_i} [1 - \exp(-i\boldsymbol{Q}\boldsymbol{l}_i)] \tag{2.13}$$

the following solution is not difficult to obtain:

$$I_{inc}(\boldsymbol{Q},t) = I_{inc}(\boldsymbol{Q},0) \exp[-\Gamma_{CE}(\boldsymbol{Q})t/\hbar]. \tag{2.14}$$

Finally the time-Fourier transform yields the scattering function in the form of Lorentzian with the half-width-at-half-maximum (HWHM) $\Gamma_{CE}(\boldsymbol{Q})$:

$$\boxed{S_{inc}(\boldsymbol{Q},\omega) = L(\Gamma(\boldsymbol{Q}),\omega) = \frac{1}{\pi} \frac{\Gamma_{CE}(\boldsymbol{Q})}{(\Gamma_{CE}(\boldsymbol{Q}))^2 + (\hbar\omega)^2}.} \tag{2.15}$$

It is very common to obtain the scattering law in the form of Lorentzian. Indeed, a number of other models, such as continuous diffusion [32], Hall-Ross [58], Sears [59] model etc. also end up with a similar result: one or a series of Lorentzians representing the scattering function. Therefore, most of the information about the diffusion is contained in the width parameter $\Gamma(\boldsymbol{Q})$. It is also important to note that if a scatterer exhibits several diffusion modes, they should come in convolution in the scattering law, while in the case of several different types of scatterers, their contributions come in a simple sum, provided there is no correlation [32].

For the Chudley-Elliot model it is possible to go further and take into consideration also the structure of MoS_2, which is layered and possesses hexagonal symmetry. This would lead to a simple expression for the width parameter $\Gamma_{CE}(\boldsymbol{Q})$, which will be used in subsequent analysis of the experimental data.

For any Bravais lattice the distances $\boldsymbol{l}_i$ and $-\boldsymbol{l}_i$ occur equally and therefore the Eq. 2.13 can be transformed to:

$$\Gamma_{CE}(\boldsymbol{Q}) = \frac{\hbar}{n\tau}[n - 2\sum_{\boldsymbol{l}_i>0}\cos(\boldsymbol{Q}\boldsymbol{l}_i)], \tag{2.16}$$

where the summation runs over the neighbouring sites in only one half-space. Here we will consider a jump site array composed of the centres of hexagonal holes in MoS_2 (Fig. 2.5), which is one of the probable arrangements for H or H_2 sorption (see Fig. 4.19). It can be imagined as two right hexagonal pyramids having their bases glued together, with the origin placed in the centre, vertices set as jump sites and jump distances set equal to l and l_c parallel and perpendicular to the basal planes, respectively. The summation in Eq. 2.16 can then be written explicitly:

$$\Gamma^{hex}_{CE}(\boldsymbol{Q}) = \frac{\hbar}{4\tau}\left[4 - \cos(\boldsymbol{Q}\boldsymbol{l}_1) - \cos(\boldsymbol{Q}\boldsymbol{l}_2) - \cos(\boldsymbol{Q}\boldsymbol{l}_3) - \cos(Ql_c\cos(\theta))\right], \tag{2.17}$$

where we used the cylindrical coordinate system with z aligned perpendicular to the MoS_2 basal planes and $\|\boldsymbol{l}_1\| = \|\boldsymbol{l}_2\| = \|\boldsymbol{l}_3\| = l$. It is possible (the exact implementation will be discussed in section 3.2.4) to set the geometry of an experiment such that $\theta \approx 0$ (out-of-plane geometry), or $\theta \approx \pi/2$ (in-plane geometry), which would allow for a separate study of the diffusion phenomena

perpendicular and parallel to the basal planes, respectively. In the former case Eq. 2.17 becomes:

$$\Gamma_{CE}^{hex}(\boldsymbol{Q} \parallel z) = \frac{\hbar}{4\tau}[1 - \cos(Ql_c)], \tag{2.18}$$

and in the latter:

$$\Gamma_{CE}^{hex}(\boldsymbol{Q} \perp z) = \frac{\hbar}{4\tau}\left[4 - \cos(Ql\cos(\phi - \pi/6)) - \cos(Ql\cos(\phi - \pi/2)) \right. \\ \left. - \cos(Ql\cos(\phi - 5\pi/6)) - 1\right]. \tag{2.19}$$

For an oriented polycrystalline sample, i.e. a set of single crystals whose basal planes are aligned, but may be rotated with respect to each other, Eq. 2.19 requires further averaging over all the possible directions of Q, i.e. over ϕ.

$$\langle\Gamma_{CE}^{hex}(\boldsymbol{Q} \perp z)\rangle_\phi = \frac{3\hbar}{4\tau}\left[1 - \frac{1}{2\pi}\int_0^{2\pi}\cos(Ql\cos\phi)d\phi\right] = \\ = \frac{3\hbar}{4\tau}\left[1 - \frac{1}{\pi}\int_0^{\pi}\cos(Ql\sin\phi)d\phi\right], \tag{2.20}$$

where the integral is the zero order Bessel function of the first kind $J_0(Ql)$, which leads to:

$$\boxed{\langle\Gamma_{CE}^{hex}(\boldsymbol{Q} \perp z)\rangle_\phi = \frac{3\hbar}{4\tau}[1 - J_0(Ql)].} \tag{2.21}$$

Therefore, if the diffusion of hydrogen in MoS_2 has a jump-like behaviour with the equilibrium sites distributed over a hexagonal pyramid array, as it was described above, then in a QENS experiment the observed Lorentzian width should follow Eq. 2.18 for the out-of-plane geometry and Eq. 2.21 for the in-plane geometry.

When we derived the structure factor in the form of a Lorentzian (Eq. 2.15) we assumed an infinite specimen with every equilibrium site having its corresponding neighbours and jump probabilities being the same for every pair of sites. However, sometimes the structure of a host material may lay constrains on the regions of space, accessible to the scatterer. For instance, in a porous material diffusion of a molecule within a pore is usually much more pronounced, than in between pores. In this case the motion is said to be constrained and the corresponding auto-correlation function gains a non-zero infinite-time limit $G_{inc}(\boldsymbol{r}, \infty) \neq 0$. In other words, if a scatterer cannot

leave some specific region of space of size V and is trapped there at all times, then the probability to find this scatterer inside any small volume within this region is never zero and is characterised by the value $1/V$ at infinite time. This non-zero limit of the auto-correlation function, after time-space Fourier transform, results in an extra term $A^{el}(\boldsymbol{Q})\delta(\omega)$ to appear in the scattering law , which represents the elastic scattering due to spatial confinement [60]:

$$S_{inc}(\boldsymbol{Q},\omega) = A^{el}(\boldsymbol{Q})\delta(\omega) + A^{qe}S^{qe}_{inc}(\boldsymbol{Q},\omega), \tag{2.22}$$

where $S^{qe}_{inc}(\boldsymbol{Q},\omega)$ is a normalized scattering function, usually a Lorentzian. The ratio of elastic scattering to the total scattering, $A(\boldsymbol{Q})$, is called the Elastic Incoherent Structure Factor (EISF) [60]:

$$A(\boldsymbol{Q}) = \frac{A^{el}(\boldsymbol{Q})}{A^{el}(\boldsymbol{Q}) + A^{qe}(\boldsymbol{Q})}. \tag{2.23}$$

The EISF essentially gives information about the geometry of a volume, where the scatterer is free to move or rotate. Some examples are diffusion within an impermeable sphere, $A(Q) = (3j_1(QR)/QR)^2$, with a radius R [61], linear diffusion between two planes, $A(Q_x) = j_0^2(Q_x l/2)$, with an interplanar distance l [58], 120° reorientations around one axis, $A(Q) = \frac{1}{3}[1 + 2j_0(Qd)]$, with a jump distance d [60], here $j_n(x)$ represents a spherical Bessel function of the order n. Therefore in the case of a Lorentzian scattering law, the width provides us with the insight into the type of diffusion, while the intensity describes the effective volume, where this diffusion phenomena occur.

Combining the information above, we can write a general expression for the scattering function, which is widely used in the analysis of QENS data [69, 70]. It consists of a sum of several Lorentzians, which represent different diffusion modes that may be exhibited by various moving species, $L_i(\Gamma(\boldsymbol{Q}),\omega)$, convoluted with the instrument resolution function, plus the resolution function itself, $S_{res}(\boldsymbol{Q},\omega)$:

$$\boxed{S_{inc}(\boldsymbol{Q},\omega) = A_{el}(Q)S_{res}(\boldsymbol{Q},\omega) + A_{qe}\sum_{i=1}^{N} A_i L_i(\Gamma(\boldsymbol{Q}),\omega) * S_{res}(\boldsymbol{Q},\omega),} \tag{2.24}$$

where A_{el} and A_{qe} are intensities of elastic and quasi-elastic scattering respectively, A_i are partial intensities of the corresponding diffusion modes and $*$ represents convolution action. Taking a quick look in a crystal ball to see

sections 3.3.2 and 4.3.2, we can say that for the analysis of the QENS data for the atom beam loaded H/MoS_2 and water loaded H_2O/MoS_2 we will be using Eq. 2.24 with only one Lorentz, while for the electrolytically loaded H^+/MoS_2, a fit with Eq. 2.24 will reveal two contributions, which, after synoptical consideration of all the data, will be assigned to H_2 molecules. Unfortunately, in case of several motion modes which may have different confining volumes, the calculation of the EISF becomes puzzling, since their elastic contributions all end up within one line. Therefore, in order to obtain more sensible information from the observed intensities, below we will develop a specific expression for the $S_{inc}(\boldsymbol{Q},\omega)$ function for H_2 molecules. We note, that the new model will only differ from Eq. 2.24 in terms of the interpretation of the intensity parameters, while the widths of the Lorentzians remain identical irrespectively of which model is used.

We start by "constructing" the basic expression for the scattering law. For H_2/MoS_2 we have the quasi-elastic scattering from mobile H_2, elastic scattering from MoS_2, which is probably small, but should not be neglected right from the start, and elastic scattering from slow H_2, slow to the point where it no longer yields any distinguishable QENS broadening. Such hydrogen we will call *immobile* hydrogen onwards, in contrast to the mobile H_2. At low temperatures (below 100 or 200 K for the experiments presented in this work) all hydrogens should be immobile and, thus, only the elastic line must be observed. We should also take into account intensity loss due to Debye-Waller factor, possible hydrogen desorption, and convolve everything with the resolution function, which gives us:

$$S(\boldsymbol{Q},\omega) = Ne^{-Q^2\langle u^2\rangle/3} \cdot [A_{el}(\boldsymbol{Q})\delta(\omega) + A_{qe}(\boldsymbol{Q})S_{qe}(\boldsymbol{Q},\omega)] * R(\boldsymbol{Q},\omega), \quad (2.25)$$

where N is a scale parameter, which is connected to the number of scatterers, $\langle u^2\rangle$ is the average squared displacement of an atom due to vibrations, $\boldsymbol{Q}$ is a momentum transfer vector, $A_{el}(\boldsymbol{Q})\delta(\omega)$ consists of elastic scattering from MoS_2 and immobile hydrogen, $A_{qe}(\boldsymbol{Q})S_{qe}(\boldsymbol{Q},\omega)$ is the quasi-elastic scattering from H_2, where $S_{qe}(\boldsymbol{Q},\omega)$ is a normalized to unity scattering function which, for now, also includes the possible elastic scattering due to spatial constrain effect, $R(\boldsymbol{Q},\omega)$ is a resolution function and $*$ is a convolution action. Considering that within the analysed temperature range (up to 500 K in the current work) immobile hydrogen can become fast enough under heating to contribute to the quasi-elastic scattering, while no significant signal is lost due to hydrogen getting too fast and subsequently leaving the spectroscopic window of an experiment, while still remaining inside MoS_2, we can

assume that $A_{qe}(\boldsymbol{Q},\omega) = 1 - A_{el}(\boldsymbol{Q},\omega)$. Additionally, we would combine all the terms that affects both elastic and inelastic scattering simultaneously into a new entity $A_{total}(Q)$, which leads us to:

$$S(\boldsymbol{Q},\omega) = A_{total}(Q)\cdot[A_{el}(\boldsymbol{Q})\delta(\omega) + (1 - A_{el}(\boldsymbol{Q}))S_{qe}(\boldsymbol{Q},\omega)] * R(\boldsymbol{Q},\omega). \quad (2.26)$$

As we have shown before, the term, which contains the most important information about the diffusive dynamics in the system, is $S_{qe}(\boldsymbol{Q},\omega)$. For molecular hydrogen we may expect two types of motion, translational and rotational. Therefore we will consider a model developed by Sears based on the first Born approximation for the case of a moving polyatomic molecule exhibiting both translational and rotational motion with negligible correlations between them [59, 62]. The model has been applied successfully to a wide range of molecules in confinement, including hydrogen, water, benzene and neopentane [63–66]. For undercooled water the approximation of negligible correlations was tested by molecular dynamics simulations and shown to be applicable at temperatures where molecules are free to move and rotate [67]. For hydrogen molecules in MoS_2, due to the low hydrogen density, the translational-rotational decoupling can be assumed to be valid for diffusion within the layers of MoS_2. For the diffusion perpendicular to the layers, however, this approximation might be satisfied to a lesser extent. Looking ahead we can say that we are mainly interested in the hydrogen motion within the layers, therefore, we consider that the approximation of negligible correlations is reasonable. In this case $S_{qe}(\boldsymbol{Q},\omega)$ can be represented by a convolution of translational, $S_T(\boldsymbol{Q},\omega)$, and rotational, $S_R(\boldsymbol{Q},\omega)$, components, respectively. For isotropic rotation on a sphere, the $S_R(\boldsymbol{Q},\omega)$ can be described by [59]:

$$S_R(Q,\omega) = j_0^2(QR)\delta(\omega) + \sum_{l=1}^{\infty}(2l+1)j_l^2(QR)L(\Gamma_R^l,\omega), \quad (2.27)$$

where $j_l(x)$ is a spherical Bessel function of the first kind of order l, R is the radius of gyration of a molecule, $L(\Gamma,\omega) = \frac{1}{\pi}\frac{\Gamma}{\omega^2+\Gamma^2}$ is a normalised Lorentzian function and $\Gamma_R^l = \frac{l(l+1)\hbar}{6\tau_{rot}}$ is the half-width at half-maximum of the corresponding rotational contribution with τ_{rot} being the characteristic time of rotation, the subscript R indicates that the terms refer to rotational diffusion. We note that for describing the motion of hydrogen atoms, the rotational terms disappear ($S_R(Q,\omega) \equiv \delta(\omega)$).

Diffusion within a crystal may be expected to exhibit some sort of spatial restrictions, hence for the translational mode it is preferably to use a more

general confined diffusion model:

$$S_T(\boldsymbol{Q},\omega) = A_0(\boldsymbol{Q})\delta(\omega) + (1 - A_0(\boldsymbol{Q}))L(\Gamma_T(\boldsymbol{Q}),\omega), \tag{2.28}$$

where $A_0(\boldsymbol{Q})$ is the EISF and $\Gamma_T(\boldsymbol{Q})$ is the width of the corresponding Lorentzian. Usually several models are tested as candidates to describe $\Gamma_T(\boldsymbol{Q})$, thus the detailed discussion regarding this parameter will be presented later. For the EISF, on the other hand, we can set a spherical confining volume with a radius r_c as a default case , for which [61]:

$$A_0(Q) = \left[\frac{3j_1(Qr_c)}{Qr_c}\right]^2. \tag{2.29}$$

By convolving Eq. 2.27 and Eq. 2.28 we get the $S_{qe}(\boldsymbol{Q},\omega)$:

$$\begin{aligned} S_{qe}(\boldsymbol{Q},\omega) &= S_T(\boldsymbol{Q},\omega) * S_R(Q,\omega) \\ &= [A_0(Q)\cdot\delta(\omega) + [1 - A_0(Q)]\cdot L(\Gamma_T(\boldsymbol{Q}),\omega)] \\ &* [j_0^2(QR)\delta(\omega) + \sum_{l=1}^{\infty}(2l+1)j_l^2(QR)L(\Gamma_R^l,\omega)]. \end{aligned} \tag{2.30}$$

The convolution in Eq. (2.30) can be performed explicitly, giving:

$$\begin{aligned} S_{qe}(\boldsymbol{Q},\omega) = A_0(Q)j_0^2(QR)\delta(\omega) \\ + A_0(Q)\sum_{l=1}^{\infty}(2l+1)j_l^2(QR)L(\Gamma_R^l,\omega) \\ + [1 - A_0(Q)]j_0^2(QR)L(\Gamma_T(\boldsymbol{Q}),\omega) \\ + [1 - A_0(Q)]\sum_{l=1}^{\infty}(2l+1)j_l^2(QR)L(\Gamma_T(\boldsymbol{Q}) + \Gamma_R^l,\omega). \end{aligned} \tag{2.31}$$

Here, we will consider a commonly occurring case, $\Gamma_R^l \ll \Gamma_T$ (the analogous reasoning can be applied if $\Gamma_R^l \gg \Gamma_T$), which allows us to neglect Γ_R^l in the last series in (2.31). Thus, the fourth item becomes $[1-A_0(Q)]\sum_{l=1}^{\infty}(2l+1)j_l^2(QR)L(\Gamma_T(\boldsymbol{Q}),\omega)$. The summation here starts from $l = 1$, however one can note that the third item $[1 - A_0(Q)]j_0^2(QR)L(\Gamma_T(\boldsymbol{Q}),\omega)$ is actually a term of this sum with $l = 0$. Hence, withdrawing Γ_T from the sum as it does

not depend on l, one can get:

$$S_{qe}(\boldsymbol{Q},\omega) = A_0(Q)j_0^2(QR)\delta(\omega) + A_0(Q)\sum_{l=1}^{\infty}(2l+1)j_l^2(QR)L(\Gamma_R^l,\omega) + [1-A_0(Q)]L(\Gamma_T(\boldsymbol{Q}),\omega)\sum_{l=0}^{\infty}(2l+1)j_l^2(QR). \quad (2.32)$$

Within the scope of our experiment ($R = 0.37$ Å for the hydrogen molecule, $Q < 2$ Å^{-1}) we generally have $QR < 0.74$ and in the first series we can neglect all terms higher than the 3rd order, as $\frac{3j_4^2(0.74)}{j_1^2(0.74)} \approx 10^{-6}$. The last sum equals unity as $\sum_{l=0}^{\infty}(2l+1)j_l^2(x) = 1$ for any value of the variable x [68]. Finally, we obtain:

$$S_{qe}(\boldsymbol{Q},\omega) = A_0(Q)j_0^2(QR)\delta(\omega) + A_0(Q)\sum_{l=1}^{3}(2l+1)j_l^2(QR)L(\Gamma_R^l,\omega) + [1-A_0(Q)]L(\Gamma_T(\boldsymbol{Q}),\omega). \quad (2.33)$$

By substituting Eq. (2.33) into Eq. (2.26), adding a background term and regrouping elements we end up with the ultimate fitting expression for our quasi-elastic spectra:

$$S(\boldsymbol{Q},\omega) = S_0(Q)\cdot\{ [\, S_{el}(Q) + (1-S_{el}(Q))A_0(Q)j_0^2(QR)\,]\cdot R(Q,\omega) + [1-S_{el}(Q)]\cdot[A_0(Q)\sum_{l=1}^{3}(2l+1)j_l^2(QR)L(\Gamma_R^l,\omega) + (1-A_0(Q))L_T(\boldsymbol{Q},\omega)] * R(Q,\omega)\} + Bkgr. \quad (2.34)$$

This equation, describing translational-rotational motion, will be used further in the analysis of the QENS data for the electrolytically loaded MoS_2 crystals. It is clear, that Eq. 2.34 preserves the main features of Eq. 2.24, in a way that both are just a sum of several Lorentzians. However, in Eq. 2.34 the intensity parameters are regrouped in such a way to allow the separation

of two confinement effects, namely, natural confinement of rotational motion, and possible confinement of translational diffusion. It should be noted that the restricting volume does not have to be impermeable in order for the confinement effect to be observable in a QENS experiment, it is enough to have a potential, which makes one region of space more probable to be occupied by a scatterer, than another [61].

2.2.2 Instruments

There are different types of QENS spectrometers [32], the ones used in this study operate either on time-of-flight (TOF, IN6-SHARP[1] at ILL and TOFTOF[2] at MLZ) or spin-echo principle (IN11[3] at ILL). The ideas underlying these principles are not complex and will be briefly discussed here.

Time-of-Flight (TOF) spectrometers measure, as it is obvious from the name, the time it takes a neutron to fly some definite path. With this information it is easy to calculate neutron's velocity and, hence, its energy. Therefore, by setting a well defined initial energy of the neutron beam and irradiating a sample with it, one obtains the distribution of neutron energies after interacting with the sample, experimental $S(\boldsymbol{Q}, \omega)$. A TOF spectrometer consists of a system, generating pulses of almost monochromatic neutron beams (usually a chopper system or a monochromator and a chopper), which creates a bunch of neutrons with energies close to a set energy; a neutron guide to a sample, and an array of detectors spaced equally far from the sample. This way a path from the monochromator to any detector is the same and known with high precision. The pulses are needed in order to set the starting point in time. The final point is when a neutron is caught in a detector. There are many factors affecting the resolution of the experiment, but most of them are set when the instrument is assembled. However, there is one thing which can be adjusted, and it is the initial speed of neutrons. The slower the neutrons, the easier it gets to resolve them in time, and thus, better resolution. However, the interval between pulses should be increased for slower neutrons, in order to avoid pulse overlapping, which, obviously, causes a drop in an average neutron flux. Thus, in a TOF experiment the resolution

[1] https://www.ill.eu/users/instruments/instruments-list/sharp/description/instrument-layout

[2] https://mlz-garching.de/toftof

[3] https://www.ill.eu/users/instruments/instruments-list/in11/description/instrument-layout

to flux ratio can be adjusted for particular needs of an experimenter.

The neutron spin-echo (NSE) technique is based on the phenomenon of Larmor precession [32]. When a polarized neutron beam travels through a magnetic field, which is perpendicular to the polarization direction, neutron's spin starts to rotate (or precess) around the magnetic field axis, and the precession angle, ϕ, increases. If, afterwards, the neutron beam traverses a magnetic field with the opposite direction, the precession goes the other way around and ϕ decreases. By assembling the instrument in such a way that a neutron beam passes subsequently two magnetic fields with opposite directions and same spatial length, one can obtain the final precession angle equal to zero, provided neutron's energy is constant throughout the process. If the energy did change after interacting with the sample, the initial spin is not fully recovered since the time spent in two magnetic fields is not the same any more. This causes the final neutron count to drop, and the amount of signal loss is related to the energy exchange. By analysing this intensity decay, one can obtain the intermediate function $I(\boldsymbol{Q}, t)$. Previously, in TOF, in order to calculate the time of flight we had to know the velocity of neutrons. With NSE this requirement no longer stands, since we measure directly the velocity difference, which, to first order, does not depend on velocity itself. This decouples the resolution of the instrument and the initial energy spread of the neutron beam, allowing to reach much better resolution than any modern TOF instrument possesses, and enabling studies of slower diffusion at small Q. The TOF and the NSE are, hence, complementary techniques, together allowing a broad Q range from 0.05 Å^{-1} to 2.6 Å^{-1} to be covered.

2.3 Nuclear reaction analysis

An atom, irradiated by an appropriate nucleus, can undergo a nuclear reaction, which would leave the nucleus of the target atom in an excited state. The excitation is usually relieved by a spontaneous emission of gamma rays with a specific energy. By counting the emitted photons it is possible to get information about the number of atoms under study in a specimen. An important feature of nuclear reactions is that they often only happen at a precise predefined energy of an incoming beam, a resonance energy. For hydrogen, which is an atom of consideration in our study, the exploited reaction is:

$$^{15}\text{N} + {}^{1}\text{H} \rightarrow {}^{12}\text{C} + \alpha + \gamma,$$

which only occurs if nitrogen ions possess an energy very close to 6.416 MeV, no further than 1 keV from the resonance. When a N beam traverses a sample, it constantly looses energy due to interaction with matter, therefore by tuning its initial energy, it is possible to reach a resonance condition at different depths in a sample. This is the main idea underlying depth profiling.

A typical nuclear reaction analysis (NRA) spectrum is depicted in Fig. 2.6. It features a large surface peak, followed by a gradual drop in H concentration with depth. The NRA data are usually easy to interpret, however, there are some points which need to be kept in mind. The ordinate is named "Bulk H concentration" for a reason. Several approximations that are used to construct the scale, which will be discussed later, do not hold for a surface peak below ∼15 nm. Therefore, although there is usually, indeed, a much higher H content near the surface, the exact value given by the graphs shown in this work should not be taken into account. In general, a separate analysis under different assumptions would be necessary to obtain surface coverages. Also, an ion beam slightly heats up the irradiated spot on a sample (temperature depends on beam current), which may cause H desorption. During a measurement, at first, a single point in energy space (or depth, they are proportional) is scanned several times until the H concentration stabilizes and does not drop significantly. This insures that the decay in photon counts with depth is not caused by H desorption, but represents the actual hydrogen distribution in a sample.

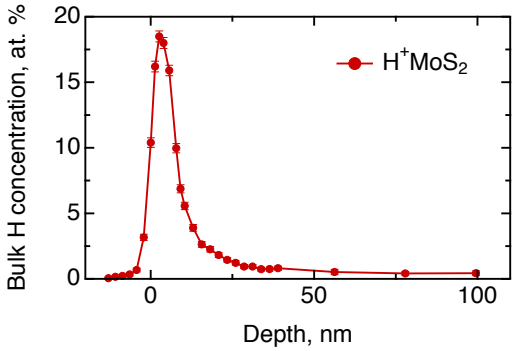

Fig. 2.6: Hydrogen content in electrolytically loaded MoS_2 single crystal, measured by nuclear reaction analysis. The concentration scale does not fully apply to the surface peak.

The raw data consist of photon counts per accumulated charge versus incoming beam energy, thus they need to be converted to hydrogen concentration versus depth. For this, one would need to know the stopping power of MoS_2 and hydrogen, which represents the energy lost by a ^{15}N beam per unit distance traversed in the material, and which can be calculated by the SRIM software [71] (Stopping and Range of Ions in Matter). For MoS_2 the stopping power is $dE/dd = 2.311 \cdot 10^{-3}$ MeV/nm, therefore in order to con-

vert an abscissa from energy to length units, it needs to be shifted by the resonance energy and divided by this coefficient. The calculation of hydrogen content is performed via the following equation:

$$R_H = K \cdot Y \cdot \epsilon_M \cdot \frac{1}{1 + KY(\epsilon_M - \epsilon_H)}, \tag{2.35}$$

where R_H is the ratio of hydrogen atoms to total number of atoms in the sample, K is an instrumental coefficient, Y represents photon yield, ϵ_M and ϵ_H are stopping cross sections of the sample's matrix and hydrogen respectively. The ϵ_H is actually not known *a priori*, since it depends on hydrogen density in a sample. Therefore Eq. 2.35 needs to be solved iteratively.

As was mentioned earlier, there are several assumptions that underlie Eq. 2.35. In a real experiment incoming beam energy is always distributed around the set value, and this distribution is further broadened by the Doppler effect and the width of the resonance. This results in an effective energy resolution of a beam, and, hence, in a smearing of the nuclear reaction in space. In Eq. 2.35 it is assumed, that all the incoming ions may participate in reactions, the so called thick target approximation. However, it is obviously not true for the topmost layer of a sample: ions with energy equal or higher than the set energy can induce the reaction at the surface or in the deeper layers, the rest of the ions, on the other hand, lack the energy to induce a reaction anywhere in the sample. Also, specimen's surface, if it was exposed to air, is often not completely clean and contains contaminations. This essentially changes the ϵ_M of the surface, resulting in an incorrect estimation of hydrogen content. The effect is usually negligible below several layers of a material, and thus it does not interfere with bulk H concentration. There are, of course, more phenomena which affect the resolution and accuracy of an NRA experiment, but they fall beyond the scope of the current work. Additional information about the technique, instrument and underlying mathematics can be found elsewhere [45, 72].

2.4 X-ray photoelectron spectroscopy

A standard tool for surface characterisation for many researchers is X-ray photoelectron spectroscopy (XPS). It allows to study electronic state of a surface, as well as performing elemental analysis. The basis for the method is the photoelectric effect, namely, electron emission from a specimen under

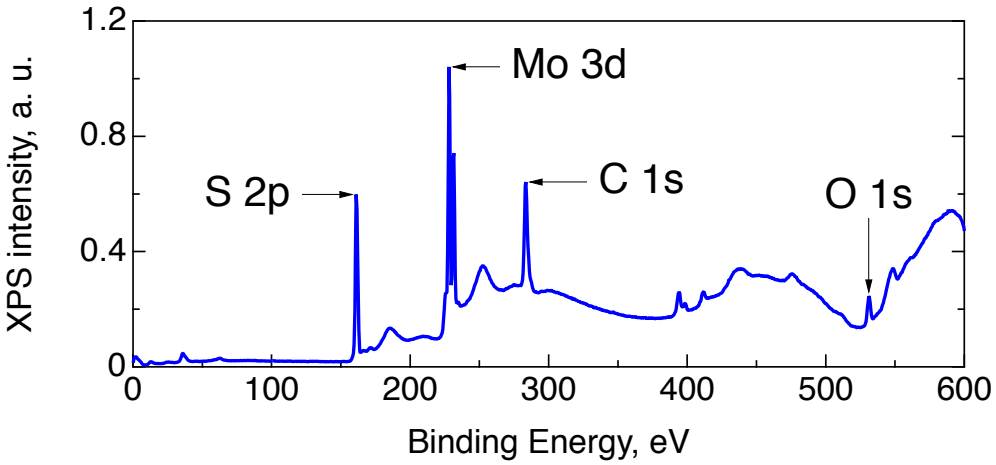

Fig. 2.7: A typical X-ray photoelectron spectrum of MoS_2, with an indication of the main elements of interest.

electromagnetic radiation. In order to remove an electron from an atom an incoming photon must transfer the electron enough energy to break its bond with the atom. This energy is called the binding energy, and it is a fingerprint of an atom. The strength of a bond depends on many different factors, including electronegativity of an atom, and thus it may vary even for the same atom in different compounds. A more detailed description will be presented later in this chapter.

The ejected electron will have a kinetic energy equal to the energy of the incoming beam, $\hbar\omega$, minus the binding energy, E_{bin}:

$$E_{kin} = \hbar\omega - E_{bin}. \tag{2.36}$$

Hence, by measuring ejected electrons' energy, one gets direct access to the binding energy of the said electrons. The method is surface sensitive in a sense that the collected information only comes from several topmost layers of material under study. This is due to an extremely small mean free path of electrons in a solid. For instance, in MoS_2 at an incident energy between 300 and 750 eV the probed depth can be approximated to be around 1 nm [73, 74], which barely covers two layers of the material.

A typical survey of MoS_2 surface is shown in Fig. 2.7. It consists of several peaks, the positions of which indicate the atoms they correspond to, and intensities are a measure of a number of these atoms in a sample, given

some remarks, mentioned below. A full survey is, to say, a first order analysis of a surface, it is mostly used to get an idea of what elements are present. A more accurate study is done via scanning each peak of interest separately. This way it is possible to tell different oxidation states of an element, and get their relative intensity. However, there is one thing which should always be kept in mind, and it is charging of a sample. During an XPS measurement electrons are removed from the sample's surface. Usually, the conductivity of the material is high enough to let the bulk refill electron vacancies on the surface. However, if it is not, then the surface is left with a residual charge, which affects the binding energies and thus, the positions of peaks in a spectrum. The positions are always referenced to a standard, known line, it could be C 1s, which is always present in a specimen kept in air, or it could be Au 4f, intentionally inserted, or other standard elements. This lowers the effect of any instrument caused shifts, or accumulated charge. Nevertheless, sometimes, if a high accuracy is desired, two or three reference points could be needed.

The interpretation of peak areas is an even more challenging task. The areas, of course, depend directly on the number of corresponding atoms in irradiated region of a sample. However, each element has a different probability to capture a photon, and thus, different electron yield. Therefore every peak needs to be corrected for the corresponding atomic subshell photoionisation cross section [75]. Further, layering in the sample is important. Electrons, generated right on the surface, reach the detector unobstructed. However, the ones generated deeper into the crystal need first to cross several layers of the material. During this journey they may scatter and loose energy, and loosing energy means they will be viewed as electrons with higher binding energy (Eq. 2.36). On a spectrum these electrons contribute to background after a peak (Fig. 2.7). Hence, two effects occur simultaneously, namely, the area of the peak decreases, because some electrons do not have their initial energy any more, and the background after the peak, at higher binding energy, increases. Let us take MoS_2 as an example of layering. Carbon and oxygen contaminations are usually situated on top of the surface, therefore the areas of the corresponding peaks are valid. The topmost material's layer is, in most cases, sulphur. Some of the peak's intensity is transferred into background, because of the contaminations. Molybdenum layer is below all of the above, and hence the area of the corresponding peak is heavily reduced. The Mo layer is then followed by another S layer, which, although greatly suppressed, contributes to the S line, and so on. The layering problem is

often rather complex, and since the information one can get from properly corrected areas is not always of a major interest, this issue is usually just kept in mind, without a final solution.

2.5 Cyclic and linear voltammetry

Electrochemistry, which includes linear (LV) and cyclic voltammetry (CV), is a method which establishes a connection between electron transfer to a compound and chemical changes in this compound. For example, suppose we have a complex A^+, it is possible to reduce it by supplying it with electrons and obtain A in the end. However, we cannot use just any electron, for the reduction to occur, the donated particles must posses energy higher than that of the lowest unoccupied molecular orbital (LUMO)[4] of A^+. Therefore, by tuning' the energy of the electrons one can study various reduction phenomena occurring at the surface of the electrode. Clearly the same is possible in the opposite direction, with electron extraction and oxidation. In an ordinary measurement both the energy of the electrons and a switch between donation/extraction can be conveniently controlled by the applied voltage in the system.

A common experimental layout consists of three electrodes, namely a working (WE), counter (CE) and reference electrode (RE), an electrolyte and a glass container where everything is put in place. The working electrode is where a sample is mounted. The reference electrode is used to monitor the applied potential, and thus its main task is to remain stable at its known potential. And the counter electrode is needed to complete the electrical circuit. Electrons, during an experiment, flow between WE and CE, thus creating a current, which is a main characteristic, measured in cyclic voltammetry.

A linear voltammetry experiment consists of one scan of the current response of the system between two predefined voltage points (Fig. 2.8, a). It is usually repeated several times to exclude possible faulty scans due to oxidised surface, for example. LV gives a clear overview on the applied potential, required to reach any specified current density with the studied electrode. An important derived quantity is the Tafel slope, which shows the sensitivity of the reaction rate on the applied potential difference. Lower Tafel slope of one catalyst over another means that the former requires a smaller voltage

[4]For a comprehensive definition of LUMO the reader is refereed to classical chemistry textbooks. In this work the detailed understanding of LUMO is not required.

increase in order to achieve the same reaction rate enhancement. This parameter usually serves as a main characteristic defining the performance of a catalyst.

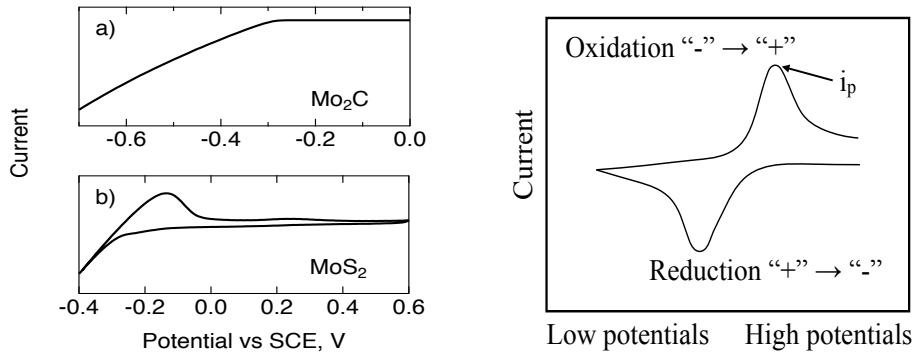

Fig. 2.8: An example of a linear voltammetry sweep (left, a), along with a "perfect" cyclic voltammetry one cycle curve (right) and a real CV one cycle curve (left, b).

A single CV measurement usually consists of dozens or hundreds of cycles of potential scans between two points. It allows to access the stability of the electrode in a long run, which is extremely important for commercial use. A common behaviour is electrode instability during several first cycles, followed by steady operation and ultimately performance decay at some point. A single scan, in ideal case, should look like Fig. 2.8 (right side). It exhibits two symmetrical parts at the top and at the bottom of the figure, which refer to oxidation and reduction, respectively. Let us say we start from a compound A in a non-oxidised state, and start ramping up the potential from low to high. At first, surface oxidation occurs, meaning A is gradually transformed into A^+, releasing electrons into the circuit and increasing current. The higher the potential, the faster this process happens, resulting in greater currents. However, over time the concentration of A at the surface decreases, since the latter becomes oxidised, and at some point the concentration gets so small that it is insufficient to maintain current growth. At this point the maximum current, i_p is reached. Afterwards the current drops until there is almost no A left on the surface, where it reaches a plateau. Here the direction of a potential sweep should be reversed to go from high to low potentials. With a negative ramp a reduction process occurs and A^+ returns back to A. If the whole oxidation-reduction cycle is reversible, the negative sweep should behave the same, as the positive one, but yielding

negative current. However, an ideal situation is almost never encountered in a real experiment, and in most cases deviations are observed, for example, specially prepared MoS_2 may yield a curve similar to Fig. 2.8 (left side). It is not symmetrical and exhibits two peaks in the oxidation part. These deviations are an important source of information, they allow, for example, to distinguish different processes occurring in the sample and tell whether they are chemically reversible or not. The description of all the possible effects spans beyond the current work. Some information will be given in the section describing the results of the CV measurements, and for a slightly more detailed overview the reader is referred to the guide by Noémie Elgrishi [76].

2.6 Numerical simulations

With the development of computational power there emerged various numerical techniques to predict (or simulate) the behaviour of atoms, molecules and more complex compounds in different environments. Each one of them posses both pros and cons. For example, density functional theory (DFT) serves as one of the most accurate methods to predict chemical and physical properties of materials, since it stems from quantum-mechanical principles [77, 78]. However, it is also extremely demanding in terms of computational resources, hence only small systems can be examined in reasonable time [79]. Classical molecular dynamics (MD) calculations, on the other hand, exploit Newton's equations of motion and, therefore, are able to work with the systems of a much larger length scale and over longer time frames [80]. This comes at a price of being unable to, for instance, simulate chemical reactions, i.e. the formation and breakage of bonds between atoms (although some state-of-the-art force-fields, like ReaxFF [81, 82], may help to overcome this issue). Of course, there exist many more computational techniques [79, 83], hence, for each particular problem a scientist ought to find a balance between the accuracy of the desired solution and the computational complexity of the exploited method.

The current study is mostly focused on experimental data, and the simulations are needed to aid the interpretation of these data. Imagine an ideal situation, where the performed experiments leave none but the only unambiguous physical interpretation. In this case the study would not require any numerical simulation, rather the experimental data itself would serve as

a framework to refine the simulation parameters for other scientists, who are specialised in this field. In a real world, however, experiments with complex systems are, most often, open to speculations, and various hypotheses can be put forward. Hence, within the scope of this project numerical simulations are needed to cut the most improbable scenarios, rather than to predict a particular outcome. Also, calculation of diffusion patterns should be performed on relatively large structures and over large time frames, therefore, time resources management should be taken into account. Hence, for our purposes, the optimal method in terms of complexity and yielded results would be classical molecular dynamics.

Classical molecular dynamics simulations consider that the interaction between each pair of atoms can be described by Newton's laws of motion [84], i.e. the particle's acceleration, $\boldsymbol{a}$, is a direct function of the applied forces, $\boldsymbol{F}$:

$$\boldsymbol{a} = \frac{\boldsymbol{F}}{m}, \tag{2.37}$$

where m stands for the mass of the particle, and the Cartesian coordinate system is used, with bold symbols representing a vector. In more general notations, for a system of N particles the Lagrangian equation is satisfied:

$$\frac{\mathrm{d}}{\mathrm{d}t}(\frac{\partial \mathcal{L}}{\partial \dot{q}_k}) - (\frac{\partial \mathcal{L}}{\partial q_k}) = 0, \tag{2.38}$$

where we introduced the Lagrangian function $\mathcal{L}(\boldsymbol{q}, \dot{\boldsymbol{q}}) = \mathcal{K} - \mathcal{V}$ in terms of kinetic, $\mathcal{K}$, and potential, $\mathcal{V}$, energy, and generalised coordinates of the system $\boldsymbol{q} = (\boldsymbol{q}_1, \boldsymbol{q}_2, ..., \boldsymbol{q}_N)$, as usual, the overhead dot notations represent time derivative. The reader may find an explicit derivation in general terms in the classical textbooks [84]. For the purposes of the brief presentation of MD simulations here we will stick to the most simple case, one dimensional version of Eq. 2.37 (interpolation to three dimensions is trivial). Hence, for a set of N atoms positioned at $\boldsymbol{x} = (x_1, x_2, ..., x_N)$ we can write a system of equations:

$$m_i \ddot{x}_i = F(x_i), \tag{2.39}$$

The idea is to simulate the evolution in time of the studied system, i.e. obtain the trajectory of each atom over the chosen time period. These trajectories can then be visualised, or used to calculate experimentally accessible parameters. Since we assume the Newtonian paradigm, the step by step solution of Eq. 2.39 must be sufficient for our cause. As a second order differential

equation, Eq. 2.39 requires two additional boundary or initial conditions. Naturally, before starting any simulation, one constructs the system which is being studied, i.e. one sets the positions of all the atoms in the system together with their properties. This gives us the first initial condition, vector $\boldsymbol{x}(t_0) = (x_1(t_0), x_2(t_0), ..., x_N(t_0))$ representing the positions of each atom in the system at $t = t_0$. Next, the global, statistical parameters are established. This can be temperature, which defines the kinetic energy distributed among all the atoms. A decent approximation would be to distribute the energy randomly using the Maxwellian distribution, which results in the second initial condition, velocities of each atom $\dot{\boldsymbol{x}}(t_0) = (\dot{x}_1(t_0), \dot{x}_2(t_0), ..., \dot{x}_N(t_0))$. Obviously, this procedure must be adapted to not induce any non-zero centre of mass velocity of the system, nor the angular momentum. Some special distributions of velocities, of course, may lead to the simulation yielding a specific, non general behaviour of the system, but it can be spotted and avoided by performing several simulations with different initial distributions. The last thing needed to solve Eq. 2.39 is the force, $F(x)$. In fact, setting the forces is one of the biggest issues encountered when starting the simulations, hence it will be addressed later in a separate paragraph. For now consider that the forces are known.

With the equation and initial conditions set, we can start calculating the trajectories of the atoms in the system via any suitable finite difference method. A simple procedure may look like this. First, use the Taylor expansion on the motion variables at time $t_0 + \delta t$, where δt is much smaller than the characteristic time of the dynamic processes in the system:

$$\boldsymbol{x}(t_0 + \delta t) = \boldsymbol{x}(t_0) + \dot{\boldsymbol{x}}(t_0)\delta t + \frac{1}{2}\ddot{\boldsymbol{x}}(t_0)\delta t^2 + O(\delta t^3),$$
$$\dot{\boldsymbol{x}}(t_0 + \delta t) = \dot{\boldsymbol{x}}(t_0) + \ddot{\boldsymbol{x}}(t_0)\delta t + O(\delta t^3), \quad (2.40)$$

here $\ddot{\boldsymbol{x}}(t_0)$ is extracted from Eq. 2.39. Next, if any set of restrictions is to be applied to the system, such as constant temperature, then the velocities at $t = t_0 + \delta t$ must be corrected accordingly. Further, we can calculate $\ddot{\boldsymbol{x}}(t_0 + \delta t)$ from Eq. 2.39 based on the new atomic positions obtained, and feed it to Eq. 2.40 constructed for the next time step. Repeating this process n times we come up with the trajectories of all atoms in the system as a series $\boldsymbol{x}(t_0), \boldsymbol{x}(t_0 + \delta t), ..., \boldsymbol{x}(t_0 + n\delta t)$ for a total duration $n\delta t$. Additionally, at any time step one can calculate any variables of interest, such as energy of the system, virial, etc. This is a very simplified example of a general MD

algorithm, but it is enough to understand the main idea. Usually, this part of the calculations is already implemented in the software one chooses to perform the simulations with. A better insight is available in the classical textbooks [80, 84].

Before proceeding with the more hands-on part of the numerical simulation process, we need to address another important feature, which is a simulation box. Obviously, samples in real experiments most often contain enormous number of atoms, for a crystal it could be at a level of Avogadro constant, which is too much for any modern computer to simulate. Therefore, instead of simulating the whole sample, we can utilise the repetitive nature of a specimen and study a small representative volume. If the system is ergodic, which it usually is, then by simulating large enough time frame and letting the particles explore all the possible configurations, the averaged over time statistical parameters will be the same as ensemble averaged, which are observed in an experiment. Thus, in the calculations we consider that the sample is infinitely large, but consists of completely identical blocks. This way it is not necessary to simulate the whole sample, instead, it is enough to consider only one block and its nearest copies in all three dimensions, which we will call "phantoms". There are different approaches to how to model interaction of the particles in a "real" volume with the ones from the phantoms. These approaches are called periodic boundary conditions (PBC). All of them, however, have one thing in common, and it is the conservation of the number of particles. If any atom leaves the real simulation box and enters a phantom, then, due to symmetry, the same atom must enter the simulated box from the opposite side. This ensures that the number of simulated atoms is constant. The potential cut-off distance defines how far an atom "senses" other atoms. The simplest PBC method is called the "minimum image convention". In this case we virtually put a "cage" on a particle, with the former having the same size and shape as the simulation box. The particle now is only allowed to interact with other atoms, the centres of which lie in this cage. For short range forces spherical potential cut-off can be utilised, further decreasing the number of pairwise interactions to be considered. The periodic boundary conditions are natural for crystalline materials, but for the others, disordered substances, they are usually detrimental. In this case the simulation box must be sufficiently larger that the cut-off distance to prevent any potential perturbation on a particle caused by its copy. For further reading, a comprehensive and compact explanation of periodic boundary conditions may be found in [84].

Previously we considered that the forces between all the atoms in the system are known. In fact, they are not known, but rather chosen by the person performing the simulations based on prior knowledge about the system or its parts. The set of forces together with their corresponding parameters is called a force field (FF). The idea under choosing a proper force-field is that it must correctly reproduce all the desired behaviour of the system, while remaining as simple as possible.

Here we will switch from forces to energies, since they are easier and more common to work with. In these notations the force field is a parametric expression defining the energy of the system as a function of the positions of its particles $\mathcal{V} = \mathcal{V}(\boldsymbol{r}_1, \boldsymbol{r}_2, ..., \boldsymbol{r}_N)$ [85]. For example, a FF equation may look like this:

$$\mathcal{V} = \sum_{bonds} \frac{1}{2} k_b (r - r_0)^2 + \sum_{angles} \frac{1}{2} k_a (\theta - \theta_0)^2 + \sum_{torsions} \frac{V_n}{2} [1 + \cos(n\phi - \delta)] + \sum_{improper} \mathcal{V}_{imp} + \sum_{LJ} 4\varepsilon_{ij} \left(\frac{\sigma_{ij}^{12}}{r_{ij}^{12}} - \frac{\sigma_{ij}^{6}}{r_{ij}^{6}} \right) + \sum_{elec} k_e \frac{q_i q_j}{r_{ij}}, \quad (2.41)$$

where the first four terms describe the energy of intramolecular interactions (bond stretching, angle bending, and dihedral and improper torsions), and the last two represent van der Waals and Coulombic forces[5] [85]. Each item in Eq. 2.41 contains not only the variables describing geometrical relations between atoms, but also specific parameters, which are usually obtained in experiment or via DFT or *ab initio* MD calculations. Eq. 2.41 is only one example of what a force field expression could look like. For some application, for instance, a 12-6 Lennard-Jones (LJ) potential is not suitable, and a modified version is used instead [86]. Theoretically, each particular system of atoms may require its own force field, differing in interaction terms or corresponding parameters. However, as it was mentioned before, classical molecular dynamics are not expected to yield fully realistic picture of atomic motion, since its fundamentals do not allow to describe quantum mechanical effects. Therefore, the objective set for a force field is to approximate real interactions by means of a relatively simple mathematical expression. Obviously, in this case, one equation may suit a range of different systems.

[5]The reader can find explicit representations of each term and explanation of parameters in [85]. However, for the understanding of the current work it is not required.

The larger this range, the more corrections are required for the parameters in order to maintain adequate accuracy.

Today, there is a large variety of available force fields for different kinds of applications [85]. Universal force field (UFF) [87] claims to have parametrised the whole of the periodic table, but lacks precision of the specified force fields and hence, should be used with caution. Popular FFs for the simulations of proteins are AMBER [88] and CHARMM [89]. CFF [90] and COMPASS [91] are often used for condensed matter studies. Usually, when approaching the process of force field selection, one can find examples of MD simulations on the interested material in the literature, which hints at the FF that can be used. Also it may be possible to find DFT calculations reporting the refined force field parameters, which should be used to further tailor the FF for the particular material. It is beneficial to additionally test several suitable force fields and, perhaps, compare their results with experimental data. This is usually done by performing geometry optimisation (GO) of all the parts of the simulated system separately without fixing the atomic positions or unit cell parameters[6]. Ideally, structural parameters should not deviate from those initially set according to the literature.

Another important feature to be chosen before starting the simulations is the thermostat. The Eq. 2.39 keeps the total energy in the system constant. However, the potential cut-off, as well as the calculation errors (rounding), may induce fluctuations in the temperature, which accumulate over the course of the simulation and cause slow temperature drift. Such behaviour is usually undesirable if the calculations are to be compared with an experiment, where the temperature is maintained at a set value, therefore, to overcome this issue one has to correct the kinetic energy of the system, i.e. scale velocities. Different scaling techniques are called thermostats. At first glance it may seem that a simple solution of scaling the velocities by a factor $\sqrt{T_0/T(t)}$ is enough, where T_0 and $T(t)$ are the desired and instantaneous temperatures, respectively. However, this rigid approach is non-physical and leads to being unable to sample the true canonical ensemble [85]. A more gentle solution was proposed by Berendsen et al. [92], which consists of creating a weak coupling of the system with a heat bath by modifying the equations of motion. To first order approximation this leads to the scaling

[6]For example, if the studied system is a molecule trapped in a crystalline material, then the GO should be carried out separately for the molecule and the crystal.

factor λ:

$$\lambda = 1 + \frac{\delta t}{2\tau}\left(\frac{T_0}{T} - 1\right), \tag{2.42}$$

where δt is the time step and τ determines the strength of the coupling and, thus, can be varied. This method ensures that the Maxwellian velocity distribution is conserved, however, is can still affect the dynamics of the system when small τ is used, while large τ means weak control over the temperature. As usual, there is no "one solution fits all", and many different thermostats are available, the choice of which depends on the particular system under study. Apart from the already described, the other popular thermostats are the Andersen [93], Nosé-Hoover [94, 95] and Nosé-Hoover-Langevin (NHL) [96] thermostat. In a similar fashion there exist barostats for simulations under constant pressure.

To sum everything up, here are the steps one usually follows to set up the classical MD simulation.

1. Search for the literature, maybe someone has already done what you are trying to accomplish. Otherwise, look for the simulation parameters used for the system / parts of the system under study.

2. Set up the system. Either find the Crystallographic Information File (.cif) or an alternative from the databases[7], or construct it by yourself with the help of literature reports. The structure must be large enough to accommodate the anticipated dynamics. Take into account the periodic boundary conditions.

3. Choose a valid force field (or several, for a test), thermostat, time step, cut-off radius and other parameters proposed by the software / MD code that is utilised. If needed, manually apply charges and force field types to the atoms in the system. Test the set up by running geometry optimisation on all the parts of the system and comparing the results with the literature.

4. Relaxation step. Imagine that for diffusion studies we inserted a molecule into a porous material. Most probably the created system will not be in the minimum energy state, but will strive towards it. By

[7]Look up https://www.iucr.org/resources/data/databases

starting the MD simulations right away we would obtain large temperature fluctuations, and the dynamics will be unpredictable. Therefore, first we need to relax the system for it to come to an equilibrium.

5. Run the MD simulations. With all the parameters set and the system in equilibrium, it is the time to start preparing the trajectories calculation. The simulation time frame must be larger than the characteristic relaxation time of the processes under study, and the time step should be sufficiently small (usually of the order of fs) to ensure correct simulation of the fastest motion modes present in the system, such as vibrations. Also the time frame must ensure the validity of the ergodic hypothesis, i.e. time average of a given property of the system is equivalent to ensemble average. Sometimes it is possible to choose the frequency of extracting the trajectories. For the sake of saving computer memory space, as well as speeding up the simulations a bit, one should not choose to extract the trajectories at every simulation step, since such precision is rarely needed. It is enough to perform extraction every 10 or 100 steps, depending on the time step and time frame.

6. After we obtained the desired results from the MD simulation, i.e. atomic trajectories, which include the evolution of positions, velocities and forces over time, these results need to be further analysed. This final step depends on a particular application. One may want to calculate statistical properties of the system, or simulate an experimental spectrum and compare it with the real experiment.

Here we only gave a brief and compressed introduction to classical molecular dynamics simulations. A more detailed manual covering various applications was produced by M.A. González [85]. Information about the underlying physics is brilliantly presented in [84], and the algorithms are well described in [80].

Molybdenum disulphide single crystals

Chapter 3

$H^+(H_2)/MoS_2$

3.1 Résumé

The idea of this study was to load MoS_2 single crystals with hydrogen via a method, which is used in industry, i.e. electrolysis, for further investigation of hydrogen dynamics. Four experimental techniques were used here, namely, quasi-elastic neutron scattering (QENS) as the main tool to study hydrogen dynamics, neutron spin-echo (NSE) to expand the examination to larger length-scale, X-ray photoelectron spectroscopy (XPS) to get an insight into surface chemistry under hydrogen dosage via electrolysis, and nuclear reaction analysis (NRA) to obtain hydrogen concentration profile, as well as the parameters of diffusion through the MoS_2 layers in a very large timeframe. It was expected, that QENS would allow the distinction of different hydrogen species, that could be present in the sample. However, the situation appeared to be much more complex. Careful mutual consideration of the results of all experiments points at hydrogen molecules to be the main source of the spectroscopic signal. They exhibit fast motion parallel to the MoS_2 basal planes with diffusion coefficient D around $4 \cdot 10^{-8}$ m^2/s. NRA revealed an extremely slow drift of hydrogen towards the bulk, however, with only the available experimental data it is not feasible to tell, in which form does hydrogen penetrate the MoS_2 layers. Within the manuscript this study serves not only the purpose of reporting the information obtained, but also as an in-depth introduction to the problem of hydrogen diffusion in MoS_2.

3.2 Experimental

3.2.1 Sample preparation

For the study of hydrogen dynamics molybdenum disulphide single crystals with a thickness of about 0.2 mm and edge lengths between 6 and 15 mm were obtained from PLANO (PLANO GmbH Wetzlar, Germany, distributor of SPI, USA). Hydrogen loading via electrolysis (see section 2.1.1 for details) was performed several times, prior to every experiment. For nuclear reaction analysis (NRA) one MoS_2 single crystal was loaded with hydrogen shortly before the experiments, and for the XPS study four days in advance. Neutron studies require a larger volume of material and therefore all 10 single crystals were used. They were hydrogen loaded 4-6 days prior to the experiments. The loading procedure was the same for every experiment with slight variations in the duration of the process. Those samples that had been used in experiments before were degassed at temperatures > 750 K. Prior to each loading all MoS_2 single crystals were cleaved by peeling off the surface layer using adhesive tape. Then the crystals were mounted onto a tantalum plate electrode and subsequently loaded by electrolysis in a 1:1 mixture of phosphoric acid (H_3PO_4 85 %) and glycerol, using a Pt counter electrode. The electrolysis lasted 2 hours at 4 V on one side of the crystal for the nuclear reaction analysis, 4 hours at 4 V on one side for XPS and 4 hours at 3 V on each side for neutron experiments, since at this point it was tested that 3 V is enough to incorporate hydrogen into MoS_2 crystals. Lower voltage is preferential in our experiments since it is more gentle to the surface.

3.2.2 Nuclear reaction analysis

Hydrogen depth profiles were measured by irradiating the sample with a ^{15}N ion beam and counting the emitted gamma-rays on the beamline NRRA[1] [72] (Nuclear Resonant Reaction Analysis) at RUBION, Bochum, Germany. The underlying reaction is:

$$^{15}N +^{1} H \rightarrow^{12} C + \alpha + \gamma,$$

with a narrow resonance at the energy of 6.4 MeV, which is used for the detection of hydrogen. In order to reach the resonance energy at different

[1] https://www.rubion.rub.de/en/methods/nrra-nuclear-resonant-reaction-analysis/

depths inside the sample, the beam energy was varied from 6.39 MeV to 6.65 MeV. The maximum beam current was set to 6 nA. Data were collected in two runs, shortly after loading the sample with hydrogen and after four weeks downtime. During the waiting time the sample was held in air under ambient conditions. The depth scale in nm was calculated on a basis of the stopping power of MoS_2 [71]. The concentration scale was constructed taking into account the stopping power of both MoS_2 and hydrogen. More details on the method are given in section 2.3.

3.2.3 X-ray photoelectron spectroscopy

XPS surface characterisation was carried out on the HE-SGM station [97] at the BESSY II synchrotron, Helmholtz-Zentrum Berlin (HZB), Germany. The XPS signal was collected with a Scienta R3000 XPS analyser. The pass energy was set to 50 eV in order to decrease the background. Excitation energies used were 650 eV for the oxygen 1s line, and 385 eV for the other elements. The energy binning step was set to 50 meV. Data were collected posterior to the sample being heated to several temperatures: 300, 400, 450 and 500 K, respectively. During heating the pressure in the analysis chamber rose due to desorption from the sample. Therefore we had to wait several minutes until the pressure dropped to a value appropriate for the XPS experiment. The measurements thus show the state of the surface several minutes after the sample was heated up to a certain temperature. For energy calibration the adventitious carbon peak at the corresponding temperature was used. The background was described by a Shirley step model [98]. The intensities were corrected for the atomic subshell photoionisation cross sections obtained by Yeh and Lindau [75]. Data treatment was performed using the XPST package within the Igor Pro software package (WaveMetrics, Portland, USA).

3.2.4 Time-of-flight neutron spectroscopy

QENS data were collected at the neutron time-of-flight (TOF) spectrometer TOFTOF [99] at the research neutron source Heinz Mayer-Leibniz (FRM II), Garching, Germany, at a wavelength $\lambda = 5$ Å. The samples were held in a flat aluminium sample cell. Two sample orientations, an in-plane and an out-of-plane set-up, were used in order to obtain information about dynamics parallel and perpendicular to the MoS_2 (0001) basal plane, respectively. For

both set-ups the surface normal (crystallographic c-axis) was within the scattering plane. For the in-plane set-up, the c-axis was turned by $\phi = 20°$ away from the direct beam direction, i.e., $\boldsymbol{Q}$ was within the basal plane exactly for a scattering angle $2\theta = 40°$ (Fig. 3.1). For the out-of-plane set-up we used $\phi = 110°$, i.e., again the momentum transfer was perpendicular to the basal planes at $2\theta = 40°$. The temperatures scanned in the out-of-plane set-up were 3, 100 and 300 K, whereas in the in-plane set-up data at 3, 50, 100, 200, 300, 400, and 500 K were measured. The spectra were measured consecutively with rising temperature up to 500 K and a further spectrum at 300 K in the in-plane set-up was measured after the last 500 K measurements to check for permanent changes of the sample upon heating to 500 K. Spectra at 3 K were used as a resolution function. Data reduction was performed using the Mantid software package [100]. Every spectrum was normalised to the beam monitor signal and, after deduction of an empty container spectrum, corrected by a vanadium spectrum to calibrate for variations in detector efficiency. Both empty container and vanadium spectra were measured at room temperature. All data were binned in energy transfer space from -10 to 3 meV with a step of 0.05 meV and in momentum transfer space from 0.05 to 2.35 Å^{-1} with a step of 0.1 Å^{-1}. A representative QENS scan of MoS_2 at 400 K in the in-plane sample geometry is shown in Fig. 3.2. No Bragg reflections or significant data reduction artefacts are observed. Further in the text the geometry specification is dropped out, by default referring to the in-plane set-up. Every reference to the out-of-plane set-up is indicated explicitly.

3.2.5 Neutron spin-echo measurement

Neutron spin echo measurements were performed on the NSE spectrometer IN11 at Institut Laue-Langevin (ILL), Grenoble, France [101], using the high signal set-up IN11C, which uses a 30° detector bank [102]. Here, we used a wavelength of $\lambda = 5.5$ Å for maximum signal. Following the same procedure as in the QENS TOF study, data were collected in two sample orientations with the surface parallel and perpendicular to the scattering vector Q. The spectra were normalised using a standard procedure: all data were divided by a spectrum that was obtained in-situ at 2 and 5 K for the in-plane and out-of-plane geometry, respectively. At these temperatures the system can safely be assumed to be static in the dynamic window of the spectrometer. The experiment covered a range of momentum transfers of $Q = [0.1 \text{ to } 0.7]$ Å^{-1} and sample temperatures up to 600 K.

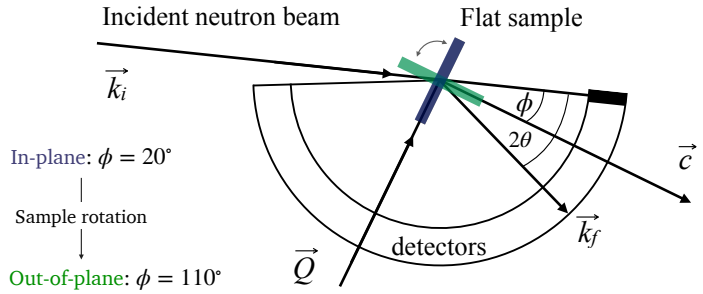

Fig. 3.1: Basic scheme of the experimental layout of the TOF neutron scattering experiment. The incident neutron beam with a wave vector $\boldsymbol{k}_i$ falls on a flat MoS_2 sample (dark blue) and is scattered in an angle 2θ with a final wave vector $\boldsymbol{k}_f$. For a defined angle ϕ between the incident beam direction and a normal to the sample's surface $\boldsymbol{c}$, there will exist an angle 2θ for which the momentum transfer vector $\boldsymbol{Q} = \boldsymbol{k}_i - \boldsymbol{k}_f$ is parallel to the MoS_2 basal planes, satisfying the in-plane scattering geometry condition. For the out-of-plane geometry the sample was rotated 90° counter-clockwise (green), i.e. $\phi = 110°$.

3.3 Results and discussion

3.3.1 Nuclear reaction analysis

We commence the description of our experiments with the structural and chemical characterisation of the samples: Fig. 3.3 shows the hydrogen concentration in dependence of the depth measured by NRA quickly after electrolysis loading of MoS_2 and after four weeks of ageing, respectively. For the freshly prepared sample the data clearly show a high concentration of hydrogen in the surface and sub-surface region and vanishing signal at higher depths (we note that the width of the surface peak is equal to the width dictated by the energy resolution of the incoming beam and, hence, the width of the surface peak gives only an upper limit for the width of the distribution function at the surface). After 4 weeks of ageing in ambient air environment, the surface peak decreased in intensity by half and a significant bulk signal was recorded that remained constant from a depth of 20 nm up to 100 nm, the maximum penetration depth recorded in our NRA measurements. Hence, the data show a diminution of hydrogen containing species in the surface layer and an increase of the concentration of hydrogen containing species in the bulk, which is a sign of hydrogen migration into the bulk of the crystal. After this first straightforward result, however, there remain two

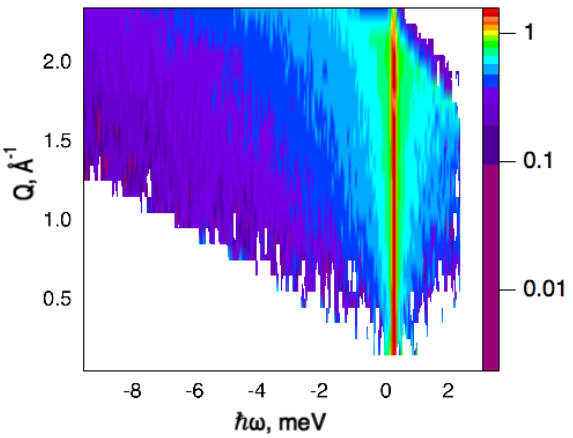

Fig. 3.2: Scattering function, $S(Q, \omega)$, of hydrogen loaded MoS_2 single crystals, measured at 400 K with the sample's basal planes oriented parallel to the momentum transfer vector Q. The plot uses a logarithmic intensity scale. Higher intensities are represented by red colour and lower intensities by blue. White area: no data, since it falls outside of the spectroscopic window.

important further questions: a) What hydrogen species do we have in this experiment and b) can we say anything about the diffusivity?

Considering the first question, one can imagine three hydrogen containing species that can be present in significant concentrations after the electrolytical loading: hydrogen atoms, hydrogen molecules and water. To distinguish between them, we have performed a test experiment with a sample as received and a sample that was exposed to pure water without electrolysis (Fig. 3.4). In these cases, we also obtained a surface peak at the start of the experiment, but no diffusion into the bulk over time. Therefore, we can conclude that water may contribute significantly to the surface signal, but does not penetrate across the basal planes into the bulk in a significant amount. The hydrogen containing species that are found in the bulk of the sample after electrochemical loading are, hence, hydrogen atoms or hydrogen molecules.

Any quantitative results extracted from the NRA surface peak must be discussed with caution, since the concentration scale is not fully applicable in that region due to several reasons, namely, hydrogen multilayer formation, surface contaminations and failure of the thick target approximation [72]. In the current experiment multilayer formation is not expected, however, light

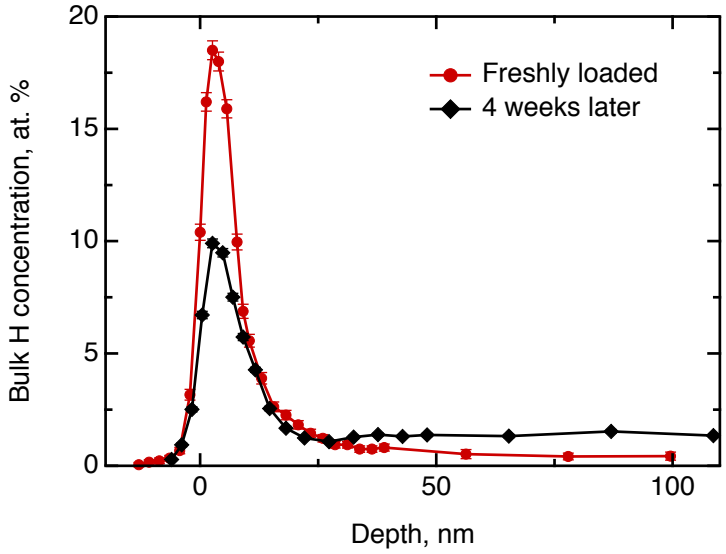

Fig. 3.3: Hydrogen depth profile in H loaded MoS_2 single crystals, measured by NRA shortly after loading (red curve) and after four weeks of ageing (black curve). The concentration scale applied to the ordinate does not apply to the surface peak.

organic contaminations may be present. Together with only partial validity of the thick target approximation this renders the concentration scale, to some extent, overestimated. Nevertheless, it is still possible to extract some information from the decay of the surface peak over time: We have demonstrated above, that only hydrogen molecules or hydrogen atoms diffuse into the bulk. This migration must lead to a loss in intensity of the hydrogen surface peak. Simultaneously, a gain in intensity may be observed due to a possible water adsorption from the atmosphere at ambient air conditions. Since during the ageing process the surface peak area decreased approximately by half, we conclude that several hours after loading process at least half of surface and subsurface hydrogen is in form of atomic and molecular hydrogen.

Now, we will try to analyse the diffusion in some more detail. The above considerations about the limited usability of the concentration scale in application to the surface peak concern mostly the depth profile up to ≈ 15 nm. Therefore the data beyond 15 nm can be used to extract some quantitative results. Fitting the data for the freshly loaded sample to the solution of Fick's second law of diffusion in the form of a Gaussian yields an order of

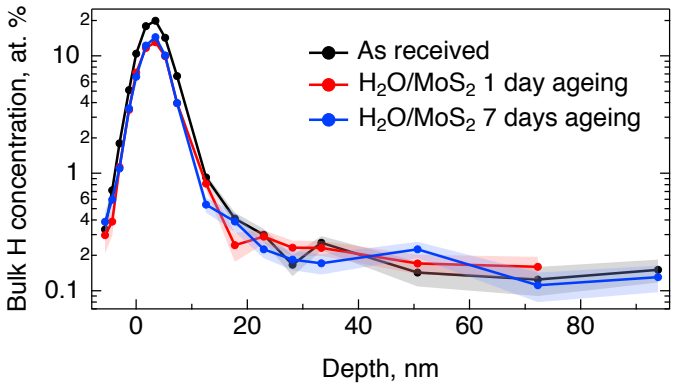

Fig. 3.4: Hydrogen depth profile in MoS_2 single crystals soaked in purified water, measured by NRA one day after loading (red curve) and after one week of ageing (blue curve). The not loaded, as received crystal is added as a reference (black curve). The concentration scale applied to the ordinate does not apply to the surface peak.

magnitude for the diffusion coefficient $D_\perp$ of $10^{-21}\ m^2/s$. Thus, the observed diffusion is extremely slow. However, even such a slow diffusion would result in almost uniform hydrogen concentration across the bulk after a 4 weeks ageing period, which is clearly observed in the data.

3.3.2 X-ray photoelectron spectroscopy

Prior to the neutron spectroscopy study of hydrogen diffusivity, see below, the chemical state of the MoS_2 surface was monitored by X-ray photoelectron spectroscopy at temperatures up to 500 K (Fig. 3.5). The XPS spectra reveal dramatic changes in the electronic structure of the MoS_2 surface upon heating. The splitting of the molybdenum and sulphur lines into two peaks each with almost identical areas was observed starting from 400 K up to the highest measured temperature 500 K, indicating the separation of the surface into oxidised and slightly reduced sections. These sections may be assigned to the surface and subsurface regions respectively. We note, that the analysis depths of the XPS experiment is limited to less than 10 nm [103], and in case of MoS_2 it can be estimated at a level of one S-Mo-S layer or slightly more [73, 74]. In view of the results of the NRA study, this covers the region, where we expect to find both water and hydrogen atoms or molecules. The analysis of the Mo and S binding energies suggests that at room temperature they correspond to clean MoS_2, i.e. Mo^{4+} and S^{2-} [104, 105]. This means

that surface chemistry changes that occurred in result of electrolysis smear out over time by electron migration from the bulk. This does not, however, mean that the surface is completely clean of any contaminations (see C and O lines in Fig. 3.5) or adsorbed hydrogen. Heating to 400 K partially reduces the surface, with Mo staying closer to the 4+ state than to 3+. Further increase in temperature prompts a new oxidation process, which results in a significant increase in the binding energy of the more oxidised state (labelled 2 in Fig. 3.5), causing Mo^{6+} to be formed at 500 K. The assignment of oxidation states remains tentative, however, since charging of the modified part of the surface may also have an impact on the observed binding energy. Keeping this reservation in mind we describe the occurring process as follows. During the loading procedure, apart from the production of -SH groups on the surface, a number of hydrogen atoms are incorporated into the bulk. At 400 K they become mobile and are subsequently bound also in the subsurface region, thus performing a reduction. At 450 K hydrogen atoms start to desorb from the surface, which leads to a surface oxidation. At the same time, as the H coverage on the surface decreases, subsurface hydrogen starts to migrate further to the surface, slowing down the surface oxidation and simultaneously oxidising the subsurface region. At 500 K the same process continues. It is also important to note that since MoS_2 is considered relatively active for the hydrogen evolution reaction, another source of subsurface H atoms apart from the bulk H exists, namely, catalytically split H_2 molecules. However in the XPS experiment little information can be drawn for hydrogen molecules, since they are not chemisorbed to the host material.

The XPS data contain also carbon and oxygen lines. Both elements are likely to be adsorbed from the atmosphere in various forms. Prior measurements utilising deuterium induced gamma emission (DIGE) at RUBION, Bochum, Germany, showed a bulk oxygen content at a level of 0.5 at. %. Hence, oxygen should mostly be located in the surface or subsurface region. The interpretation of the O 1s line requires a careful analysis: molybdenum oxides are expected to create an XPS signal around 530 eV [104, 105] and, thus, are not observed in this study. The other oxygen containing species that are expected in our samples and could be observable in the XPS spectrum are adsorbed water and organic molecules which contain oxygen bound to carbon in the form of $-CO_n$ groups. The binding energies of oxygen in these compounds are very similar and, therefore, cannot be resolved within the O 1s line. However, since the area under the peaks is proportional to the amount of corresponding C and O atoms in a sample, in first order approximation,

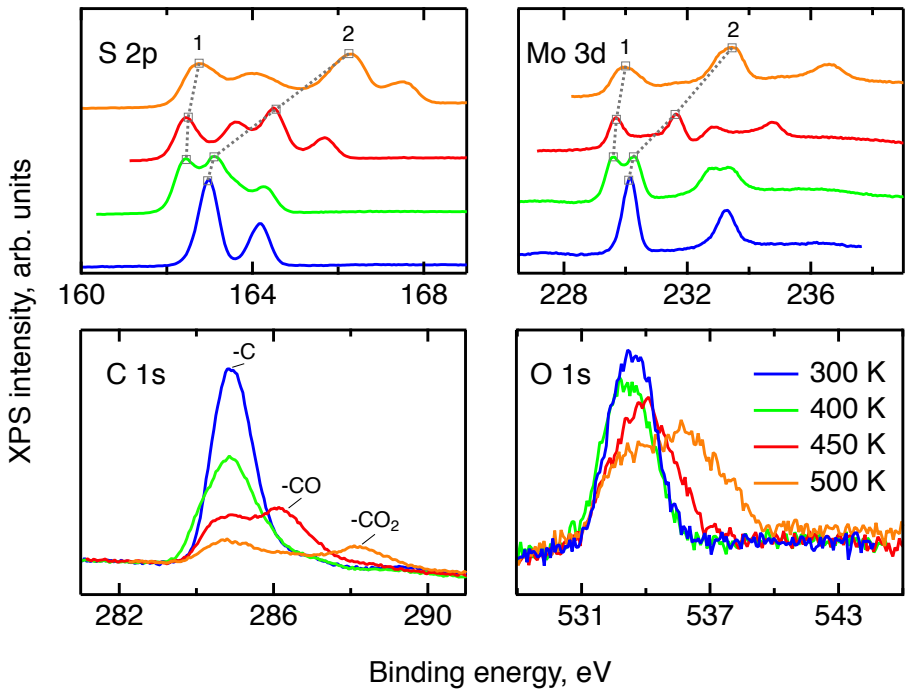

Fig. 3.5: XPS scans of various elemental lines for MoS_2 single crystals at different temperatures. From left to right: sulphur 2p, molybdenum 3d, carbon 1s and oxygen 1s. The temperature colouring is the same for all four plots: blue for 300 K, green for 400 K, red for 450 K and orange for 500 K. The grey dotted lines show the evolution of the binding energies of the two main oxidation states, labelled 1 and 2. For visual clarity a vertical offset is applied to the S and Mo data at elevated temperatures.

some information can be drawn from the behaviour of the C and O lines under temperature treatment. If every oxygen atom was bound to carbon, then the desorption picture, i.e. the loss of area under a peak, would be the same for both the O 1s line and the peaks corresponding to -CO and -CO_2. In our case no simple correlation can be established. Therefore it can be concluded that a significant amount of the observed oxygen is bound in water. As we have shown in the NRA study, however, this water has to be in the surface or subsurface regions. Additional XPS measurements of two MoS_2 single crystals loaded with hydrogen under the same conditions and heated to 500 K *ex-situ* showed a great difference between the areas of the corresponding O 1s lines. Given a very small measuring spot size (2×0.2 mm^2), the most probable cause of this effect is water agglomeration within volume defects. In this

case, the amount of oxygen seen in the XPS experiment would depend on whether the incoming X-ray beams hit the water agglomerate or not. The O 1s line splitting that appears at 500 K indicates that a large fraction of the water molecules transfer from a strongly adsorbed state to almost free H_2O molecules at this temperature [106, 107].

To conclude, the XPS study shows that chemisorbed hydrogen exhibits a thermally activated mobility in MoS_2 when the temperature of the sample is raised to 400 K or above. This leads to a chemical transformation of the sample as reduction and oxidation of MoS_2 can be observed. Strongly adsorbed water is also present to some extent in the surface or subsurface region up to elevated temperatures and becomes free at 500 K.

3.3.3 Quasi-elastic neutron scattering

The first subject that we aimed to address in the neutron scattering study was the impact of the layered structure of MoS_2 on the hydrogen dynamics. This should be observable through a difference between the quasi-elastic spectra obtained at different sample orientations, i.e., with the momentum transfer being parallel or perpendicular to the basal planes of the 2D samples (Fig. 3.6). In QENS measurements, the diffusive dynamics of sample atoms and molecules lead to a broadening of the elastic scattering line (around energy transfer $\hbar\omega = 0$) [32]. In our QENS spectra no systematic difference between the two sample orientations was found in the normalised data. This means that the properties of hydrogen diffusion parallel and perpendicular to the MoS_2 basal planes are mostly indistinguishable within the spectroscopic window of the present TOF QENS measurements. However, since the lowest exploitable Q values were relatively high (0.55 $Å^{-1}$), this finding does not put strict constraints on the model of hydrogen diffusion. Based on the structure of molybdenum disulphide we assume two possible diffusion patterns. In the first case hydrogen moves identically between the layers of MoS_2 and through the hexagonal wells (Fig. 3.6 inset), thus the length scale is of the order of the c unit cell parameter, i.e., 6.15 Å. The second possibility is a motion completely restricted by the sulphur planes, i.e., with no diffusion through the wells. In this case, the characteristic length of diffusion should be no larger than the gap between the sulphur planes of 2-3 Å. Fig. 3.6 displays the spectra at $Q = 0.85$ $Å^{-1}$, the momentum transfer for which the corresponding scattering angle best satisfies the in-plane and out-of-plane condition.

Now we turn to the in-plane data at various temperatures. Below 200 K

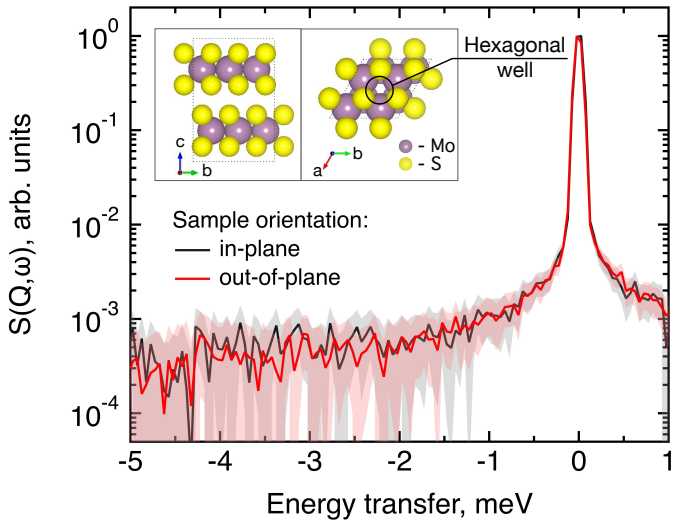

Fig. 3.6: Neutron quasi-elastic data obtained at T = 300 K, Q = 0.85 Å^{-1} and different orientations of MoS_2 single crystals versus momentum transfer vector. The in-plane geometry is represented by the black line and the out-of-plane geometry is represented by the red line. Error bars are displayed as a shading with a corresponding colour. The inset shows the structure of MoS_2, side-view (*bc* plane) on the left-hand-side and top-view (*ab* plane) on the right-hand-side. The visualisation of MoS_2 structure was prepared using the VESTA 3 software [108].

any hydrogen motion appeared to be too slow to fit into the spectroscopic window of the instrument, thus yielding no detectable quasi-elastic broadening (Fig. 3.7 a). At 200 K a clearly visible difference between the data and a resolution function occurs, however it is still too small to allow meaningful quantitative fits. A major gain in quasi-elastic signal takes place when heating the sample up to 300 K, and already at this temperature the QENS broadening exhibits clear signs of two different types of motion being present in the sample (Fig. 3.7 b). Taking into account their dependence on the Q vector, which will be discussed later, we interpret these two modes preliminarily as translational and rotational diffusion of hydrogen. The assignment of these modes to specific hydrogen containing species, i.e., hydrogen atoms, hydrogen molecules or water, is difficult. The NRA experiments demonstrate that water does not penetrate into the sample volume and that at least half of the hydrogen is in the form of atoms and molecules. The XPS measurements also show that water changes its binding energy only just below

500 K. Since in the QENS data no radical alterations are observed when heating from 400 to 500 K and since the neutron signal comes from the whole sample simultaneously, we conclude that water may not play a major role in the QENS signal. Now we consider if we can distinguish between the mobility of H_2 and H. Obviously, hydrogen molecules may exhibit both translational and rotational diffusion, whereas atoms are expected to show mostly translational motion, with a possibility of reorientations within S-H formation without breaking the bond. The XPS experiment indicates that H atoms start migrating to the surface at $\approx$ 400 K, whereas in the QENS data the quasi-elastic broadening can already be observed at room temperature, and no significant qualitative changes are observed when heating to 400 K. The above considerations hint that most of the QENS signal must arise from H_2 mobility, however, they are not entirely solid. In the next section, after analysing the data from the atom beam and water loaded samples, it will be more evident that in this experiment indeed H_2 makes the main contribution. Therefore, here we will continue our analysis considering that hydrogen molecules are the source of the QENS signal.

The whole set of data at temperatures higher than 200 K was treated by means of the rotational-translational model described in the QENS theory section 2.2.1 (Eq. 2.34):

$$\begin{aligned} S(\boldsymbol{Q},\omega) = S_0(Q)\cdot\{ & \\ & [\ S_{el}(Q) + (1-S_{el}(Q))A_0(Q)j_0^2(QR)\ ]\cdot R(Q,\omega) \\ & + [1-S_{el}(Q)]\cdot[A_0(Q)\sum_{l=1}^{3}(2l+1)j_l^2(QR)L(\Gamma_R^l,\omega) \\ & + (1-A_0(Q))L(\Gamma_T(\boldsymbol{Q}),\omega)] * R(Q,\omega)\} + Bkgr. \end{aligned} \quad (3.1)$$

Several spectra at low, below 0.85 Å^{-1}, and high, above 1.75 Å^{-1}, Q were not used in further analysis as the lack of data points in the QENS region (Fig. 3.2) made the corresponding analysis statistically unstable.

Based on the analysis of χ^2 values and on the behaviour of the residuals function (difference between observed and calculated points weighted for statistical errors) we conclude that our model is sufficient for the description of the data and no extra fitting parameters are required. The χ^2 values of the treated data set are distributed around 0.5 with a standard deviation of 0.1. The residuals functions for all spectra exhibit no systematic deviations from zero. The resulting fitting parameters are summarised in Tab. 3.1.

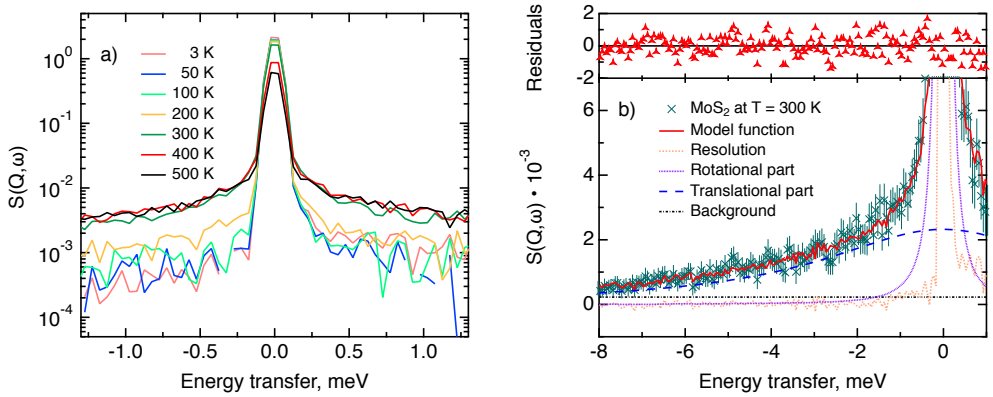

Fig. 3.7: a) Quasi-elastic neutron scattering scans of MoS_2 single crystals loaded with hydrogen, measured at a range of temperatures from 3 to 500 K at momentum transfer $Q = 1.35$ Å^{-1}. Statistical error bars are omitted for a clearer visualisation. b) Closer look at the 300 K data, which are represented by green crosses with error bars, and their approximation by means of a rotational-translational model (red line). Rotational and translational components are shown as purple and blue dashed lines, respectively, the light orange dotted line is the resolution function (hydrogen containing sample at 3 K) and a background term is shown as a black dash-dotted line. The residuals function (difference between measured and calculated points weighted for experimental errors) is displayed on top of the graph.

In the following we discuss the parameters of hydrogen diffusion in MoS_2 obtained by fitting Eq. (3.1) to the data. The change in the overall intensity $S_0(Q)$ at different temperatures that is shown in Fig. 3.8 a reveals that a significant fraction of hydrogen was desorbed during the first heating from 300 to 400 K (of the order of 50 %) and then from 400 to 500 K (an additional 10-20 %). This desorption happened rather fast during the heating and temperature equilibration phases, meaning that at the start of an actual measurement the system was already stable with no significant desorption observed during the accumulation of the spectroscopic signal (spectra in Fig. 3.7 a). Notably, the detected hydrogen loss did not impact the QENS profile, but only affected the overall signal strength. In order to evade possible re-adsorption during cooling down to 300 K the sample holder was not tightly closed to allow the desorbed gases to evacuate into the environment around the sample holder, which was held at low pressure during experiments. The low pressure itself does not drive significant hydrogen desorption, as was tested by monitoring the signal intensity during the measurements. Although in the QENS experiment substantial hydrogen desorption was observed between 300 and 400 K,

Table 3.1: Parameters of hydrogen diffusion inside MoS_2 single crystals at various temperatures. The asterisk represents data from the second heating run. Mean square displacement $< u^2 >$ was calculated via the Debye-Waller factor. τ_{rot} is the characteristic time of rotational diffusion. The radius of a confining sphere r_c was obtained by fitting Eq. 2.29 to the $A_0(Q)$ factor. Jump distance $d = \sqrt{< l^2 >}$ and residence time between jumps τ were estimated with the help of several models: Chudley-Elliot (CE), Singwi-Sjölander (SS) and Hall-Ross (HR) model. The subscripts denote, which model was applied for the corresponding numbers.

T, K		$< u^2 >$, Å^2		τ_{rot}, ps		r_c, Å
300		0.23 (1)		2.1 (4)		0.68 (2)
400		0.40 (1)		2.1 (3)		0.63 (1)
500		0.51 (1)		1.5 (3)		0.74 (1)
300*		0.32 (1)		1.7 (5)		0.71 (3)
T, K	d_{CE}, Å	d_{SS}, Å	d_{HR}, Å	τ_{CE}, ps	τ_{SS}, ps	τ_{HR}, ps
300	2.8 (2)			0.20 (1)		
400	2.1 (2)	2.6 (6)	2.2 (2)	0.29 (3)	0.19 (3)	0.26 (2)
500	2.3 (2)	2.9 (6)	2.5 (2)	0.32 (2)	0.22 (3)	0.29 (2)
300*	1.9 (7)	2.4 (16)	2.1 (7)	0.21 (8)	0.15 (6)	0.20 (5)

in the XPS study only a small reduction and peak splitting occur at these temperatures within the S and Mo lines, and minor intensity decrease in the O line. This indicates that the majority of the desorbed species could not be water molecules, nor could they be chemically bound to MoS_2 surface. Hence the observed large desorption should be attributed to weakly physisorbed, probably surface H_2 molecules. The Q dependence of $S_0(Q)$ allows us to estimate the level of hydrogen vibrations $< u^2 >$. The calculated values are moderate for the whole range of temperatures (Tab. 3.1).

The factor S_{el}, displayed in Fig. 3.8 b, shows the ratio of the scattering intensity off the immobile hydrogen and the host material, to the total scattering intensity $S_{el} = (I_H^{im} + I_{MoS_2})/(I_H^{total} + I_{MoS_2})$. The term "immobile" refers rather to atoms or molecules, whose movement is very slow and falls into the energy window of the resolution function, than to completely stationary particles. Although the incoherent scattering cross section of MoS_2 is very small as compared to hydrogen, it still may contribute to the S_{el} factor due to a larger number of scatterers, and thus it is taken into account in the further considerations. Hence, the decrease of S_{el} with temperature indicates that a part of immobile hydrogen either becomes mobile, i.e., becomes sufficiently fast to enter the spectroscopic window of the spectrometer, and

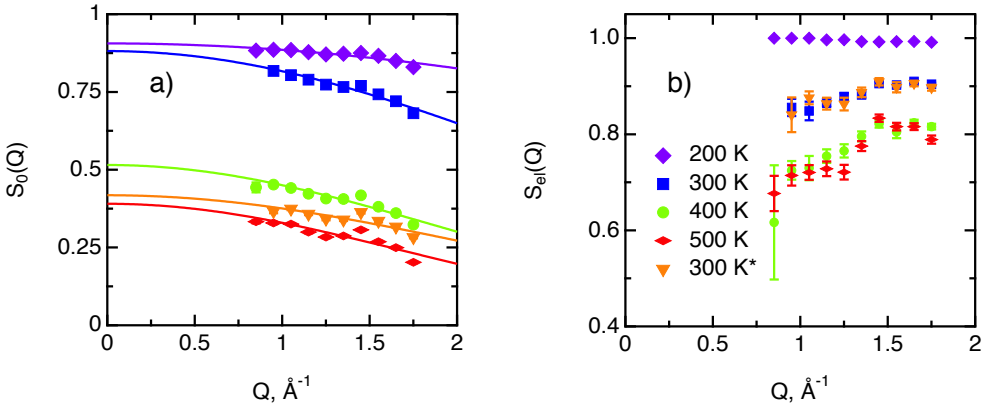

Fig. 3.8: Total neutron count characteristics of H/MoS_2 at different temperatures. The asterisk represents second heating run. a) The overall intensity factor $S_0(Q)$ (scale parameter times Debye-Waller factor) and its fit, represented by solid lines with corresponding colour. b) The ratio of elastic scattering to the normalised total neutron count $S_{el}(Q)$.

thus contributes to $1 - S_{el}$, or desorbs. Both room temperature runs, before and after heating to 500 K, give almost identical values of S_{el}. As no significant changes of S_{el} are observed between the two room temperature runs, it can be concluded that the balance between mobile H_2 and H atoms that are immobile at room temperature remains unchanged, which is in line with the above observations of H and H_2 desorption at elevated temperatures. During heating from 300 to 400 K the S_{el} factor drops and then remains similar upon heating to 500 K, indicating that heating from to 400 to 500 K does not induce any additional hydrogen to become mobile.

The decay of $A_0(Q)$ with Q (Fig. 3.9 a) shows the presence of a certain confinement effect beyond the natural confinement of the rotational diffusion. The approximation of $A_0(Q)$ with a model of a diffusion confined in a sphere (Eq. 2.29) [61] gives a good fit with a radius of confinement $r_c \approx 0.7$ Å, which is approximately twice as big as the radius of H_2 molecule. This length may indicate that hydrogen molecules are, to some extent, caged by four neighbouring sulphur atoms (the corresponding distance calculated on the basis of the MoS_2 structure is around 0.6 Å). In order to better understand the confinement effect two further EISF models were tested, namely, jump reorientations between two and three equivalent sites, respectively, equally spaced on a circle [32]. The fits of these models are of the same quality as for a spherical confinement model and yield a circle radius of around 0.6 Å,

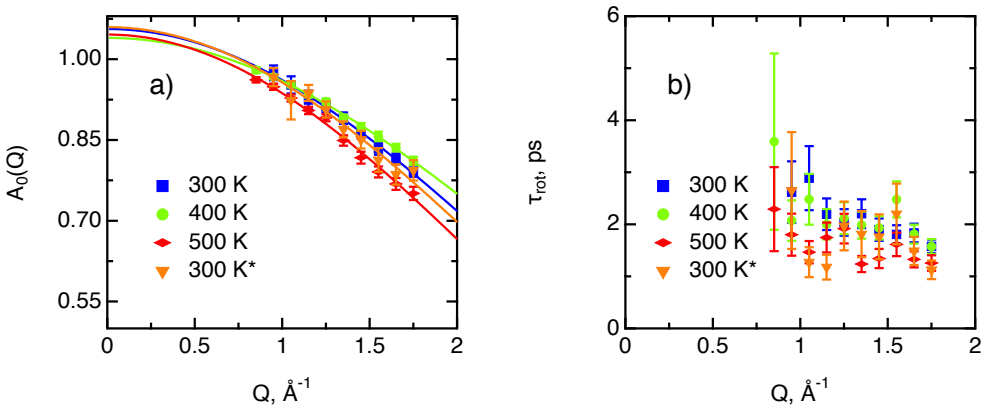

Fig. 3.9: Diffusion parameters of hydrogen in MoS_2 single crystals at various temperature. The asterisk represents second heating run. a) $A_0(Q)$ factor and its approximation using a model of translational diffusion confined within an impermeable sphere (Eq. 2.29). b) Characteristic time of rotational diffusion τ_{rot}.

very close to what was obtained with the previous model. This result is not surprising as for such a small confining length all the sensitive information should be contained in a high Q region, which could not be assessed in the current experiment, and hence, the specific geometry of the restricting potential could not be established. We would like to stress that the presence of this additional confinement length, in addition to the radius of the hydrogen molecule, does not exclude the existence of long range diffusion, because, in general, any potential of spherical symmetry would induce confinement effect [61], the restricting volume does not have to be fully impermeable, it must only put some constrains on hydrogen motion within it. For all three models extrapolations of the fit functions to $Q = 0$ Å^{-1} yield values of $A_0(0)$ slightly higher than 1, despite the fact that the expected value is less or equal to unity. This is an indication of the existence of various hydrogen containing species inside the sample. Indeed, if slow motion of atomic hydrogen falls into the energy window of the rotational mode of H_2, i.e. very close to the resolution function, it would increase the $A_0(Q)$ factor since the observed area of the rotational peak increases (see eq. 3.1). As expected the effect is minor as it is caused by the presence of atomic hydrogen. The characteristic time of rotation τ_{rot}, as theoretically expected, does not depend on the momentum transfer Q (Fig. 3.9 b).

The part of the quasi-elastic broadening that is caused by translational

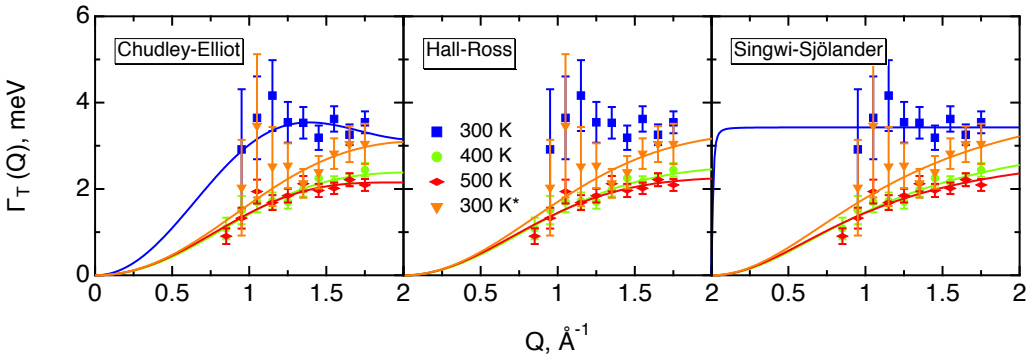

Fig. 3.10: Quasi-elastic broadening due to translational motion of hydrogen in MoS_2 $\Gamma_T(Q)$ plotted versus momentum transfer Q, represented by marks. And its approximated by different translational diffusion models, represented by solid lines: Hall-Ross, Singwi-Sjölander and Chudley-Elliot model for a hexagonal array of jump vectors. Data were collected at various sample temperatures, indicated by different colours in the plot. The asterisk represents the second heating run.

diffusion of molecular hydrogen exhibits a typical behaviour for a jump-diffusion process (Fig. 3.10) following a DQ^2 law at low values of momentum transfer and reaching a plateau at high Q [32]. As was observed earlier [109], diffusion models with a continuous distribution of jump lengths, like the Singwi-Sjölander [110] (SS) and the Hall-Ross [58] (HR) model, are well suited for treating such cases. Both were tested in this work, together with a general discrete-jump-diffusion model by Chudley and Elliot [57] (CE). The Singwi-Sjölander and Hall-Ross models consider different distributions of jump distances. The Singwi-Sjölander assumes an exponentially decaying distribution

$$\rho(r) = r/r_0^2 \cdot \exp^{-r/r_0}, \tag{3.2}$$

while in the Hall-Ross model the jump distances are distributed normally:

$$\rho(r) = \frac{2r^2}{r_0^3\sqrt{2\pi}} \exp(-r^2/2r_0^2). \tag{3.3}$$

The Chudley-Elliot model, on the other hand, considers jump diffusion between periodic discrete jump sites. In the case of a Bravais lattice, the HWHM of a translational Lorentzian can be derived from the following general expression:

$$\Gamma_{CE}(\boldsymbol{Q}) = \frac{4\hbar}{n\tau} \sum_{l_i>0} sin^2(\boldsymbol{Q}\boldsymbol{l}_i/2), \tag{3.4}$$

where n is a number of neighbouring jump sites and the summation goes over jump vectors $\boldsymbol{l_i}$ in a positive hemisphere. For the hexagonal MoS_2 structure it is reasonable to choose jump sites that are distributed with a hexagonal symmetry and a unique jump length l, since it was already shown that the diffusion should be isotropic. Hence, a jump site array was chosen in the form of a right hexagonal pyramid with a jump origin in the centre of the base and jump vectors pointing at the vertices.

At this point we should recall the geometry of the experiment. The in-plane set-up implies that a momentum transfer vector $\boldsymbol{Q}$ is almost parallel to the basal planes of the MoS_2 single crystals, i.e., $Q_\parallel \gg Q_\perp$. The SS and HR models assume isotropic diffusion, which implies that only the magnitude of the momentum transfer vector is relevant and the geometry of the experiment is insignificant. However, the CE model requires an averaging over all possible directions of $\boldsymbol{Q}$, which in our case requires an averaging over $\boldsymbol{Q}_\parallel$. By substituting the pyramid jump array into (Eq. 3.4) and averaging over $\boldsymbol{Q}_\parallel$ one gets an expression for the width of the translational broadening as displayed in the table below (see section 2.2.1 for details).

Singwi-Sjölander	Hall-Ross	Chudley-Elliott
$\Gamma_{SS}(Q) =$	$\Gamma_{HR}(Q) =$	$\Gamma_{CE}(Q) =$
$\frac{\hbar D_{SS} Q^2}{1+\tau_{SS} D_{SS} Q^2}$	$\frac{\hbar}{\tau_{HR}} \cdot [1 - e^{-\tau_{HR} D_{HR} Q^2}]$	$\frac{3\hbar}{4\tau_{CE}}[1 - J_0(Q_\parallel l)]$

Here, D is the diffusion coefficient, τ is the residence time between jumps and $J_0(x)$ is a zeroth order Bessel function of the first kind. The mean squared jump length and the diffusion coefficient are related by the Einstein equation [32] $D = \frac{<l^2>}{6\tau}$. The projection of $\boldsymbol{Q}$ in the current experiment can be evaluated as $Q_\parallel = Q \cdot \sin(\phi + \arcsin(Q\lambda/4\pi))$.

All three models describe most of the data equally well (in terms of a χ^2 test). However, the Singwi-Sjölander and Hall-Ross models did not succeed in treating the data obtained during the first 300 K run. The calculated jump distances $d = \sqrt{< l^2 >}$ and residence times τ are listed in Tab. 3.1. The first room temperature scan indicates a faster diffusion than all the others. This is due to weakly bound surface H_2 molecules, which, as we have shown earlier, desorb when heating the sample up to 400 K. Therefore, it would be appropriate to exclude the 300 K results for the first temperature run from further consideration. That being so, one can note a slight, but consistent correlation of the jump distance with temperature, which holds for every model. An averaged value of the jump length for all temperatures and models

is 2.3 Å. This value may be compared to certain characteristic distances in the MoS_2 structure and to the confinement length r_c, that was obtained from the $A_0(Q)$ factor. The calculated jump distance is significantly smaller, than the unit cell parameter of 3.15 Å, but close to the distance between two MoS_2 layers of 2 Å. It is also substantially larger, than the calculated confinement radius of 0.7 Å, which means that the observed jumps must happen between neighbouring confinement regions and not within them. As was described above, the restricting potential does not have to be impermeable for the confinement effect to be detected in a QENS experiment. It is also important to note that this jump distance is much less than the 6.15 Å interval between two layers of MoS_2. Therefore, what is observed in the QENS experiment is likely a movement completely restricted by the MoS_2 layers, rather than a diffusion through the hexagonal wells.

Since molybdenum sulphide is a promising catalyst for the hydrogen evolution reaction (HER), we would like to compare the parameters of hydrogen molecule diffusion in MoS_2 to the currently most active catalyst, platinum. Unfortunately spectroscopic information about hydrogen diffusion on Pt is only available for hydrogen atoms. It was obtained by Graham et al. [111] for a (111) surface of Pt by means of quasi-elastic helium atom scattering. We also add to the comparison the diffusion of hydrogen molecules on exfoliated graphite, studied by Bahn et al. [109] with quasi-elastic neutron scattering. Exfoliated graphite has not shown any significant activity in the HER reaction [112], but its layered structure is similar to MoS_2, hence it can be used as a reference non catalytic material. An Arrhenius plot of the temperature dependence of the diffusion coefficients of these three materials is displayed in Fig. 3.11. The diffusion coefficient for platinum was extracted via the Chudley-Elliot model, whereas the data for MoS_2 were averaged between the three models studied in this work (Table 3.2).

Table 3.2: Diffusion coefficient of hydrogen in MoS_2 obtained by means of three different diffusion models: Chudley-Elliot D_{CE}, Singwi-Sjölander D_{SS} and Hall-Ross D_{HR}; and an average over the models $< D >$. Here the 300 K results from the second heating run are shown, as an averaging over the models for the first run is not possible.

T, K	$D_{CE} \cdot 10^{-8}$, m^2/s	$D_{SS} \cdot 10^{-8}$ m^2/s	$D_{HR} \cdot 10^{-8}$, m^2/s	$< D > \cdot 10^{-8}$, m^2/s
300	2.8 ± 1.5	6.4 ± 5.0	3.6 ± 1.6	4.3 ± 2.7
400	2.5 ± 0.3	5.8 ± 1.5	3.2 ± 0.4	3.8 ± 0.8
500	2.7 ± 0.2	6.3 ± 1.5	3.5 ± 0.4	4.2 ± 0.7

The 300 K results from the first run were not used for this evaluation also because it was not possible to average over the models. The data for exfoliated graphite were extracted using the Singwi-Sjölander model. Interestingly, the diffusion coefficient of hydrogen atoms on Pt extrapolates quite well to the diffusion coefficient that was observed in the present study for hydrogen molecules at high temperatures. The diffusion coefficient of hydrogen on graphite, on the other hand, is substantially higher than the diffusion coefficient of hydrogen on MoS_2 if extrapolated to a similar temperature. Due to relatively large error bars in the calculation of the diffusion coefficient, we could not define with confidence the nature of its dependence on the temperature. The QENS broadening at 400 and 500 K, as well as the D coefficient, is the same within the range of statistical errors, which is an indication of an extremely small activation barrier, E_B. However, the data for the second heating run at room temperature suggest faster diffusion at 300 K, than at 400 and 500 K, although, due to rather weak signal, the statistical errors are so large that the comparison between the D coefficients at these temperatures becomes meaningless. Additional experiments with longer data acquisition time are required in order to confidently state whether the diffusion of H_2 in MoS_2 has the direct or inverted dependence of the D coefficient on temperature.

3.3.4 Neutron spin-echo study

Neutron spin-echo (NSE) experiments provide a direct measurement of the time evolution of the space correlation function of the sample (also called the intermediate scattering function $S(Q,t)$) [32, 113]. NSE data are complementary to TOF spectroscopy data, because they provide the Fourier transform with respect to energy and time of the TOF data. The spectroscopic window of the technique, in addition, allows the observation of dynamics with a characteristic time from ≈ 5 ps to several ns and therefore allows us to investigate the diffusion phenomena at lower Q values than the ones studied in the QENS experiment, i.e., testing substantially larger real space distances.

NSE spectra are shown in Fig. 3.12. Starting from 400 K the intermediate scattering function $S(Q,t)$ of the in-plane set-up shows a clearly visible decay that can be fit by an exponential law at $Q = 0.15$ Å^{-1}, which is an indication of diffusive motion parallel to the surface. We note, that an exponential decay found with NSE is equivalent to a Lorentzian line shape in the TOF

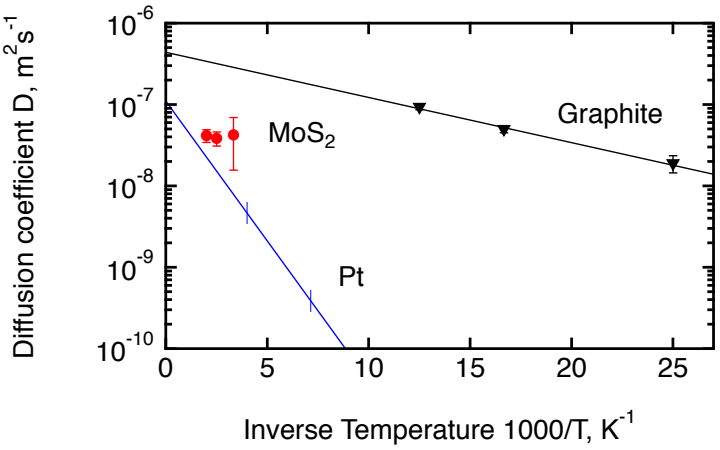

Fig. 3.11: Comparison of diffusion coefficients calculated in the current work for hydrogen molecules on MoS_2 (red circles) with the results obtained earlier for hydrogen atoms on platinum [111] (blue line) and hydrogen molecules on exfoliated graphite [109] (black triangles). Lines are calculated based on the activation energies and D_0 factors stated in the corresponding papers. Vertical lines for Pt show the range of measured temperatures. The diffusion coefficient at room temperature shown here for MoS_2 represents the second run.

experiment, because $S(Q,t)$ is the Fourier transform of $S(Q,\omega)$. In order to obtain the values of the diffusion coefficient, a DQ^2 law was used, since at low Q all the diffusion models described in the previous section reduce down to the DQ^2 law. Within the experimental error bar, we find similar diffusion coefficients through our NSE measurements as for the translational diffusion derived from the QENS data, i.e., $(1 \pm 1), (5 \pm 3), (4 \pm 2) \cdot 10^{-8}$ m^2/s at 400, 500 and 600 K, respectively. While we find a clear indication of diffusion parallel to the basal planes we observe that the signal in the out-of-plane orientation does not change substantially with temperature indicating that no significant diffusion is found perpendicular to the basal planes of MoS_2 within the spectroscopic window of QENS spectroscopy. We would like to stress that this observation is not in contradiction to the TOF findings (where we did not observe a difference between spectra parallel or perpendicular to the basal planes) because the smallest Q values that were exploitable in the TOF spectra represent distances that are in the range of the interlayer distance in MoS_2 of 6.2 Å. On the other hand, the distance corresponding to $Q = 0.15$ Å^{-1}, probed in the NSE experiment, is about 40 Å. It was not possible to measure the dynamics at higher Q values (above 0.15 Å^{-1}) using

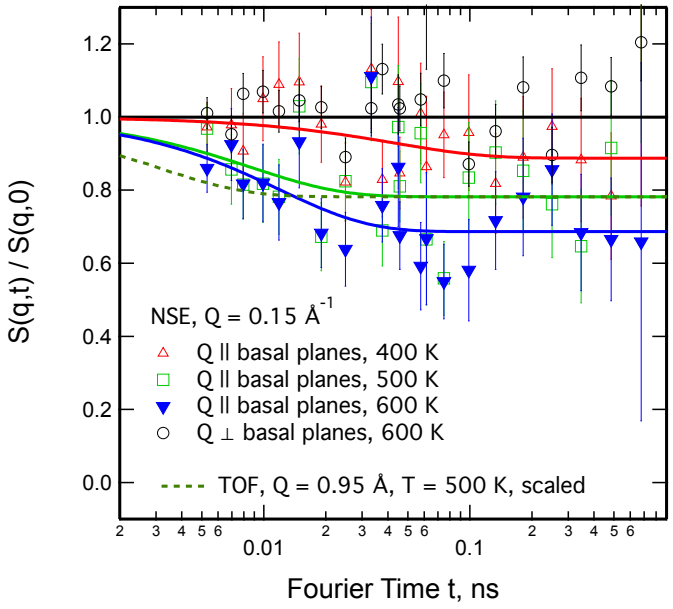

Fig. 3.12: Normalised intermediate scattering function as a function of Fourier time for a momentum transfer of $Q = 0.15$ Å^{-1} and Q vector parallel (red, green and blue) and perpendicular (black) to the MoS_2 basal planes. Markers represent NSE experimental points and solid lines with respective colour depict their fits with a scaled exponential law plus constant term. For comparison, the time Fourier transform of the translational diffusive contribution to the TOF QENS spectra is shown here as a dashed line. This line was scaled to have the same $S(Q, \infty)$ as the NSE 500 K fit curve. The NSE data have been normalised to the scans at the cryostat base temperature of 2 K.

NSE, because the neutron beam polarisation was destroyed by the incoherent scattering of the hydrogen for higher Q values: coherent scatterers leave the neutron spin unaltered upon scattering, whereas incoherent scattering atoms cause spin-flips upon interaction with the scattering neutron leading to a final beam polarisation after scattering of $P = -\frac{1}{3}$ on average [113]. We note, that rotational diffusion will not be visible at the low Q measured by our NSE measurement, since the intensity of the rotational diffusion vanishes at small Q [67].

3.4 Conclusions

In this study we have performed the analysis of hydrogen diffusion in the bulk of electrolytically loaded MoS_2 single crystals by means of quasi-elastic neutron scattering and neutron spin-echo spectroscopy. The results were compared to the currently most active HER catalyst platinum and a non-catalytic exfoliated graphite. A supplementary study of the surface chemistry of the MoS_2 under temperature treatment and ageing was carried out with the help of X-ray photoelectron spectroscopy and nuclear reaction analysis.

First of all, the nuclear reaction analysis has shown clear signs that hydrogen is able to penetrate the layered structure of MoS_2 and migrate from the surface to the bulk across the basal planes of this layered material, though rather slowly with a diffusion coefficient of the order of 10^{-21} m^2/s. The NRA and XPS data also showed that water does not penetrate into the bulk, but can be found adsorbed at the surface or subsurface layer. The QENS study showed a clear translational and rotational diffusion of hydrogen molecules and only a negligible contribution of hydrogen atom diffusion within the spectroscopic window of the present experiments. The low Q data from NSE spectroscopy demonstrated that the hydrogen diffusion between 300 and 600 K is limited to a motion constrained between the layers of MoS_2. The QENS data could be fitted by models that consider a restricted jump diffusion, where the jump distance and the restricting length are both smaller than 3 Å, supporting the idea that the diffusion observed here comes from hydrogen enclosed between the layers.

The calculated diffusion coefficients of hydrogen molecules in molybdenum disulphide were compared to the ones of hydrogen atoms in a catalytic platinum and of hydrogen molecules in non-catalytic exfoliated graphite. According to the Arrhenius plot (Fig. 3.11) the diffusion rate of H_2 in MoS_2 at room temperature or above is similar to the diffusion coefficient expected for hydrogen atoms on Pt at the same temperatures. The activation barrier could not be estimated due to relatively large statistic errors in the data, which do not allow to state clearly whether the dependence of the D coefficient of temperature has a direct or inverted behaviour.

Chapter 4

H and H_2O/MoS_2

4.1 Résumé

The study of the MoS_2 crystals loaded by hydrogen via electrolysis yielded a vast amount of information, but also a number of new questions arose, and some of the old ones were left with no answer. The results point at recombined H_2 to be the main source of the QENS signal, but the indications are indirect. The diffusion of H atoms is still to be examined. The absence of any type of simulations leaves a lot of space for the speculations around the interpretation of the data. In the further study we address these problems by examining the samples loaded with H and H_2O via more reliable methods. The H atom beam bombardment introduces mostly neutral H atoms into the MoS_2 matrix. Soaking in purified water should promote the adsorption of H_2O on the surface. Ideally we would expect to obtain motion parameters easily separated between the three hydrogen species. As it will be shown, this is achieved for the most part. Hydrogen atoms are found to move slower than other species, however, their motion parallel to the MoS_2 basal planes is mostly unobstructed. Water molecules tend to infiltrate various voids or cracks in the material, staying there until relatively high temperatures. Their motion resembles liquid water diffusion. Classical molecular dynamics simulations are also presented, yielding important pieces of information to support our interpretation of H, H_2 and H_2O diffusion.

4.2 Experimental

4.2.1 Sample preparation

Commercial MoS_2 crystals with a thickness of around 0.2 mm and area varying from 5 to 50 mm^2, obtained from PLANO (PLANO GmbH Wetzlar, Germany, distributor of SPI, USA), were used as a target material for hydrogen dosage. The crystals were divided into two sets. One set was loaded with H atoms via atom beam bombardment (see section 2.1.2), while the other one with H_2O via soaking in purified water (Milli-Q, Merck KGaA, Darmstadt, Germany) (see section 2.1.3). In the following, we will call the former samples H/MoS_2 and the latter H_2O/MoS_2.

For the atom beam preparation, a flat sample is first mounted onto a tantalum plate and fixed with tantalum stripes. Then the sample holder is inserted into a chamber, which is subsequently vacuum pumped until a pressure in the range of 10^{-8} mbar is reached. Afterwards, the sample is degased several times at temperatures from 750 to 850 K in order to eliminate any hydrogen remaining from previous experiments. When the sample temperature returns to 300 K the hydrogen loading commences. The valve to the H_2 source is partially opened to create a hydrogen gas flow into the chamber in a way, that under constant pumping the pressure in the chamber stabilizes at $3 - 5 \cdot 10^{-6}$ mbar. After this the tungsten filament, placed between the H_2 source and the sample, is heated to T $\approx$ 1900 K, which leads to the dissociation of a part of the H_2 molecules into atoms. Subsequently, hydrogen atoms impinge the MoS_2 crystals and get trapped inside the material. Here, we used a loading time of 2 hours. For the X-ray photoelectron spectroscopy measurements the crystals were prepared several days in advance, while for the neutron experiment the crystals were loaded from one side 3 months prior to the measurements, and from the other side one week in advance. Shortly before the neutron experiment the crystals were baked for 6 hours at 390 K, because the previous experiment with the electrolytically loaded crystals proved that a significant amount of weakly physisorbed H_2 molecules can be accumulated on the surface of MoS_2, which desorb at some point below 400 K. Since the idea of the current experiment is to isolate the diffusion of H atoms, the pre-baking was crucial to obtain clean MoS_2 surface. With this kind of pretreatment we inevitably lose also some amount of H atoms, however, the resulting H content was enough to obtain decent QENS profile, as will be shown in the Results and discussion section. The second set of

crystals was soaked in purified H_2O for several hours right before each measurement. Prior to mounting the water loaded crystals they were gently dried with a paper cloth to remove any excess water. Here the pre-baking was not necessary since H_2 was not present during the loading in any way.

The presence of hydrogen in the H/MoS_2 samples as well as the absence of possibly intercalated water in H_2O/MoS_2 have been proven by a hydrogen depth profile (Fig. 4.1) via nuclear reaction analysis ($^{15}N + ^1H \rightarrow ^{12}C + \alpha + \gamma$). The ageing measurements reveal the same diffusion coefficient for the migration of H atoms into the bulk, as for the electrolytically loaded samples. *In situ* NRA measurements also showed no hydrogen uptake by MoS_2 under H_2 flow with the filament switched off (Fig. 4.1). The experiments were performed at the beamline NRRA (Nuclear Resonant Reaction Analysis) at RUBION, Bochum, Germany.

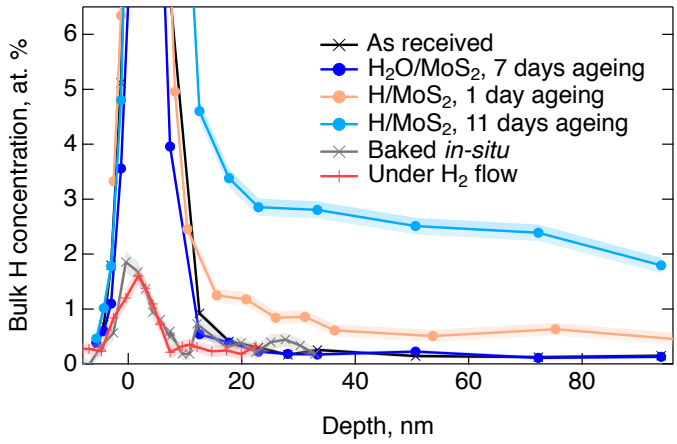

Fig. 4.1: Bulk hydrogen concentration depth profile for various specially prepared MoS_2 crystals. Black line shows the data for the crystals as received from the supplier. Blue line stands for the water loaded sample, scanned one week after loading. Light orange and light blue curves show the hydrogen concentration for H atom beam loaded crystal one day and 11 days after loading, respectively. Grey and red line represent the same sample, first baked at ~700 K *in situ* (grey), and than targeted by a jet of H_2 gas in the same conditions as for the H atom beam loading, but with the filament switched off (red).

4.2.2 X-ray photoelectron spectroscopy

The XPS measurements were performed on the HE-SGM station at the BESSY II synchrotron, Helmholtz-Zentrum Berlin (HZB), Germany, which

possesses a Scienta R3000 XPS analyser and a photon beam size of 2×0.2 mm^2. The pass energy for the collected electrons was set to 50 eV to reduce background. The excitation energy of the incoming beam for H/MoS_2 was set to 750, 500, 450 and 380 eV for the oxygen, carbon, molybdenum and sulphur lines, respectively, while for H_2O/MoS_2 it was fixed to 700 eV for oxygen and to 350 eV for all the other elements. We note that a difference in excitation energies between different experiments may slightly alter the resulting intensities of elemental lines due to a variation in the analysis depth, however, the effect is minor in our case. In order to monitor the changes of the surface chemistry upon hydrogen desorption the samples were exposed to temperature treatment *in situ*. Both specimens were heated up to 550 K, with XPS scans conducted at several intermediate temperatures. The XPS scans could not be conducted while the samples were at elevated temperatures, because the sample heating increased the chamber pressure to levels that were incompatible with the operation of the electron energy analyser and detector. Therefore, before each scan the system was left to rest for some time in order to let the pressure in the chamber return to operating values. The temperatures displayed in the graphs, therefore, represent the maximum temperature the crystal was heated to, and not the temperature during the measurement. A heavy desorption from the H/MoS_2 crystal did not allow to perform the whole treatment in one run, thus a second run was carried out to reach 550 K. Approximately 14 hours had to be skipped between the first and the second heating run for H/MoS_2. This issue will be addressed later in the results and discussion section. The analysis of the data was performed with the help of the XPST package within the Igor Pro software (WaveMetrics, Portland, USA). The energy calibration for each sample and each temperature was conducted by referring to the corresponding adventitious C 1s line at 284.8 eV. The background was treated by means of the Shirley step model [98] and the intensities were corrected for the atomic subshell photoionization cross sections [75].

4.2.3 Time-of-flight quasi-elastic neutron scattering

The prepared samples H/MoS_2 and H_2O/MoS_2 were measured on the neutron time-of-flight spectrometer IN6-SHARP at Institut Laue-Langevin (ILL), Grenoble, France [114]. The instrument operates based on a time-focusing TOF principle. For an optimal resolution-flux ratio neutrons of wavelength $\lambda = 5.12$ Å were used. The MoS_2 crystals were placed in a flat aluminium

cell, which was not vacuum tight to allow any desorbed gases to leave the system. The sample cell was inserted into an "orange" cryo-furnace [115] and positioned such that the MoS_2 (0001) basal planes were parallel to the momentum transfer vector. The geometry of the experiment was set identically to the previous study of electrolytically loaded crystals (Fig. 4.2), however, this time the out-of-plane data were not collected since it was shown that the exploited Q values (from 0.7-1 $Å^{-1}$) are larger than required to access the anisotropic features of the material. The influence of layered structure of MoS_2 on hydrogen diffusion must be examined by means of neutron spin-echo. Such experiment was performed, but, unfortunately, the amount of hydrogen in the atom beam loaded samples was not enough to extract any reliable information from the data.

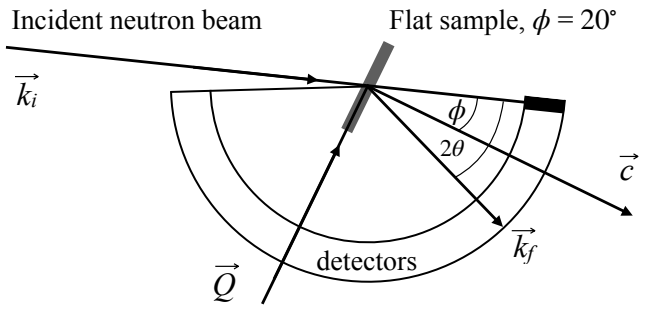

Fig. 4.2: Basic scheme of the experimental layout of the neutron scattering experiment. The incident neutron beam with a wave vector $\boldsymbol{k}_i$ falls on a flat MoS_2 sample and is scattered in an angle 2θ with a final wave vector $\boldsymbol{k}_f$. For a defined angle ϕ between the incident beam direction and a normal to the sample's surface $\boldsymbol{c}$, there will exist an angle 2θ for which the momentum transfer vector $\boldsymbol{Q} = \boldsymbol{k}_i - \boldsymbol{k}_f$ is parallel to the MoS_2 basal planes, satisfying the in-plane scattering geometry condition.

As it was mentioned before, the in-plane set-up allows to study the diffusion phenomena along the MoS_2 layers only. However, the perpendicularity condition cannot be strictly satisfied for each scattering angle simultaneously. The momentum transfer vector Q for which this condition is best fulfilled is the same as in the previous experiment and equals 0.85 $Å^{-1}$. For the largest Q values used in further analysis the ratio $Q_{\parallel}/Q$ reaches 0.8, meaning that the data at these Q values are, to some extent, influenced by the out-of-plane diffusion as well. Both samples were measured at several temperatures between 2 K and 500 K. The sample H/MoS_2 was additionally scanned at

the same temperatures after being heated to 500 K and cooled down to 2 K, to check for diffusivity changes after one desorption cycle. Data were reduced within the Mantid software [100] using the standard ILL reduction procedures, which include normalization to monitor, empty container subtraction and detector efficiency correction. The reduced data do not contain any major Bragg reflections (Fig. 4.3).

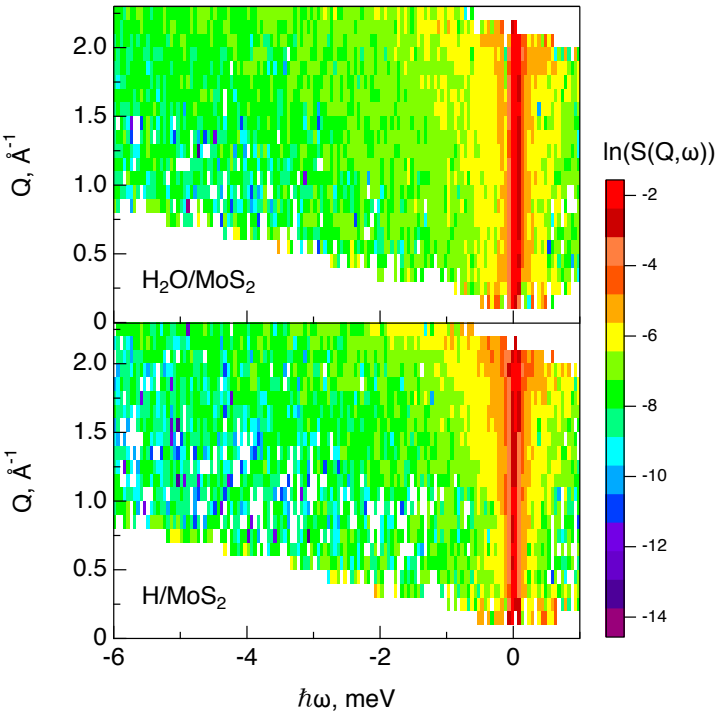

Fig. 4.3: The logarithmic dynamic structure factor $ln(S(Q,\omega))$ for H_2O/MoS_2 (top) and H/MoS_2 (bottom) measured at 400 K and plotted in identical scaling. No major elastic or inelastic peaks are observed.

4.2.4 Numerical simulations

Classical molecular dynamics simulations were performed using the Forcite Module of the BIOVIA Materials Studio 2020 suite (BIOVIA, Dassault Systèmes, BIOVIA Materials Studio, 20.1.0.5, San Diego, USA). The utilized forcefield is *pcff* [116] (version 3.1), which was modified according to Liu [73]. Non-default force field types and bonds were implemented for Mo

and S depending on their position within the structure (see Fig. 4.4). The partial charges were set to 0.5 for Mo and -0.25 for S. Considering the aims put for MD simulations in this work, i.e. assisting the interpretation of experimental data, the *pcff* forcefield is a decent choice in terms of utilisation ease and the amount of literature reports regarding MoS_2. However, as in was mentioned in the section 2.6, it does not allow the simulations of bond creation and breakage, which may be expected for H atoms in MoS_2. This, of course, must affect the simulated diffusion pattern and, hence, diffusion coefficient. However, the quantitative effect is not dramatic since the free hydrogen motion, i.e. while it is not bonded to sulphur, must obey classical laws. Therefore, as here our purpose is not to tailor out simulations to the experimental data, but rather gain a comprehensive visual picture of different hydrogen species movement in MoS_2, the *pcff* forcefield is sufficient for us. In order to describe the system more accurately and in more detail one has to use the reactive forcefields, like *ReaxFF* [81], which allow the creation and breakage of chemical bonds. There exist several studies of MoS_2 using *ReaxFF* [117, 118], which may help in determining the proper initial parameters for commencing the simulations.

The initial MoS_2 structure was obtained from the ICSD database with a collection code 24000, which is referenced to the work by Dickinson and Pauling [119]. The original hexagonal MoS_2 structure was redefined into an orthorhombic set-up by transforming the unit cell vectors via a = (0, 1, 0), b = (1, 1, 0) and c = (0, 0, -1). Hydrogen species were simulated using the default *pcff* force field types *h+* for protons and neutral H atoms, with a set charge of 0 for the latter, h with 0 set charge for H_2 molecules, and *hw* for hydrogen in H_2O. The simulation of both H and H^+ serves the purpose of accessing the influence of charge on the diffusion characteristics of atomic hydrogen. The charge for H^+ was set to 0.9, while in the case of water, the partial charges had been assigned automatically by the force field, approximately 0.4 for hydrogen and -0.8 for oxygen. Additionally, the H_2O molecule underwent a geometry optimization procedure.

For a simulation of hydrogen diffusion on a surface, a 7 × 4 supercell consisting of 7 MoS_2 layers was constructed, which was merged with a 30 Å height vacuum slab, resulting in 1212 atoms in total. The 4 topmost layers were relaxed and the others were set fixed. Further, five hydrogen atoms, five ions or three H_2O or H_2 molecules, respectively, were randomly placed near the surface, and the final system was subjected to geometry optimization with fixed cell volume.

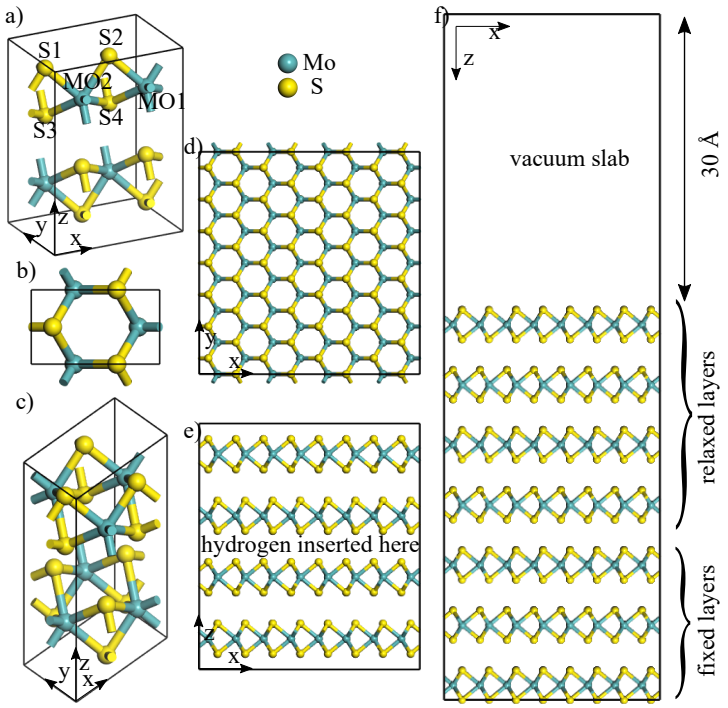

Fig. 4.4: a) The configuration of MoS_2 for the validation of the force fields. The labels are the force field types assigned to each atom. b) Top view of c) orthorhombic configuration of MoS_2. d) Top view of the configurations that were used to simulate diffusion of hydrogen. e,f) Side views of the configurations for the bulk and surface MoS_2 simulations, respectively.

For hydrogen inside MoS_2 a $7 \times 4 \times 2$ supercell was used, with hydrogen species placed in the middle interspace of the 4-layer structure. Here, during the geometry optimization the unit cell was optimized as well. The resulting unit cell parameters remained almost unchanged.

4.3 Results and discussion

4.3.1 X-ray photoelectron spectroscopy

The surface chemistry of the hydrogen containing MoS_2 samples was characterized using XPS from room temperature up to 550 K. XPS allows us to identify changes of the sample chemistry due to the chemisorbed hydrogen and to test its influence on the surface oxidation state during hydro-

gen desorption. Pronounced chemical changes were expected for the atom beam loaded sample, H/MoS_2, while the sample that was soaked in water, H_2O/MoS_2, was anticipated to deviate only slightly from a clean MoS_2 sample, since water is not expected to bind chemically to the MoS_2 surface.

As expected, the XPS spectra of H_2O/MoS_2 at room temperature exhibit an almost clean surface evidenced by the binding energies of S and Mo [104, 105] (Fig. 4.5), with a slightly reduced sulfur. With increasing temperature the S 2p and Mo 3d peaks of H_2O/MoS_2 first shift to lower binding energies between 300 and 400 K, indicating a very weak reduction process, and then remain unchanged at higher temperatures. On the other hand, during initial heating from room temperature the oxygen and carbon lines undergo a noticeable transformation (Fig. 4.6, 4.7). The oxygen peak, the assignment of which to a specific compound will be discussed later, shifts to lower binding energies and slightly drops in intensity (Fig. 4.6). The carbon line consists of 4 peaks, positioned approximately at 284.8, 285.5, 286.9 and 288.8 eV, respectively (Fig. 4.7), with the last one having insignificant intensity. The first peak is attributed to adventitious carbon and acts as the binding energy reference of the present study. The second one can be assigned to carbon in C-O-C configuration within organic molecules. Such organic molecules can be adsorbed from air while mounting the sample. The third peak possesses a binding energy, which can be exhibited by a number of different compounds, and therefore its assignment is ambiguous. One of the possibilities is carbon bound to sulphur in a S=C=S configuration [120]. The last peak at 288.8 eV could be yielded by carbon in O-C=O, however, as it was already mentioned, the peak's area is negligible as compared to the other peaks. When heating the specimen from 300 to 400 K, the weight of the C-O-C line reduces almost by half, meaning that a large number of carbon atoms, which are probably bound to oxygen, are desorbed. At the same time, the O 1s line does not significantly decrease in intensity between these temperatures, i.e., we observe a lack of correlation between the changes of the areas under the peaks of O 1s, A_{O1s}, and C-O-C, A_{C-O-C}, upon heating. This suggests that most oxygen atoms are not bound to carbon at room temperature, if we assume a near linear relationship between the XPS area and the number of corresponding atoms. During heating, the ratio A_{C-O-C}/A_{O1s} takes the values 1.8, 1.4, 1.2, 1.6, 1.6 at 300, 400, 450, 500 and 550 K, respectively, meaning that below 500 K the correlation is not observed. The O 1s line could also be yielded by molybdenum oxides, however, in this case, the corresponding binding energy is expected to lay

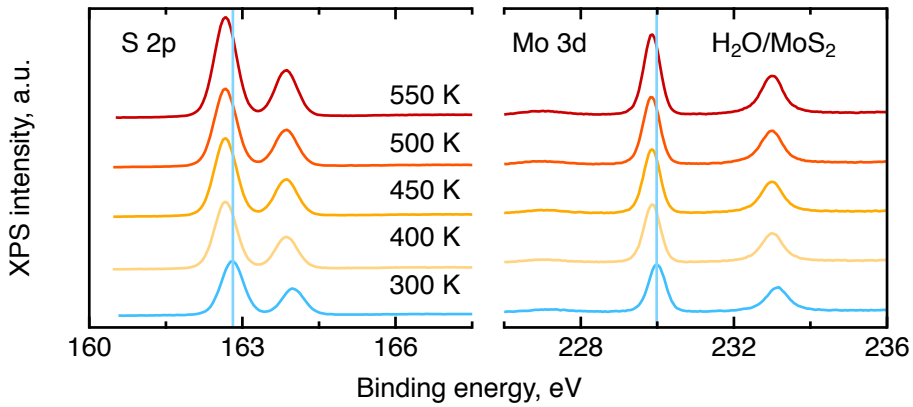

Fig. 4.5: X-ray photoelectron spectroscopy scans of the S 2p and Mo 3d elemental lines of H_2O/MoS_2. The data were acquired at several temperatures from 300 to 550 K, which are indicated by different colours. For visual clarity vertical offset is applied to each spectrum. A blue upright line shows the position of the corresponding peak at room temperature. The displayed temperatures are the ones the sample was heated to and are slightly higher than the temperature during measurement.

around 530 eV [104, 105], a spectral position at which no significant signal is detected in our experiment (Fig. 4.6). Therefore, we conclude that, at least below 500 K, the oxygen line, observed for the H_2O/MoS_2 crystal, is yielded mostly by water, adsorbed during the loading process.

Now we continue with the interpretation of the molybdenum and sulphur chemistry through the XPS spectra for H_2O/MoS_2. The shift of the oxygen, sulphur and molybdenum lines to lower binding energies, occurring when heating the sample from room temperature to 400 K can be associated with the significant desorption of C-O-C containing molecules. Further, at higher temperatures, no significant changes are observed for the S 2p and Mo 3d lines, despite a considerable water desorption between 450 and 500 K. Therefore, since the alterations in the O 1s peak do not affect the chemistry of the host material, it can be concluded, that water should only be physisorbed within MoS_2. Physisorption, in contrast to chemisorption, means that a sorbed H_2O molecule is trapped within the host material without creating chemical bonds with Mo or S atoms. This is in line with our previous study of the electrolytically loaded crystals, where we proposed the same idea based on indirect indications in the data. Water physisorption may occur within grain boundaries, cracks and other volume defects. We recall, that a water molecule cannot penetrate the layered structure of MoS_2, which is obvious

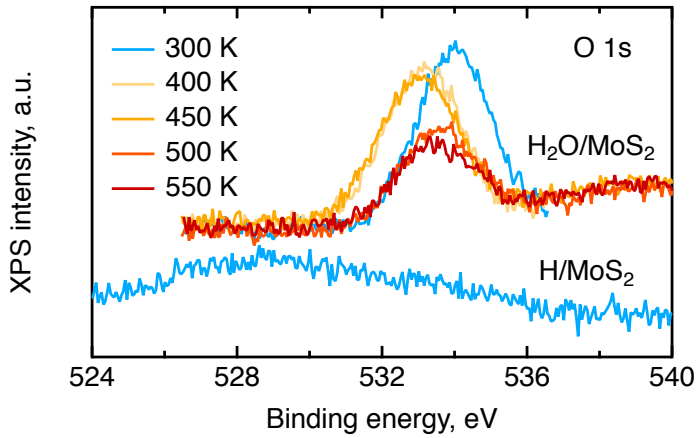

Fig. 4.6: XPS scans of the O 1s line for the water loaded H_2O/MoS_2 and hydrogen loaded H/MoS_2. A vertical offset is applied to the H/MoS_2 spectrum in order to simplify visual comparison, therefore the intensities should be regarded in terms of signal to noise ratio, and not in absolute values. The H_2O/MoS_2 was heated up to 550 K, with XPS scans performed at several intermediate temperatures, indicated in the legend. The displayed temperatures are the ones the sample was heated to and are slightly higher than the temperature during measurement.

given its large size, and additionally observed in an ageing NRA experiment, where, over time, the bulk hydrogen concentration does not rise above the background value, given by the clean, as received crystal. Therefore, our XPS study reveals that liquid water can access specific defective regions of MoS_2, where a larger number of active sites can be anticipated, which is important for an overall catalysis mechanism.

The evolution of the O 1s line profile between 450 and 500 K suggests, that the signal at 450 K consists of two peaks: one at 532.3 eV, from a species that desorbs at 500 K, and the other one at 533.4 eV, which stays unaffected at elevated temperatures. The two peaks may correspond either to water intercalated into defects of different type, or to oxygen bound within H_2O and within organic molecules, provided that the disappearing peak is yielded by water. The latter option would imply a loss of quasi-elastic neutron scattering signal at 500 K, which, as will be shown later in the discussion of the QENS results, does not occur. Therefore we conclude that there are several types of volume defects, which provide an appropriate environment for water physisorption within MoS_2 crystals. In these defects water is constrained with different binding energy, which results in non-identical desorption tem-

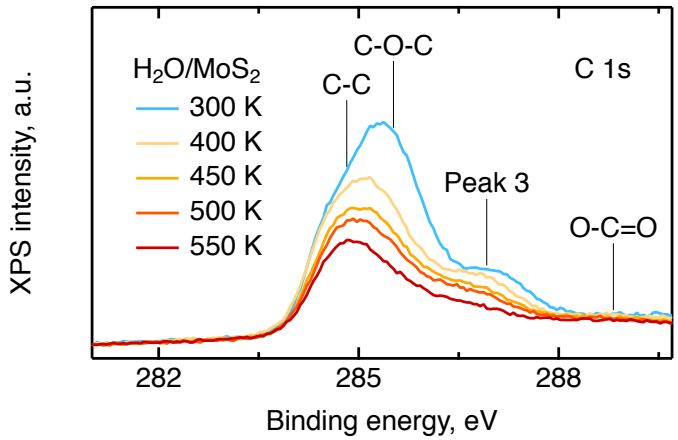

Fig. 4.7: XPS scans of the C 1s line for the water loaded H_2O/MoS_2 measured at various temperatures, labelled via different colours. The assignment of Peak 3 is ambiguous, and thus, not labelled here. The displayed temperatures are the ones the sample was heated to and are slightly higher than the temperature during measurement.

peratures, namely, around 500 K for one species, and somewhere above 550 K for the other.

Now we turn our attention to the XPS data of the H atom-beam loaded sample, H/MoS_2. We begin the description with the analysis of the oxygen and carbon lines. The O 1s peak is extremely broad and feeble (Fig. 4.6). It consists of several peaks, however, numerically it is not feasible to distinguish them due to weak signal. The oxygen line reaches its maximum at 529 eV, the energy region where oxygen in molybdenum oxides is expected to reside [104, 105], and then has its tail spreading until 536 eV, thus covering also the region, where physisorbed water is usually observed. The peak area in the latter region, is, however, much smaller than the one, observed for H_2O/MoS_2, and therefore the presence of water may be neglected. The carbon line does not show any extraordinary behaviour, and thus it was used only as a binding energy reference.

Before continuing, we would like to recall in brief the temperature treatment procedure: Each time after the specimen had been heated to an indicated temperature, the heater was turned off in order for the chamber pressure to descend to a value that allowed turning on the XPS spectrometer. During the resting time, which generally lasted around 30 minutes, the sample cooled down by several tens of degrees. The indicated temperature, thus, shows the

temperature the crystal was heated to, which is higher than the one during measurement. This process, however, is not expected to affect the surface chemistry significantly, and therefore the data is presumed to represent the surface state, achieved at an elevated temperature and frozen afterwards. In the following, we proceed with the description of the XPS data for sulphur and molybdenum. At room temperature the S 2p and Mo 3d lines are shifted slightly to higher binding energies, corresponding to an oxidized surface. Upon heating the surface gets reduced at 360 K (Fig. 4.8). The reduction is accompanied by a splitting of the S 2p peak. Upon heating further to 400 K both the sulphur and molybdenum lines reach the clean MoS_2 state. Next, at 420 K the reduction phenomenon occurs again, however, this time, without a detectable splitting. Here we note, that at this temperature a strong desorption peak was encountered, leading to a much longer pressure recovery time. During the corresponding long waiting period the sample cooled down to room temperature. The subsequent series of XPS measurements was carried out after 14 hours, and the initial scan was conducted at 300 K in order to review the surface chemistry variations over a longer period. The S 2p line appears to shift approximately halfway towards a clean state, and does not reach it. This supports our assumption that over a short time period the changes in surface chemistry are minor. When heating further to 450 and 500 K, the sample exhibits a similar pattern as observed at 360 K, with almost identical shift and peak splitting. Then, at 550 K, the surface returns to a clean state with slightly oxidized molybdenum.

Given the observation that the water loaded sample does not exhibit a similar behaviour in terms of S 2p line shift and splitting, we conclude that the effects observed for H/MoS_2 are caused by the incorporated hydrogen. The reduction phenomenon, thus, should be attributed to hydrogen atoms, creating chemical bonds with the MoS_2 surface. This requires a source of hydrogen atoms to be present somewhere in the subsurface region. One of the possible options is hydrogen atoms, incorporated into the bulk during the loading process, which migrate to the surface at elevated temperatures. The other possible source is H_2 molecules, which would be generated via recombination, given the known activity of MoS_2 in the hydrogen evolution reaction. H_2 may dissociate into H atoms on a heated MoS_2 matrix. On the other hand, considering the results of our neutron and molecular dynamics simulation studies, we will show that the samples loaded via atom beam bombardment do not contain large amounts of hydrogen molecules, therefore their possible contribution will not be discussed explicitly. If, nevertheless,

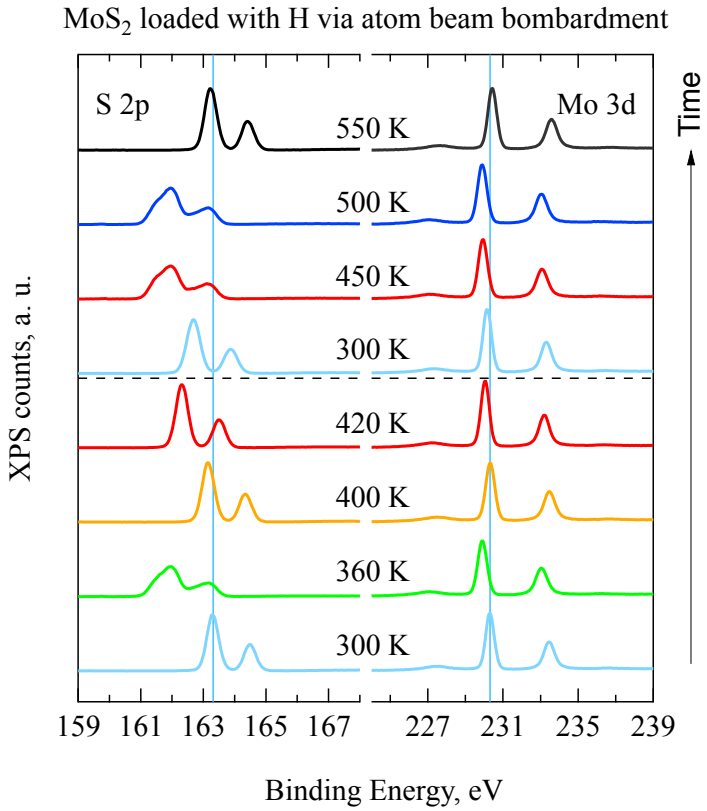

Fig. 4.8: X-ray photoelectron spectroscopy scans of the S 2p and Mo 3d elemental lines of H/MoS_2. The data were acquired at several temperatures from 300 to 550 K, which are indicated by different colours. For visual clarity vertical offset is applied to each spectrum. A blue upright line shows the position of the corresponding peak at room temperature. The "Time" axis represents the order in which the measurements were performed.

some recombined H_2 molecules are present in H/MoS_2, then their influence on the XPS spectrum will be indistinguishable from the H atoms in the -SH groups, given the similar hydrogen binding energies in these compounds [42, 121]. Taking into account only the available information from XPS, the interpretation of the XPS data is not unique. In this latter sense, we will only present one of the possible scenarios in terms of different hydrogen species in the following.

Hydrogen atoms can be stored in MoS_2 combined in -SH groups, as in a perfect crystal, or in a local potential minimum near defects, such as sulphur vacancies. The binding energy of hydrogen within these species is reported

to be around 0.6 eV for -SH groups and 1.3 eV for H atoms within a sulphur vacancy [42], respectively. Experimentally, we observe the first reduction sequence at 360 K, accompanied by a peak splitting. Given the said binding energies this process can be assigned to the initiation of hydrogen mobility from subsurface -SH groups, which deliver new hydrogen atoms to the surface. Molybdenum sulphide layers are assembled as S-Mo-S sandwich. Therefore, it is safe to assume that, within the uppermost layer, hydrogen uptake in the outer S sub-layer is different from the one in the inner S sub-layer, where the former faces vacuum and the latter - another S sub-layer. This results in different reduction levels for two subsequent S sub-layers, and hence, peak splitting. Further, at 400 K all of the surface hydrogen is desorbed, resulting in a clean surface. At 420 K hydrogen atoms constrained within sulphur vacancies start to move, providing hydrogen to the surface, thus, reducing it. This reduction process becomes more pronounced at 450 K and continues up to at least 500 K, vanishing at 550 K. The fact that, in this case, total desorption requires higher temperatures or longer times, suggests that the amount of hydrogen stored within sulphur vacancies is much greater, than in the form of -SH groups. Here we recall, that the presented interpretation is only tentative. More experimental and calculated data are required to make a firm statement.

4.3.2 Neutron time-of-flight spectroscopy - hydrogen dynamics

We now turn to the presentation of the results of the quasi-elastic neutron scattering experiments. In QENS the measured entity is the mobility of the sample atoms through scattering of a monochromatic beam of neutrons. Upon scattering the mobile sample atoms exchange kinetic energy with the neutrons, which leads to a broadening of the energy distribution around the elastic scattering peak. In our experiments the large majority of this quasi-elastic signal will stem from hydrogen, because hydrogen has a substantially bigger neutron scattering cross section than all other atoms and we do not expect any significant diffusion from molybdenum or sulphur, the substrate atoms.

As before, we commence our analysis with the water loaded H_2O/MoS_2 and then continue with the H atom-beam loaded H/MoS_2. Taking a first look at the data (Fig. 4.9), one can observe that the quasi-elastic signal

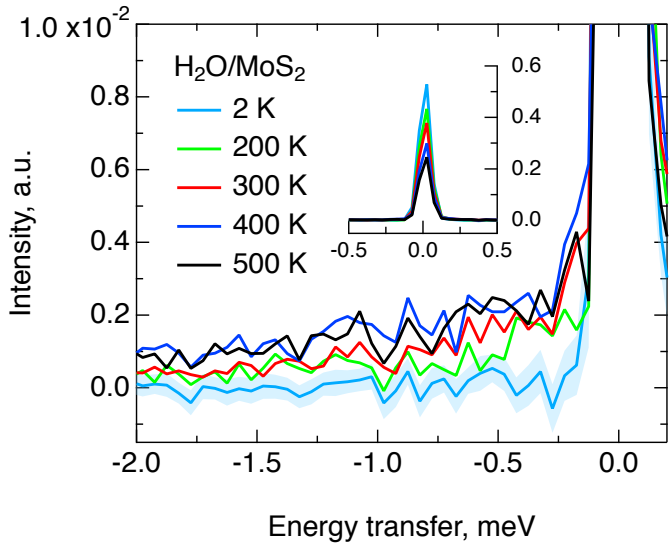

Fig. 4.9: Quasi-elastic neutron scattering spectra of water loaded H_2O/MoS_2, obtained at momentum transfer $Q = 1.55$ Å^{-1} and at various temperatures, which are indicated via colouring. The plot is scaled to display the QENS broadening. For visual clarity the error bars are omitted for each spectrum except the 2 K one, for which they are expressed as shadowing. The inset displays the same spectra in full scale at Y axis.

for H_2O/MoS_2 appears already at 200 K, meaning that at this temperature hydrogen atoms start moving fast enough to enter the spectroscopic window of the instrument. At 300 K the QENS intensity increases substantially and it stays at a similar level beyond this temperature. Since even at 500 K the quasi-elastic signal remains rather feeble, it was decided to fit the data with a commonly used model consisting of a sum of an elastic line and one Lorentzian, describing the quasi-elastic broadening:

$$S(Q,\omega) = A_{el}(Q)S_{res}(Q,\omega) + A_{qe}(Q)L(\Gamma(Q),\omega) * S_{res}(Q,\omega) + B, \quad (4.1)$$

where $A_{el}(Q)$ and $A_{qe}(Q)$ are intensities of elastic and quasi-elastic scattering, respectively, $S_{res}(Q,\omega)$ is the instrument resolution function, i.e., the spectra obtained at 2 K where no detectable atomic motion is anticipated, $L(\Gamma(Q),\omega) = \frac{1}{\pi}\frac{\Gamma(Q)}{\omega^2+\Gamma(Q)^2}$ is a normalized Lorentzian function with a half-width-at-half-maximum (HWHM), $\Gamma(Q)$, B is a constant background term and $*$ represents a convolution action. Apparently, one Lorentzian is sufficient to describe the data of H_2O/MoS_2 (Fig. 4.10), and the introduction of

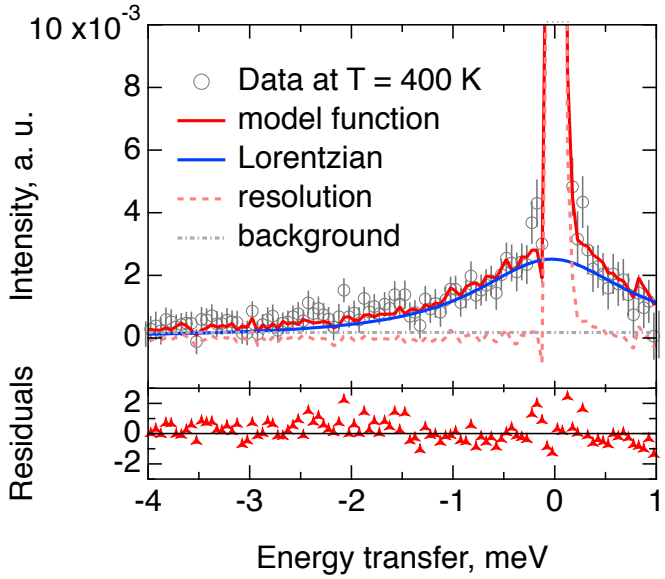

Fig. 4.10: The fit of the QENS data for H_2O/MoS_2 at 400 K and Q = 1.35 Å^{-1}, obtained with the model described in the main text (Eq. 4.1). The data points are displayed as grey circles, the model function is a red line consisting of a Lorentzian (blue line), elastic line (pale red dashed line) and background (grey dash-dotted line). The residuals function is plotted on the bottom of the graph. It represents the difference between the model function and the data, weighted for statistical errors. The elastic line is not fully shown in the plot, however, the quality of the fit around $\hbar\omega = 0$ can be assessed visually via the residuals function.

a second Lorentzian does not significantly improve the fit results in terms of χ^2 statistics. Therefore, we may conclude that only one diffusion mode is observed for H_2O/MoS_2.

By looking at the total scattering intensity $A_{total}(Q) = A_{el}(Q) + A_{qe}(Q)$ (Fig. 4.11), it becomes evident that some signal is lost when heating the sample. Also, we note small peaks around 1.5 and 1.9 Å^{-1}, which could be caused by various compounds possibly existing in the system, however, the determination of an exact source is not important for the current study. For the interpretation of the total scattering intensity behaviour the peaks do not play a major role, but further in the analysis of the elastic incoherent structure factor, their effect will be significant and easily observable. $A_{total}(Q)$ can be expressed as a product of a Q-independent constituent $K(T)$, which represents the amount of hydrogen in the sample and, hence, depends on temperature, and the Debye-Waller factor:

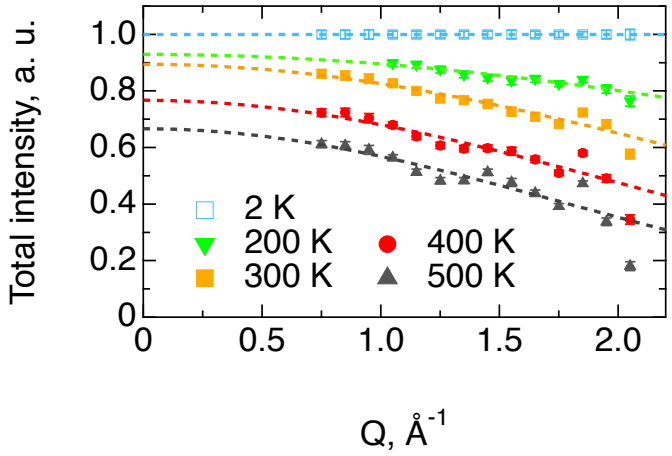

Fig. 4.11: Total neutron scattering intensity (elastic plus inelastic) for H_2O/MoS_2. Data were collected at increasing temperature from 2 to 500 K. The temperature is indicated via colouring and markers according to the legend. Experimental points are modelled with the scaled Debye-Waller law (Eq. 4.2), and the fit curves are displayed as dashed lines of corresponding colour.

$$A_{total}(Q) = K \cdot \exp(-Q^2\langle u^2\rangle/3), \tag{4.2}$$

where $\langle u^2\rangle$ stands for the mean square displacement of H atoms. During heating some hydrogen could desorb and leave the system, thus decreasing the $K(T)$ coefficient, which is normalized to be equal to unity at 2 K. By fitting the data to Eq. 4.2 it is possible to estimate $K(T)$, which appears to gradually decrease with rising temperature (Fig. 4.11), decaying from 0.93 at 200 K to 0.67 at 500 K. Thus, even at the highest scanned temperature the amount of water in the sample remains to be significant. A similar situation is observed in the XPS experiment, where the oxygen line remains strong at 550 K.

Now we proceed to the analysis of an eventual spatial confinement of water molecules. The corresponding information is contained in the elastic incoherent structure factor, $A_0(Q)$ [60]:

$$A_0(Q) = \frac{A_{el}(Q)}{A_{el}(Q) + A_{qe}(Q)}. \tag{4.3}$$

Clearly the EISF decays with Q (Fig. 4.12), indicating some level of spatial

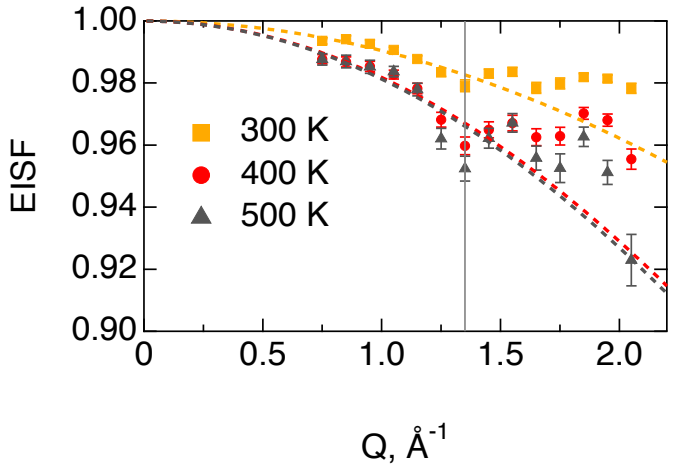

Fig. 4.12: Elastic Incoherent Structure Factor for hydrogen in H_2O/MoS_2. The EISF was extracted at three temperature points, indicated in the legend with corresponding colours and markers. Experimental values were approximated by means of the model for confinement within a sphere (Eq. 4.4), and the fit curves are displayed as dashed lines of corresponding colour. Data points to the left of the vertical line were used for the quantitative fit, while the points to the right are significantly influenced by elastic peaks and not used for the fits. The error bars at 300 K are smaller than the markers.

confinement. However,, due to the already mentioned broad elastic peaks, the data beyond Q = 1.4 Å^{-1} are unsuitable for a quantitative analysis of the EISF. Nevertheless, an attempt was made to fit the whole range, which did not lead to qualitatively different results which would affect the interpretation that is given below. The Q region up to 1.4 Å allows only to estimate the size of the confining volume, but provides no conclusive information on its shape. Therefore for a quantitative analysis a basic model of a confinement within an impermeable sphere of a radius R_c was used [61]:

$$A_0(Q) = A_0(0) \cdot \left(\frac{3j_1(QR_c)}{QR_c} \right)^2, \tag{4.4}$$

where $j_1(QR_c)$ is a spherical Bessel function of the first kind and first order and the factor $A_0(0)$ accounts for the fraction of hydrogen that is constrained. The chosen model describes the data well, but the fits of the data yield an unexpectedly small radius of confinement, $R_c = (0.30 \pm 0.01)$ Å at elevated temperatures and an even smaller radius, $R_c = (0.20 \pm 0.01)$ Å, at 300 K.

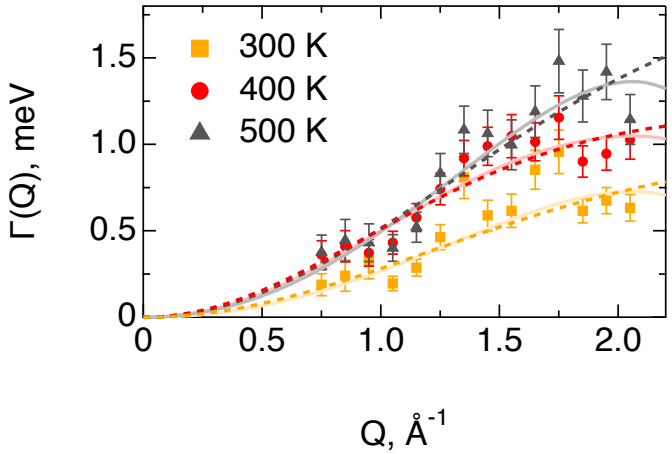

Fig. 4.13: The width of the QENS broadening for H_2O/MoS_2, estimated at three temperature points and displayed as coloured markers according to the legend. The fits by means of the Hall-Ross model are shown as dashed lines, and by the Chudley-Elliot model as straight pale lines. The latter model is unstable since no data are available beyond the apex after which bending downwards occurs.

These values could be influenced by a presence of immobile hydrogen within the sample. Here, we use the notion "immobile" to refer to hydrogen atoms that are moving too slowly to yield a QENS broadening within the resolution window of the spectrometer. The XPS experiment revealed that water is constrained within different local MoS_2 environments, having variable binding energies there. This suggests that the diffusion rate of H atoms may also vary from one local environment to another. Very slow hydrogen, thus, contributes to the elastic line, increasing the EISF and decreasing the observed apparent confining radius. Nevertheless, the R_c remains much smaller than the gyration radius of H in a water molecule. This means that the detected motion should not be attributed to a full revolution of hydrogen around an oxygen atom. To acquire a better insight into which kind of hydrogen diffusion is observed, the analysis of the Lorentzian line width is required.

Apart from a full revolution, hydrogen atoms may also perform rotational motion around, for instance, an axis which is parallel to the line connecting two H atoms in H_2O, and which passes through the O atom. In this case the Lorentzian width, $\Gamma(Q)$, should be constant over the scanned momentum transfer region. However, the experimental values clearly show the presence

of translational diffusion with a jump-like behaviour, which is indicated by a rise of $\Gamma(Q)$ at low Q, and its saturation above 1.7 Å^{-1} (Fig. 4.13). Jump diffusion in a liquid is usually treated in terms of the Singwi-Sjölander (SS) model [110], which assumes an exponentially decaying distribution of jump lengths:

$$\rho(r) = r/r_0^2 \cdot \exp(-r/r_0). \tag{4.5}$$

Along with the SS model we have also tested the Hall-Ross [58] (HR) and Chudley-Elliot [57] (CE) models on our set of data. The former utilizes a normal distribution of jump distances

$$\rho(r) = \frac{2r^2}{r_0^3\sqrt{2\pi}} \exp(-r^2/2r_0^2) \tag{4.6}$$

and the latter assumes diffusion over a discrete array of jump sites of a Bravais lattice. The explicit formulae for the Lorentzian widths in these models are:

$$\Gamma_{SS}(Q) = \frac{\hbar D_{SS} Q^2}{1 + \tau_{SS} D_{SS} Q^2},$$
$$\Gamma_{HR}(Q) = \frac{\hbar}{\tau_{HR}} \cdot [1 - e^{-\tau_{HR} D_{HR} Q^2}],$$
$$\Gamma_{CE}(Q) = \frac{3\hbar}{4\tau_{CE}}[1 - J_0(Q_\parallel l)], \tag{4.7}$$

where D is the diffusion coefficient, τ is the residence time between jumps, l is the distance between jump sites, $\hbar$ is the reduced Planck's constant and $J_0(Q_\parallel l)$ is the Bessel function of the first kind and order zero with $Q_\parallel = Q \cdot \sin(\phi + \arcsin(Q\lambda/4\pi))$ being the projection of the $\boldsymbol{Q}$ vector on the MoS_2 basal plane. Here, we used a representation of the CE model developed for a 2D hexagonal array of jump sites, given in the section 2.2.1, which satisfies the structure of MoS_2. However, given the statistical errors of the data, the exact pattern of the jump site distribution is not significant. All three models produce a satisfactory description of the data. Unfortunately, the fits of the CE model became unstable and yielded large errors in the fit parameters due to a lack of data points beyond 2 Å^{-1}, which are important in order to access the sine-like features of the CE model. Therefore only the SS and HR models will be discussed further. Their results are summarized in Table 4.1. The diffusion coefficient increases when the sample is heated from room temperature to 400 K. At 500 K it does not increase further within the experimental error bars.

Table 4.1: The results of the analysis of QENS broadening for H_2O/MoS_2 by means of the Singwi-Sjölander and Hall-Ross model. The average jump distance is $d = \sqrt{\langle l^2 \rangle}$, the residence time between jumps is τ_{res} and the diffusion coefficient is D.

T, K	$\sqrt{\langle l^2 \rangle}$, Å	τ_{res}, ps	D, $10^{-8} \cdot m^2/s$
Singwi-Sjölander			
300	1.1 ± 0.2	0.4 ± 0.1	0.5 ± 0.1
400	1.6 ± 0.2	0.4 ± 0.1	1.1 ± 0.2
500	1.1 ± 0.2	0.2 ± 0.1	0.9 ± 0.1
Hall-Ross			
300	1.4 ± 0.2	0.7 ± 0.1	0.5 ± 0.1
400	1.8 ± 0.2	0.6 ± 0.1	1.1 ± 0.2
500	1.4 ± 0.2	0.3 ± 0.1	0.9 ± 0.1

Given the above results we propose two possible scenarios for the translational diffusion of hydrogen in H_2O/MoS_2. As already noted, water molecules should be adsorbed in small voids or cracks in the material. The first option is diffusion of H_2O molecules as a whole around a defect domain which provides a small enough binding energy of water molecules inside of it. Provided the domain hosts several H_2O molecules, they may collide with each other performing a motion, which is generally described via liquid diffusion models, such as SS and HR. The other option is a clustering of water molecules and subsequent hopping of hydrogen atoms from one oxygen to another, or to sulphur and back.

Now we turn to the H atom beam loaded H/MoS_2. Here, the 200 K spectra showed no observable quasi-elastic broadening, and hence they were used as resolution function. During the initial heating run the quasi-elastic signal rose significantly at 300 K and continued increasing up to 400 K (Fig. 4.14). Further, at 500 K, the QENS signal vanished, returning to the spectrum observed at 200 K. This indicates a loss of almost all the hydrogen that was mobile at 400 K. Since the sample holder was open to the cryo-furnace environment, the desorbed hydrogen was not expected to be reabsorbed when cooling down. This is exactly what was observed during the second heating sequence: the absence of any significant QENS signal. Therefore, the second run was used as a measure of the host scattering, which includes immobile hydrogen species and a small contribution from MoS_2. The second heating run spectra, thus, were subtracted from the corresponding first heating run data in order to minimize the influence of the scatterers not under study.

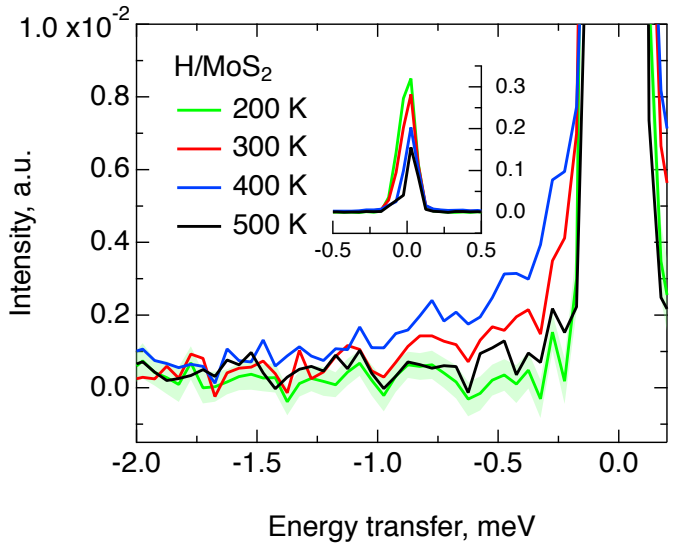

Fig. 4.14: The quasi-elastic neutron scattering spectra of hydrogen loaded H/MoS_2, obtained at momentum transfer $Q = 1.85$ Å^{-1} and at various temperatures, which are indicated via colouring. The plot is scaled to display the QENS broadening. For visual clarity the error bars are omitted for each spectrum except the 200 K one, for which they are expressed as shadowing. The inset displays the same spectra in full scale at Y axis.

Total desorption of mobile hydrogen at 500 K is a notable feature of H/MoS_2 samples, which distinguishes them from the electrolytically and water loaded crystals, and additionally supports our interpretation of the hydrogen species present in each sample.

To describe the corrected data Eq. 4.1 was used with $S_{res}(Q,\omega)$ being the corresponding 200 K spectrum. The QENS signal both at 300 and 400 K is rather weak. Therefore, only the high Q data, above 1.35 Å−1, could be exploited for a quantitative analysis. Clearly, one Lorentzian model is sufficient to fit the profile of the experimental spectra (Fig. 4.15), and no additional peak is required. This is different from what was observed previously for the MoS_2 crystals that were electrolytically loaded with hydrogen, where two diffusion modes were detected. The total scattering intensity, $A_{total}(Q)$, was fitted to the already mentioned scaled Debye-Waller law (Eq. 4.2). The extrapolation of $A_{total}(Q)$ to $Q = 0$ Å^{-1} reveals that at room temperature the overall amount of hydrogen is almost the same as at 200 K (Fig. 4.16). The desorption starts when heating the sample to 400 K, which leads to a drop in the amount of hydrogen by 26 %. Further heating to 500 K results

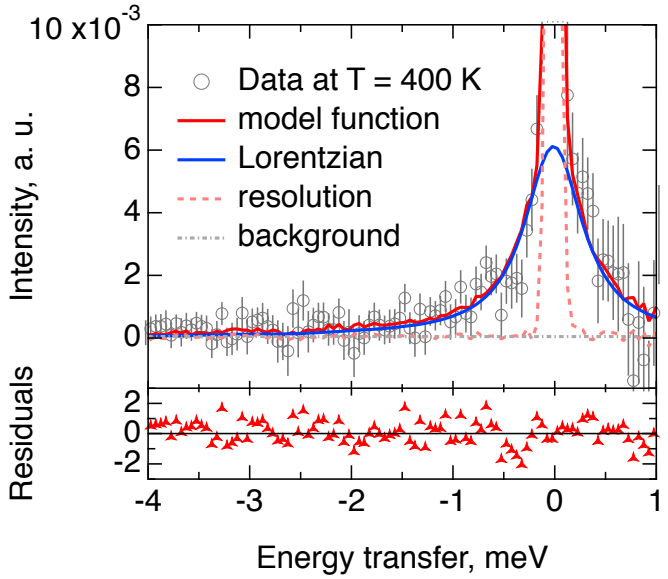

Fig. 4.15: The fit of the QENS data for H/MoS_2 at 400 K and Q = 1.85 Å^{-1}, obtained by means of Eq. 4.1. The data points are displayed as grey circles, the model function is a red line consisting of a Lorentzian (blue line), elastic line (pale red dashed line) and background (grey dash-dotted line). Also in the bottom of the graph the residuals function is plotted, which stands for a difference between the model function and the data, weighted for statistical errors. The elastic line is not fully represented in the plot, however, the quality of the fit around $\hbar\omega = 0$ can be accessed visually via the residuals function.

in total loss of mobile hydrogen. In the XPS experiment we observed hydrogen desorption at a somewhat higher temperature, 550 K. This difference is caused by a shorter period between the scans in XPS than in the neutron measurement, i.e., in the X-ray experiment hydrogen did not have enough time to fully desorb below 550 K.

Next we examine the effect of hydrogen confinement in H/MoS_2. We recall that the data were collected for the in-plane geometry, which means that the diffusion parallel to the MoS_2 basal planes is studied. The EISF appears to be constant within the error bars both at 300 and 400 K, meaning that no spatial restrictions for hydrogen diffusion are observed (Fig. 4.16). However, the value of the extrapolation to $Q = 0$ Å^{-1} changes under temperature treatment, decaying from 0.83 at 300 K to 0.45 at 400 K. This value represents the ratio of immobile hydrogen to the total amount of hydrogen in the sample. It is evident that at 300 K only a small fraction of H atoms perform movement fast enough to be detected in the experiment. Further, at

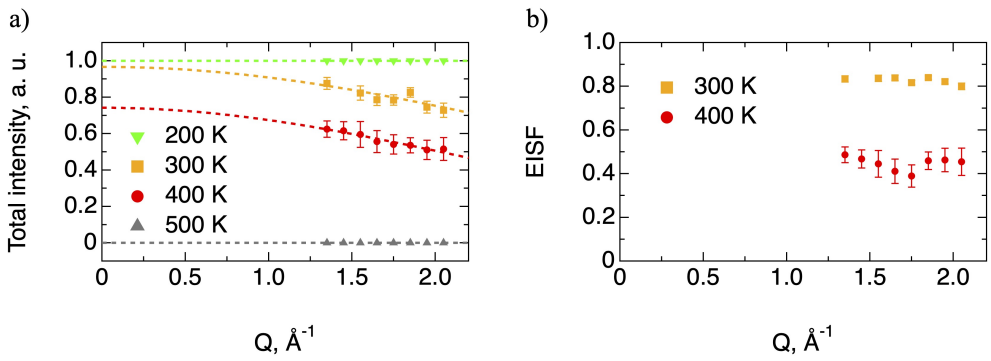

Fig. 4.16: a) Total neutron scattering intensity and b) EISF for H/MoS_2. Data were collected at increasing temperature from 200 to 500 K, which are indicated via colouring and markers according to the legend. The total intensity factor is modelled with the scaled Debye-Waller law (Eq. 4.2), and the fit curves are displayed as dashed lines of corresponding colour. The error bars of the EISF at 300 K are smaller than the markers.

400 K more hydrogen centres get activated and around a half of the H atoms become mobile. The total hydrogen mobilization is anticipated somewhere between 400 and 500 K, since at the latter temperature any QENS signal is lost. We note, taking into account the reduction procedure, that this does not forbid the presence of any hydrogen species, which remain immobile even at 500 K. From NRA it is deduced that some amount of immobile hydrogen is present up to 700 K.

For the estimation of Lorentzian widths, in order to obtain more data points, an alternative fitting approach was used. Data at high Q were fitted as described previously in the text, while spectra at low Q were fitted with the same equation, but with the Lorentzian area fixed. Since in this range all the intensity parameters vary only slightly, the approximation must yield the quasi-elastic broadening close to the correct one. Nevertheless, in Fig. 4.17 the two ranges are depicted explicitly to stress the different fitting procedures. The width of the QENS broadening, $\Gamma(Q)$, increases with Q and does not reach a plateau within the available Q region, which is a common feature for a continuous Brownian diffusion [32] (Fig. 4.17). Such behaviour, of course, can also be described by means of jump diffusion models with a continuous distribution of jump lengths, like the Singwi-Sjölander model. However, this leads to overparametrisation, and therefore, in this case, jump-diffusion models become less trustworthy. On that accord we will continue the interpretation in terms of Brownian motion. Interestingly, the

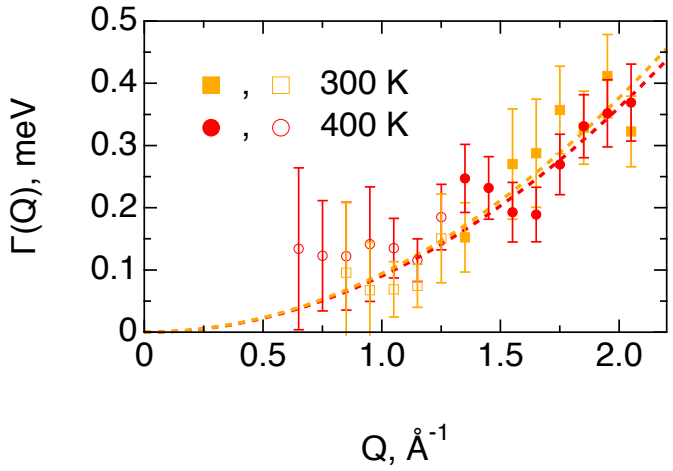

Fig. 4.17: The width of the QENS broadening for H/MoS_2, extracted at two temperature points and displayed as coloured markers according to the legend. The full markers indicate that the points were obtained via the default model given by Eq. 4.1, while for the points with hollow markers the intensity of the Lorentzian was fixed. The fits by means of the DQ^2 model for Brownian diffusion are shown as dashed lines.

diffusion coefficient, D, at 300 and 400 K is mostly the same, amounting to $1 \cdot 10^{-9} m^2/s$, approximately. This means that the activation barrier for the diffusion must be low. Unfortunately, with only two temperature points available for the analysis it is not feasible to present an unambiguous interpretation. The statistical errors in our data points are not sufficiently small to rule out the possibility of a moderate dependency of D on the temperature. In any case, the atomic hydrogen motion appears to be slower in MoS_2, than on the surface of Pt [111].

4.3.3 Molecular dynamics simulations

Classical molecular dynamics simulations were performed for two configurations of hydrogen: on the surface of MoS_2 and in its bulk. We simulated four hydrogen species, namely, neutral H atoms, positively charged H^+ ions, H_2 molecules and water molecules. The comparison of the simulations of H and H^+ allows us to assess the influence of hydrogen charge on its diffusion pattern, which is important in view of a possible electron exchange with the MoS_2 matrix. The main aim of the simulations was to obtain a qualitative

insight into the classically possible pathways for hydrogen diffusion. Our calculations are not assumed to give a good quantitative fit of parameters, such as desorption temperatures, diffusion coefficients, etc., since, for simplicity of simulations, we neglect chemical bonds, which, especially for H atoms or ions, must affect the values of said parameters.

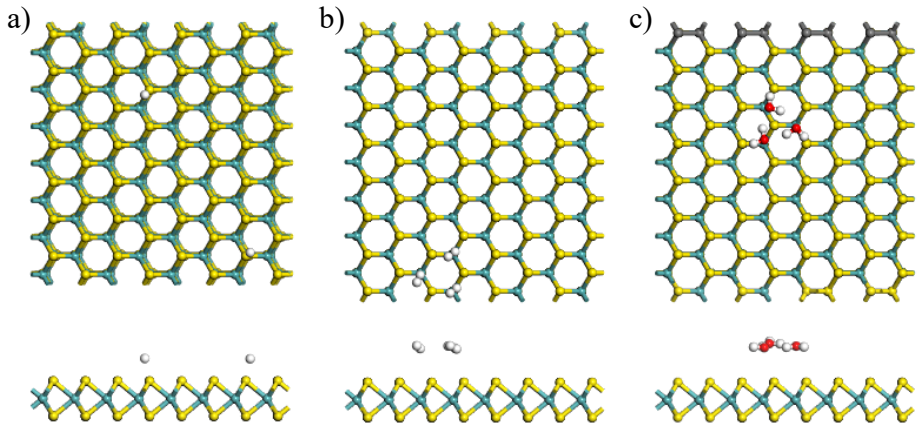

Fig. 4.18: The hydrogen locations on the surface at 3 K. a, b, and c show top views (top) and side views (bottom) of the surface for H^+, H_2 and H_2O, respectively. Atoms are coloured according to the elements: Mo is cyan, S is yellow, H is white, and O is red.

We begin the description with the results for hydrogen diffusion on the surface of MoS_2 (see Fig. 4.18 and Fig. 4.19). When neutral hydrogen atoms are placed on the surface, they desorb already at the lowest simulated temperature of 3 K, signalling that the electron exchange with MoS_2 must play a role in neutral H adsorption. H^+ ions, on the contrary, are attracted to S atoms via Coulomb forces and stay on the surface until the temperature rises to 200 K. Between 100 and 200 K hydrogen ions occasionally hop from one sulphur atom to another, with a frequency that increases with temperature. This type of diffusion would probably be difficult to observe experimentally, since at low temperatures the diffusion is very slow, and the increase in temperature is directly connected to the strength of H desorption. H_2, similar to neutral atoms, are barely attracted to the MoS_2 surface and leave it at 100 K. Water molecules, on the contrary, position themselves on top of Mo atoms and stay on the surface almost up to 500 K. The desorption temperature can be increased even higher by creating a sulphur vacancy and placing an H_2O molecule in its vicinity. Hence, although the desorption temperatures in the simulations may not be the same as in the experiment, the general trend of

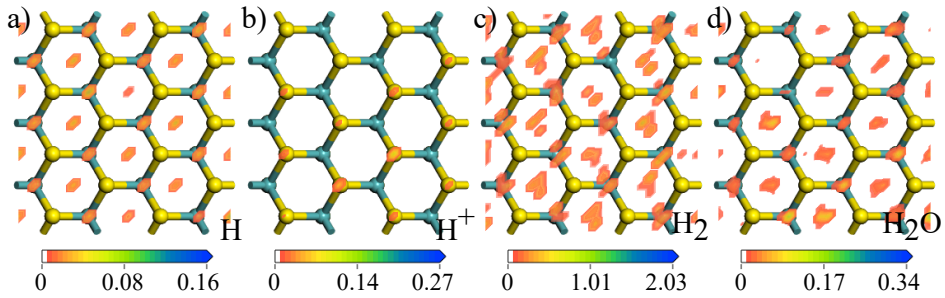

Fig. 4.19: Top views of the results from adsorption dynamics calculations, which show preferred sites for hydrogen. The colour shows the density of hydrogen on the surface. The inhomogeneity of the hydrogen density is caused by the limited sampling statistics of the adsorption calculations.

a higher desorption barrier for water on MoS_2, than for H^+ ions, is observed both in the experiment and the simulations.

The possibility to penetrate the layers of MoS_2 was calculated for H, H^+ and H_2 (Fig. 4.20). It was not calculated for H_2O since it is obvious that water molecules, due to their size, cannot pass through a defect-free layer. The calculation was carried out manually by placing the atom or molecule at initial position and subsequently shifting it towards the destination, and calculating its energy at several intermediate points. The resulting energy barrier is much higher for the ions, than for neutral atoms, where it is approximately 4 eV for the former and 0.4 eV for the latter. Apparently, the difference is caused by the Coulomb repulsion by the Mo atoms. This information suggests, that the bombardment of MoS_2 with neutral H atoms can relatively easily deliver them a few layers deep into the material, allowing also for their thermalisation with the hot filament. Then, after loosing kinetic energy, protiums bind to sulphur, and layer penetration becomes hindered. The diffusion barrier for migration parallel to the MoS_2 layers from one hexagonal site to another is at a similar level for both H and H^+, below 0.15 eV, which is significantly lower than the one for layer penetration. H_2 diffusion is hindered in both directions, with a very high 20 eV barrier for relocation from one interlayer space to another, even with the H_2 molecule aligned perpendicular to the layers (Fig. 4.20). Jumps between hexagonal sites are also improbable and depend on the orientation of the molecule, although the barrier is much lower, 2 eV. Hence any recombined H_2 is not expected to leave the crystal easily.

The diffusion of H and H^+ in the bulk of MoS_2 exhibits a jump-like

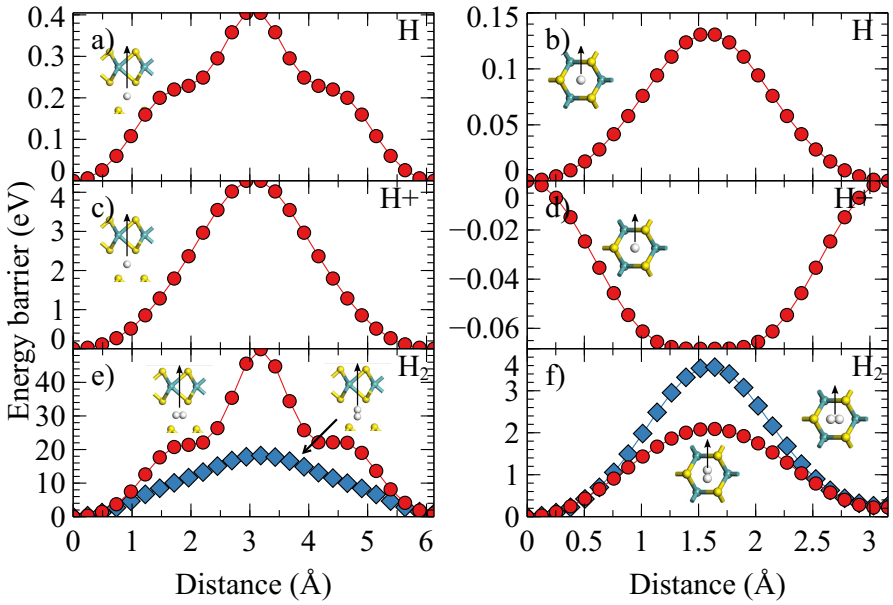

Fig. 4.20: Diffusion barriers for H, H^+, H_2. a, c, and e are the barriers when crossing the S–Mo–S layer through a hole. b, d, and f are the barriers when hydrogen moves parallel to the layers in the space between layers from a hexagonal site to another. For H_2 the red and blue lines depict different orientations of the molecule. In e the red curve represents H_2 molecule aligned parallel to the MoS_2 layers, while the blue curve shows the results for the molecule aligned perpendicular to the layers, along the hole. In f red line represents H_2 molecule aligned along its move direction, while for blue line the molecule was rotated 90° in-plane.

behaviour, however, the jump site geometries are different (Fig. 4.21 and Fig. 4.22). Neutral atoms favour staying between 6 sulphur atoms of two adjacent layers, while ions are mostly located at a line connecting two nearest S atoms from adjacent layers. We will call the former hexagonal site, and the latter bridge site. The hopping usually occurs as a series of two or three consecutive jumps and is heavily correlated with the shearing of MoS_2 layers. The diffusion coefficient, D, was estimated on the basis of fitting the QENS spectra, calculated from the simulated hydrogen trajectories. Despite the fact, that the layer penetration barrier is smaller for neutral atoms than for ions, the diffusion coefficient for the motion between layers shows the opposite behaviour. For H the obtained D rises from 3.5 to $7.5 \cdot 10^{-8}\ m^2/s$ at 300 and 500 K, respectively, while for H^+ it first leaps up from 2.2 to $21.3 \cdot 10^{-8}\ m^2/s$ between 300 and 400 K, and then decays to $10.3 \cdot 10^{-8}\ m^2/s$

at 500 K. This behaviour is directly connected to the shearing of MoS_2 layers. A protium, being added to the matrix, does not disturb the structure significantly and the mean square displacement of sulphur atoms remains close to its value for a clean MoS_2. A positive proton, on the other hand, destabilizes the matrix completely, inducing large displacement of S atoms, which at 500 K result in the formation of a new stable structure with $P\bar{6}m2$ space group. Such instability drives hydrogen movement and causes a large diffusion coefficient for H^+ at 400 K. The decrease of D at 500 K is the result of a more stable structure. We note, that in a real crystal a disorder of this kind is less likely to occur since a substantial amount of hydrogen is only present up to ∼100 nm below the surface, beyond this depth there is a stable, hydrogen-free molybdenum sulphide. Therefore, the small value and the absence of considerable temperature dependence of the experimentally observed diffusion coefficient may be connected to the rigidity of the host matrix.

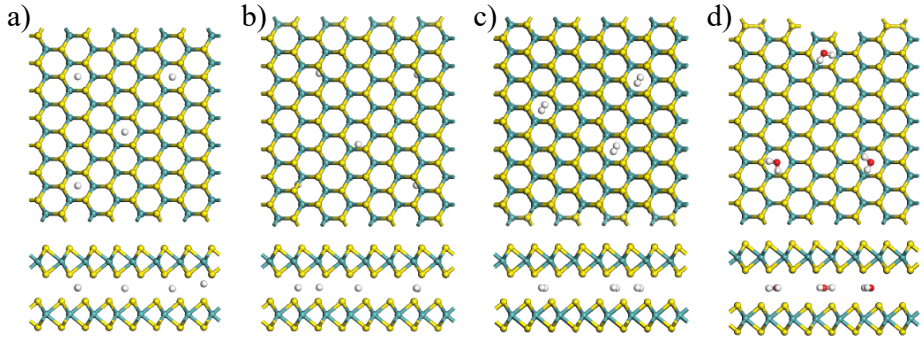

Fig. 4.21: The hydrogen which is inside the bulk MoS_2 at 3 K. a, b, c, and d show top views (top) and side views (bottom) of the model for H, H^+, H_2, and H_2O respectively.

Water molecules in the bulk of MoS_2 stay in hexagonal interlayer sites with the oxygen atom pinned in the centre and almost immobile (Fig. 4.21). The water hydrogen atoms perform random reorientations around the oxygen atom. The main mode is 2D rotations in plane, parallel to MoS_2 layers (c rotational axis). As the temperature rises, out-of-plane swings intensify and occasionally full revolutions around the a rotational axis happen. The simulated QENS broadening is constant versus Q and amounts to 4 meV already at 100 K, rising with temperature. Therefore it is not surprising that in the experiment no rotational diffusion is detected, since such width would result in a Lorentzian broadening that is large enough to be interpreted

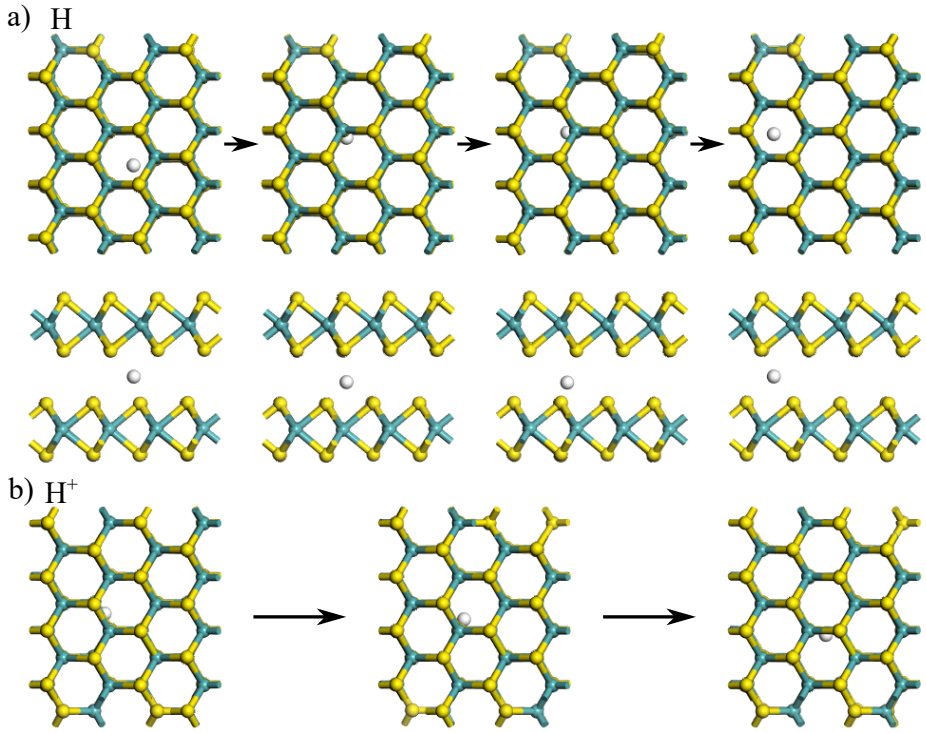

Fig. 4.22: This sequence of images shows the jumps of a) H and b) H^+ in the bulk of MoS_2.

as constant background, i.e., it is too fast for the spectroscopic window of our neutron spectroscopy experiments[1]. The translational diffusion observed in the TOF study, thus, cannot be yielded by water molecules constrained in a perfect crystal and must be caused by H_2O accumulated within structural defects, the exact configuration of which is still under question.

In a similar manner H_2 molecules are trapped in the centres of hexagonal interlayer sites. However, their motion is restricted from performing a full revolution around the molecule's centre of mass. Instead, the molecule undergoes random jump-like reorientations mostly parallel to the MoS_2 layers. The displayed quasi-elastic broadening is constant versus Q and increases from 0.2 to 2 meV from 100 to 500 K, respectively. These values lie nicely within the spectroscopic window of the exploited neutron spectrometer, therefore, such diffusion must be observable in our studies. The rotational diffusion mode de-

[1]The neutron transfer energy range, required to observe such rotational diffusion can be accessed by, for example, PANTHER instrument at the ILL.

tected for the electrolytically loaded crystals exhibits the characteristic time of rotations approximately one magnitude slower than the simulated values. The discrepancy could be attributed to electron cloud interactions between H_2 molecule and MoS_2, which was not accounted for in the simulations.

Following the same interpretation as for H_2O, the translational diffusion observed in the case of electrolytically loaded MoS_2 crystals must have been exhibited by H_2 molecules trapped in some specific environments. Experimentally we observed, that the short-range motion of a hydrogen molecule is isotropic (TOF) and the long-range motion occurs mostly in-plane with the MoS_2 layers (NSE). Therefore, the geometry of the space where H_2 diffusion takes place must be 2D. This could be the interlayer agglomeration of vacancies near stacking fault defects, or different types of grain boundaries. In this case the rotational diffusion can be expected to be faster, than it is estimated in our MD study, where the molecules are caged between S atoms. Therefore, the motion mode observed for electrolytically loaded crystals, that was interpreted as rotational mode, could not be exhibited by the same molecules, which were preforming translational diffusion. The width of this mode is close to the one observed for H/MoS_2, however, the Q dependence is clearly different. Hence, the most probable scenario is that the electrolytically loaded crystals contained recombined H_2 molecules both within various voids, where they move relatively freely, and trapped between S atoms in hexagonal sites, where they are restricted to perform any motion apart from reorientations. We note, however, that with the available information it is not possible to completely exclude the option of slower mode being exhibited by hydrogen atoms.

4.4 Conclusions

In summary, in this work the adsorption behaviour and motion of water and atomic hydrogen in MoS_2 has been studied.

Exposed to liquid water MoS_2 crystals tend to absorb a substantial amount of H_2O molecules, which are partially restrained within the host matrix up to the highest temperatures of our experiments, 500 K. The synoptical consideration of all methods points to physisorption in voids or cracks of the material and we find that there is no intercalation between perfect MoS_2 bilayers. The possibility of mobile electrolyte accessing inner surfaces of the crystalline material may be important for the electrocatalytic performance

of MoS_2. The motion of H_2O molecules is qualitatively similar to diffusion in liquid water: either it is dominated by movement of intact molecules in the volume of the void, or by hopping of protons between oxygen and sulphur similar to proton conduction in bulk water. The high diffusion rate may be caused by repulsion of water molecules by MoS_2, which could be expected due to the known hydrophobic properties of molybdenum disulphide.

The X-ray photoelectron spectroscopy reveals that under temperature treatment the surface of the H atoms loaded MoS_2 crystal undergoes a series of reduction-oxidation instances. This effect is due to hydrogen migration and is mainly observed for sulphur atoms. The reduction is attributed to the formation of S-H groups by attachment of hydrogen to the surface. Surface reduction is followed by re-oxidation under hydrogen desorption, as expected for recombinative desorption of H_2. Within the studied range of temperatures two reduction-oxidation cycles were observed. The first one between 360 and 400 K, which was assigned, based on the bond strength, to the mobilization of hydrogen within subsurface S-H groups, along with dissociation of the possibly generated H_2 molecules. The second cycle occurring between 420 and 550 K was assigned to hydrogen atoms bound within S vacancies or other defective sites which provide a similar hydrogen binding energy. During the first cycle these atoms did not have enough energy to leave their traps and were, in terms of the time-scale of our study, immobile. The number of H atoms activated during the second cycle was found to be greater, than the one for the first cycle, as indicated by the temperature range span of the reduction process. Additional nuclear reaction analysis measurements assume that some amount of immobile hydrogen is present up to 700 K.

As far as hydrogen diffusion is concerned, we find that in the present study for the H/MoS_2 the mobile species is clearly $H^{0/+}$, i.e., H in form of atoms or protons. This result come from a survey of all the completed experiments and their intra-comparison, but largely stems from the desorption and dynamical patters in QENS data and elemental line shifts of S and Mo from XPS. The QENS spectra for H/MoS_2 exhibit only one motion mode in contrast to our previous study on electrolysis loaded samples [122], where we found clear evidence of two diffusion processes. For the electrolytically loaded samples the motion of hydrogen molecules within the material was identified as the major contribution, leading to the fast diffusion process. Since H_2 does not diffuse through MoS_2 layers, these molecules must have been formed by recombination of H atoms within the material. This process, apparently, does not dominate in case of H atom beam loading. Nevertheless,

the slower diffusion component of the electrolytically loaded samples displays a similar broadening as the motion observed in the present experiments and could possibly be caused by $H^{0/+}$ diffusion.

The study of the in-plane movement of atomic hydrogen, i.e., motion parallel to the MoS_2 layers, discovered a moderately swift diffusion with $D \approx 1 \cdot 10^{-9}$ m^2/s. The data suggests the interpretation in terms of Brownian diffusion, however, within the explored momentum transfer range Brownian and jump diffusion with a continuous distribution of jump lengths could not be resolved with confidence. No spatial confinement was observed at the examined temperatures, as expected for diffusing species of the size of an H atom (or proton). The diffusion coefficient appeared to be the same at 300 and 400 K, however, two data points are not enough to establish a statistically justified interpretation. Compared to atomic hydrogen diffusion on a Pt surface [111], the experimentally observed motion of H atoms in crystalline MoS_2 is slower by an order of magnitude, but, as numerical simulations suggest, could be largely influenced by the particular structure of MoS_2, which is known to have two naturally occurring polytypes, namely, 2H-MoS_2 (most frequent, studied in this work) and 1T-MoS_2 (more rare) [123]. Therefore, the diffusion of hydrogen still seems to be able to play a role in the catalytic mechanism, since it provides means to vacate an active site by making available non-reactive parts of the surface.

4.5 Special acknowledgements

The MD simulations part presented in this work was carried out together with the Master's student, Leran Lu. The work was distributed in a way that Leran was mainly in charge of constructing the system and running the simulations, and I took a large part in the interpretation of the results, as well as detecting errors in the simulations.

Molybdenum disulphide and molybdenum carbide powders, voltammetry study

Chapter 5

Molybdenum disulphide and molybdenum carbide powders

5.1 Cyclic and linear voltammetry

This part of the project was carried out in Westfälische Hochschule, Gelsenkirchen and Recklinghausen, Germany, year 2020, therefore it was largely affected by Covid-19. The university campus in Gelsenkirchen was a place where all the powder voltammetry experiments were carried out, and in Recklinghausen tutoring of a Bachelor's student took place. As a non-chemist and having little hand-on experience with voltammetry, I was not granted a free access to the laboratory in Gelsenkirchen and could only work under the supervision of laboratory staff, who in my case was Dr. Norbert Kazamer, most of the time. Due to Covid-19 restrictions the number of experiments I could carry out was limited, and since a lot of test measurements were required in order to establish a reliable set-up, only a few real experiments could be performed. Having said that, we can proceed with the description of the study of molybdenum sulphide and carbide by means of cyclic and linear voltammetry.

The MoS_2 and Mo_2C powders, with particle sizes in the range of nanometers and micrometer, respectively, were acquired from Sigma-Aldrich. For the wet chemistry measurements the inks of the studied powders were produced using the following procedure: 100 g of MoS_2 powder were mixed with 2 ml of distilled water, and subsequently the solution was stirred for 25 minutes in

an ultrasonic bath. After that 300 mg of 5 % Nafion solution from QuinTech[1] was added to the mixture, followed by another 5 minutes of ultrasonification. At this state the ink is deemed to be prepared. For the Mo_2C powder the procedure was the same, except for the mass of powder and Nafion used, which in this case were 200 mg of Mo_2C and 400 mg of Nafion solution. The relative amounts of a catalyst powder, water and Nafion solution were established after a series of cyclic voltammetry experiments, where various ratios were tested, including the ones obtained from the literature [18]. The eventual composition is the one that yielded relatively consistent results, but may not be the most efficient one, overall. Additionally, inks based on isopropanol and on ethanol were tested, however, their low surface tension was not suitable for drop casting, and therefore they were discarded.

For the cyclic and linear voltammetry a rotating disk electrode (RDE) set-up was used, with a 0.5 M H_2SO_4 electrolyte, saturated calomel reference electrode (SCE), Pt wire as a counter electrode, and glassy carbon tip as a working electrode, with the latter being in two configurations, 3 and 5 mm in diameter, which was taken into account during calculations. Before each measurement the tips were polished using a 3 μm diamond suspension and washed with ethanol. After these manipulations, a studied ink was drop casted on the as-prepared glassy carbon tip and left in air until water is fully evaporated. For $\sim$10 minutes, shortly before the measurement, the electrolyte was deaerated to remove any oxygen, dissolved during the preparation process. Test measurements revealed, that if drop casting is successful, then rotation of the electrode does not significantly affect the results, and therefore can be omitted.

Linear voltammetry measurements were performed in potential range {0; -0.8} V with 10 mV/s scan rate and 10 mV potential step. Several LV scans were performed to ensure the short-term stability of the electrodes. After that, without touching the experimental layout, the CV measurements were carried out. The working potential range, as well as the scan rate, were established in test experiments at values {-0.4; 0.6} V and 200 mV/s, respectively. With a potential step of 10 mV these settings proved to be a decent choice in terms of signal to noise ratio. For each sample 50 cycles were measured as it is a generally accepted minimum number of cycles allowing to access the long-term stable performance of an electrode. After CV scans, extra LV measurements were performed, which did not show significant difference with

[1]https://www.quintech.de/en/produkte/components/solutions-emulsions/ns-5-2/

respect to the pre-CV curves.

5.2 Results and discussion

Among a series of voltammetry experiments, one set poses a particular interest and will be presented here. For it, first of all, two inks were prepared 15 days before the measurements, one with MoS_2 and one with Mo_2C powder. These inks showed decent results in terms of yielded current stability and quality for drop casting, therefore the decision was made to proceed working with these inks and repeat the experiment, in order to test the reproducibility. Due to Covid-19 restrictions, the next measurement could only be scheduled in two months, which actually turned out to be beneficial, because it forced us to examine also the ageing of the powders. Surprisingly, the results turned out to be completely different from the initial scans, meaning that the powders, being soaked in water, change their activity over time. Hence, here we will compare the two experiments, where the first one we will call "Fresh", and the second one "Aged".

Let us start with the linear voltammetry (LV) experiment. Here the main extracted parameters which characterise a catalyst are yielded current at a given potential and Tafel slope. From a plot of current density versus applied potential with respect to Saturated calomel electrode (SCE) it is clear that a much smaller voltage is required in order to reach a substantial current flow with the aged, water infused catalyst powders (Fig. 5.1). A 30 $mA \cdot cm^{-2} \cdot mg^{-1}$ limit is reached at around -410 mV applied potential with the freshly prepared inks, and at -340 and -220 mV with the aged Mo_2C and MoS_2 respectively. These values give a comprehensible view on the catalyst's activity, however, they are not easily comparable with the literature. Instead, it is more common to use the Tafel slope, a derived parameter with a property that the lower it is, the better the performance. In case of the studied powders the Tafel slope decreases from around 200 mV/dec for the fresh samples to 65 mV/dec in average for the aged ones. The former value indicates a poor performance, as expected for the plain powders under study, however, the latter is already close to the state-of-the-art MoS_2 based catalysts with 32 mV/dec Tafel slope [40]. Therefore, even without complex synthesis procedures it was possible to achieve a decent catalytic activity by simply letting the powders infuse in water. Before attempting to understand the reasons for such a spike in performance, it is important to also have a

look at the stability of the produced samples.

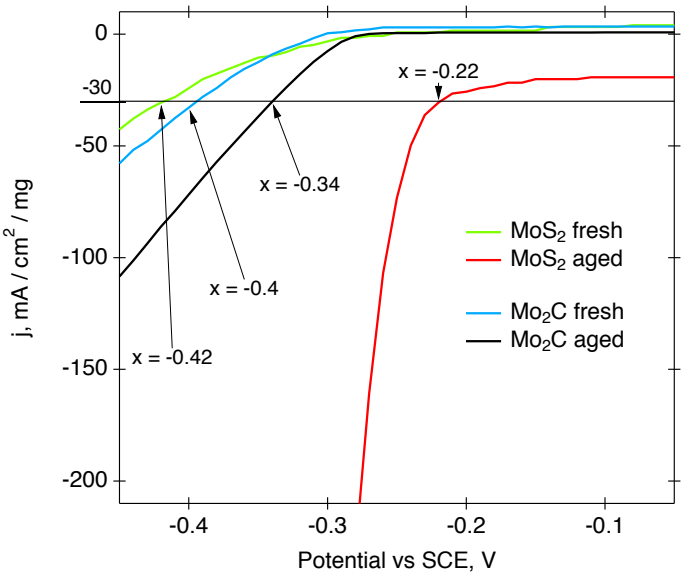

Fig. 5.1: Linear voltammogram of Mo_2C and MoS_2 inks prepared 15 days before the measurement (fresh, green and blue lines) and 2 months later (aged, red and black lines).

The stability can be accessed via cyclic voltammetry (CV), which consists of a series of electrochemistry scans of the catalytic powder under study within a predefined potential range while monitoring the current response of the system. In the chosen here notations the top part of the curve (positive current) represents oxidation phenomenon, and the bottom part corresponds to reduction (negative current) (Fig. 5.2). Obviously, the MoS_2 powder exhibits an extraordinary increase in yielded currents after being soaked in H_2O, however, the signal is highly unstable and changes with every few cycles, especially in the oxidation region. In this region two peaks can be distinguished, at around -0.10 and 0.25 V. Tentatively they can be assigned to hydrogen and oxygen oxidation, at lower and higher potential, respectively. The reduction part of the curve is not as impressive, but still a feeble peak at around 0 V can be noted, which most probably represents hydrogen reduction. This indicates an imbalance in the hydrogen oxidation-reduction cycle, caused by more facile oxidation. Allowing for the preparation process, the latter can be explained assuming that during ageing in water, MoS_2 promoted adsorption of hydrogen atoms, which could subsequently migrate from the active sites to nearby locations. As it was described in section 4.3.1, XPS studies on MoS_2

crystals suggest that water can access various cracks or voids in the material. Although the presence of cracks in nanosized particles of a powdered compound is unlikely, there must be a large number of grain boundaries due to natural agglomeration. The intercalation of water molecules into these boundaries exposes a much greater number of edge S atoms to hydrogen in the solution, thus, enhancing the adsorption. Therefore, since in our case the oxidation part of the CV curve represents hydrogen desorption, a substantial number of pre–adsorbed hydrogens would indeed increase the oxidation signal, without amplifying the reduction part. The irregularity of the oxidation peak (Fig. 5.2) should be linked to diversity of possible hydrogen storage sites, which are being unfolded at different stages of the cyclic voltammetry experiment. Here we recall, that the observed effect of signal amplification only becomes significant in 2-3 months after ink preparation, therefore, whatever the underlying phenomenon is, it should be extremely slow.

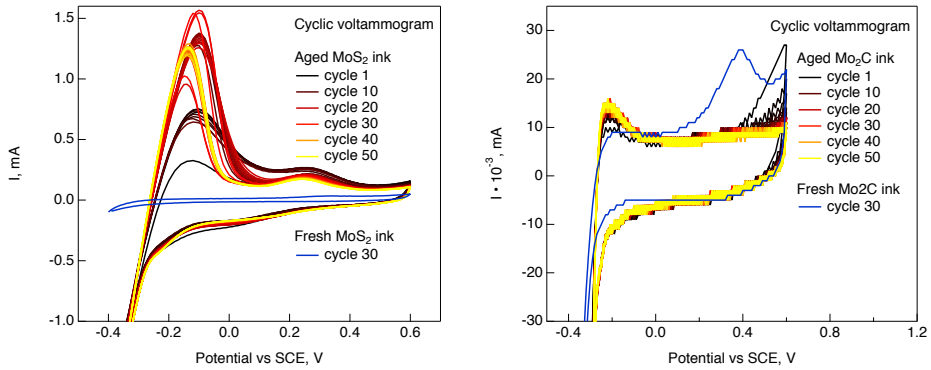

Fig. 5.2: Cyclic voltammograms of MoS_2 (left) and Mo_2C (right) based inks. The scans performed within 15 days from the preparation of the inks (fresh) are displayed in blue. For each sample only one "fresh" scan is shown, because most of the others are the same. The scans performed between two and three months from the preparation of the inks (aged) are shown via colour gradient from black to yellow. All 50 cycles are presented, however, the legend only indicates the colours of several intermediate scans, due to size restrictions of the plot. Note that the scale if different in the two graphs, milliamperes for MoS_2 and microamperes for Mo_2C.

Next we turn to the Mo_2C sample, which does not show as much difference after ageing as the MoS_2 one does. Here the water infusion process leads to a disappearing of the oxygen oxidation peak (at 0.4 V) and a rise of the hydrogen oxidation peak (at -0.2 V) (Fig. 5.2). However, the overall current response in the main CV region stays below 30 μA in the absolute value,

as compared to MoS_2, where it rises to 1.5 mA. In the reduction part of the curve a slight enhancement of the hydrogen reduction signal is observed, however the peak cannot be resolved.

From a CV peak it is possible to estimate the active surface of the electrode versus a reaction, corresponding to the chosen peak. Here we will only be interested in hydrogen reduction and oxidation reactions. The estimation is based on the fact, that during the reduction of the catalyst, protons from the solution are adsorbed on the active sites of the electrode. During oxidation these H atoms desorb, supplying the system with an electron:

$$H_{ad} \rightarrow H^+ + e^-. \tag{5.1}$$

The number of liberated electrons is, therefore, directly connected to the number of active sites of the electrode, and can be measured as yielded current. With a knowledge of the total number of surface atoms, the percentage of active sites can be calculated. Hence the hydrogen reduction peak gives the number of adsorption sites, and hydrogen oxidation peak shows the amount of desorbed H atoms. The area of a peak, A, is related to the emitted charge via the following equation:

$$C = \frac{A}{\nu S}, \tag{5.2}$$

where ν is the scan rate in V/s and S is the area of the electrode. The values calculated based on the most representative scan of both MoS_2 and Mo_2C, cycle number 50, are as follows. For hydrogen reduction on MoS_2, $C_{red}(MoS_2) \approx 10\ \mu C/cm^2$, hydrogen oxidation on MoS_2, $C_{ox}(MoS_2) \approx 276\ \mu C/cm^2$ and on Mo_2C, $C_{ox}(Mo_2C) \approx 1\ \mu C/cm^2$. Converting Coulombs to elementary charges and considering hydrogen adsorption only at the topmost, perfectly flat layer of a material, and hence normalising to one surface atom per unit cell of the corresponding compound, we end up with a rough estimation of hydrogen uptake/desorption in perfect MoS_2 and Mo_2C. The assumption of perfectly flat surface is, no doubt, rather far from reality, therefore in the further considerations keep in mind an error of about half the values provided. In case of molybdenum disulphide we observe, from the reduction peak, that in average 62 H atoms are adsorbed per 1000 unit cells, while the oxidation peak shows that almost 2 H atoms are desorbed per one surface S atom. This suggests that during ageing hydrogen is adsorbed not only at the surface, but also in the subsurface region. The analysis of the surface peak of water loaded MoS_2 crystals also points at more than one

monolayer of hydrogen adsorbed near the surface, although, large statistical errors should be taken into account in this case as well. For the Mo_2C the number of desorbed hydrogens is estimated at a level of 3 atoms per 1000 S atoms, thus, the adsorption pattern must be even more feeble and definitely inferior to that of MoS_2. Comparing the results to the linear voltammetry experiment, we see, as expected, that the main trend is the same for LV and CV, i.e. after ageing in water both catalyst powders exhibit an increase in their activity, while for Mo_2C the enhancement is moderate and for MoS_2 it is colossal.

There is another possible explanation for the activity enhancement of MoS_2, which we would like to put forward. Molybdenum sulphide powder, provided by the manufacturer in a nanometre size, may agglomerate over time. Ultrasonification, which the ink was subjected to during the preparation process, should promote disintegration of the agglomerates to some extend, however, with no external force preventing the particles to stick together, the clustering must occur again. In case of MoS_2 water may provide this force. It is known that molybdenum disulphide possesses moderate hydrophobic properties, therefore, during ultrasonification, H_2O molecules may repel freshly fractured pieces of MoS_2, preventing them from sticking together again, thus reducing the average particle size in the system. In course of ageing, the MoS_2 ink in its vial used to separate into powder at the bottom and water at the top, hence both MoS_2 and Mo_2C inks[2] were subject to intermediate ultrasonification a few times between the first and the second experiment. Therefore, if indeed water averts MoS_2 powder clustering, then several extra ultrasonification runs could revert it to a nanopowder state. Nanoparticles are well known to have an enhanced catalytic activity, therefore the overall increase in the performance of MoS_2 could also be attributed to the described here phenomenon. However, it does not account for the reduction-oxidation imbalance, hence hydrogen adsorption must occur in this case as well.

It is possible that during ageing hydrogen atoms were incorporated in the MoS_2 matrix in such a way or concentration that they slightly deformed the crystal structure of MoS_2 particles. This could also affect the catalytic properties of the powder. The most convenient way to assess this phenomenon is X-ray (powder) diffraction (XRD). For this experiment, which was conducted on the PANalytical Empyrean X-ray bench at the EPN campus[3] (Grenoble,

[2]The Mo_2C ink did not separate into layers, the additional ultrasonification cycles were carried out for the purposes of symmetry with MoS_2

[3]European Photon and Neutron Science Campus, IRT Nanoelec Advanced Character-

France), equipped with Cu source (8 keV), two powdered samples were prepared, one was not modified by any means, and another one was mixed with distilled water and left to infuse for 2.5 months, with several intermediate ultrasonification runs. Shortly before the experiment several drops of the ink with the MoS_2 powder were cast on a piece of beryllium foil and left in a furnace under 80 C° until fully dry. Beryllium foil with the catalyst powder on top was then used in the sample holder assembly for the XRD measurement. Drying left a relatively smooth disk of MoS_2, therefore it was gently crushed into smaller grains in order to mitigate the orientational effects of the crystallines.

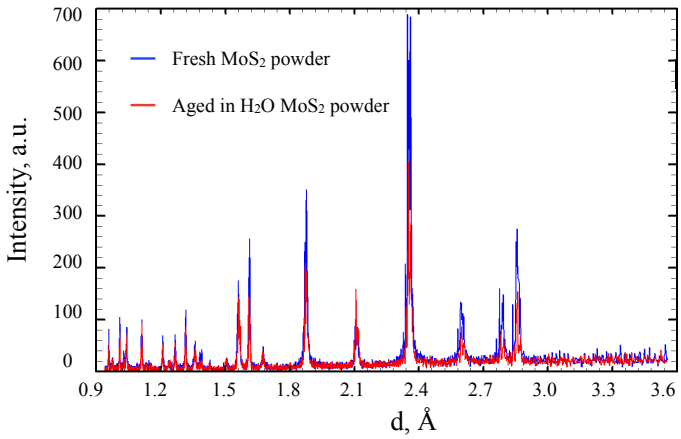

Fig. 5.3: X-ray diffraction pattern of a fresh, as received MoS_2 powder (blue line) and an aged in H_2O for 2.5 months powder (red line).

X-ray scattering pattern of a crystalline material consists of a sequence of peaks, the positions of which reflect the average structure over all the small crystallines in the examined powder. By looking at the experimental spectra of the fresh and aged MoS_2 powders, it becomes evident that the peak positions are identical (Fig. 5.3), meaning that the unit cell and the structure remain unchanged. This, however, does not prohibit small deformations at the very surface of the MoS_2 particles. Also, X-rays are most sensitive to heavy elements, like molybdenum, hence sulphur makes only a minor contribution to the overall pattern. Therefore, although the unit cell does not

isation Platform

change, it does not mean that S atoms remain in the exact same positions. This could be checked by carefully comparing the intensities of the peaks, but a strong orientational effect, which, eventually, could not be omitted by simple specimen manipulations, forbids us from doing so. The scanning electron microscope photos, taken at Westfälische Hochschule, Recklinghausen, Germany, reveal that even in powdered state MoS_2 particles preserve a flake-like form in the majority (Fig. 5.4). Since for the XRD experiment the examined powder sample was moderately compressed between two Be foils, it is natural that some preferred orientation would appear, and this orientation is not necessary the same for different experiments.

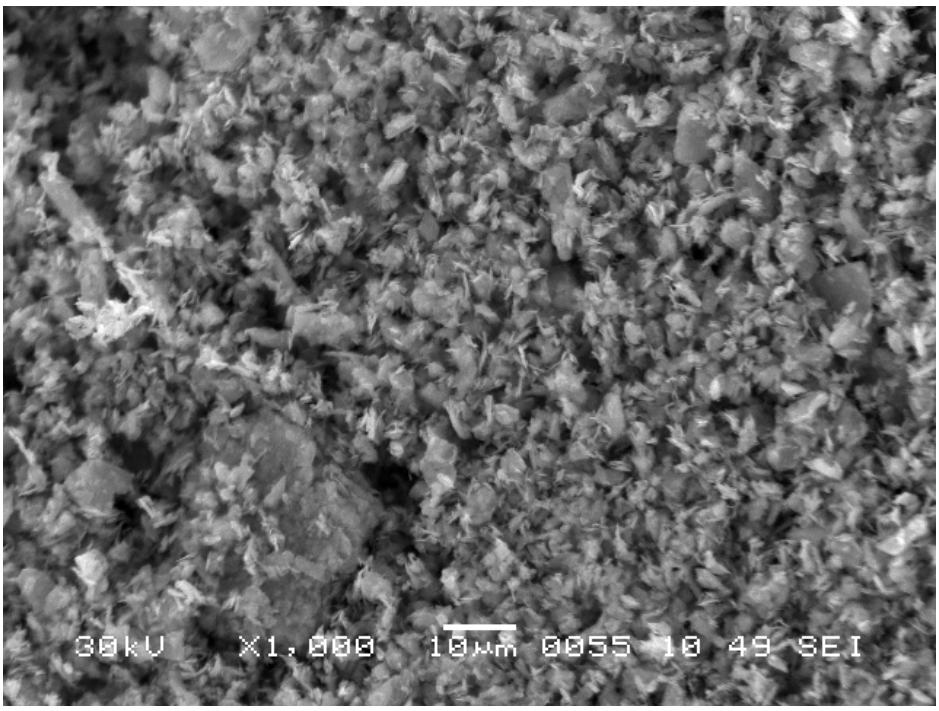

Fig. 5.4: Scanning electron microscope photograph of a fresh, as received MoS_2 powder. The scale is 10 μm and is indicated in the figure.

After the activity enhancement phenomenon was discovered for the powders, an MoS_2 single crystal was additionally tested to see whether it would exhibit similar behaviour. The experiments for this part of the project were conducted by a chemistry Bachelor's student Alexander Graf, for whom it was a part of his internship at the Westphalian University under

the supervision of Prof. Franziska Traeger (my co-supervisor). I collaborated closely with Mr. Graf, acting as a mentor and instructor, but could not participate in every measurement he has performed. The MoS_2 single crystal had been first measured without any pretreatment, and then soaked in water for almost 2 months, after which another CV experiment was carried out. Interestingly, the current response did not increase, but rather slightly decreased after ageing. Here two aspects need to be discussed, but first we would like to note that the slight decrease in the current yield should, most probably, be attributed to the inconsistency of the experimental layout, used in this case, but not to any extra phenomenon. Unlike in the experiments with powders, here the crystals must have been mounted ensuring the best connection to the supporting Ta plate, which could not be done consistently with the available tools. Also the distance between the electrodes was estimated mainly by eye, which additionally increases the overall systematic error.

With that being said, we continue the discussion considering that the activity of MoS_2 did not change after ageing within the errors of the experiment. It is known that MoS_2 in a single crystal state possesses a much lower density of active sites, since mostly S atoms near edges or defects are considered as such. However, the yielded current is comparable to the one given by the fresh powder, therefore the much larger size of the crystal as compared to the electrode prepared via drop-casting must equilibrate the total number of active sites, to some extend. If the whole activity boost effect for the MoS_2 powder was due to hydrogen adsorption and diffusion, then at least some increase must be seen with the single crystals as well, since we have an indication that the number of active sites is not extremely different and in a scale of several unit cells the diffusion of hydrogen within a crystalline in a powder must be the same as in a single crystal. Therefore we may conclude that hydrogen adsorption and diffusion cannot solely induce the observed activity enhancement. Hence the fragmentation during ultrasonification is an paramount step in this process, since it increases the amount of exposed edge S atoms significantly.

By summarising the available information we can say, that hydrogen interaction with molybdenum disulphide plays an important role in its catalytic properties, and probably a much greater role than it is for dimolybdenum carbide. Ageing of MoS_2 powder in water with intermediate ultrasonification runs drastically enhances its activity versus both hydrogen reduction and oxidation reactions. Ultrasonification appears to be a key step, since is

promotes the splitting up of the accumulated agglomerates. During ageing MoS_2 adsorbs a large number of H atoms, most probably with the help of their migration from catalytically active to plain subsurface sites. These intercalation events do not affect the global structure of MoS_2 particles in a detectable with a laboratory XRD source way. The phenomena occurring upon a long lasting exposure of MoS_2 powder to distilled water appeared to be more complex then expected and require a broader study. Perhaps, various modifications may shorten the ageing period, which is, no doubt, a major obstacle for such kind of experiments. First of all, it should be tested whether several (at least 5) ultrasonification runs over the course of one week enhance the activity in any way. If not, then, perhaps, keeping the ink warmed up would speed up the process by increasing the frequency of water - MoS_2 interaction.

Chapter 6

Conclusions

In summary, we have studied MoS_2 crystals loaded via three methods, namely, electrolysis (H^+/MoS_2), H atom beam bombardment (H/MoS_2), and soaking in water (H_2O/MoS_2). The main means of investigation were quasi-elastic neutron scattering via time-of-flight and spin-echo spectroscopy, X-ray photoelectron spectroscopy and nuclear reaction analysis. Additionally, the electrochemical properties of MoS_2 and Mo_2C powders were examined by means of linear and cyclic voltammetry.

The water loaded crystals exhibited a diffusion mode easily distinguishable from other samples. This means that the signal comes from adsorbed water, and that the other samples do not contain it in significant quantities. The electrolytically loaded MoS_2 crystals yielded a QENS spectrum clearly showing two diffusion modes: One is the fastest among all the samples, and the other has a quasi-elastic broadening in the same range as H/MoS_2 exhibits. At the same time, the Q dependence of these two latter modes is clearly different. The QENS broadening detected for H/MoS_2 follows the DQ^2 law, while the one for H^+/MoS_2 is almost constant versus Q. Therefore, in our interpretation the slow motion observed for the electrolytically loaded crystals was described in terms of rotational diffusion of recombined H_2 molecules. However, we do not fully exclude the possibility of it being exhibited by atomic hydrogen. Protons, as DFT studies report [42], should not be considered as a separate diffusion species, since in MoS_2 they bind to sulphur, get neutralised, and act very similarly to neutral H atoms onwards. Hence the fast translational diffusion mode in H^+/MoS_2 was attributed to H_2 molecules, but not the same molecules as the ones performing slow rotations. We found that adsorbed water tends to occupy various voids or cracks in the

material, therefore it is natural to assume that recombined H_2 molecules can also access similar regions and move there rather freely.

The fact that the electrolytically loaded MoS_2 crystals contain recombined H_2 molecules, while the H atom beam bombarded ones do not, could be explained in different ways. Recalling that H^+/MoS_2 contained much higher amount of hydrogen than H/MoS_2, the recombination could simply be caused by high hydrogen density. Also it is possible that electrolysis itself promoted recombination of H_2 molecules by affecting the chemistry of MoS_2. This could be expected since generation of hydrogen gas is one of the purposes of water electrolysis. The recombined H_2 are trapped inside the material rather strongly and are still present even when the crystal is heated to 500 K, which is an undesired feature when HER catalysis is concerned, as the aim is usually to generate and extract hydrogen gas, but not to keep it inside. The H_2 molecules are distributed around the crystal: Part of them is caged between sulphur atoms of two adjacent MoS_2 layers, while others dwell within grain boundaries or vacancies agglomeration, where they perform fast long-range diffusion parallel to MoS_2 basal planes with D around $4 \cdot 10^{-8}\ m^2/s$. As MD simulations suggest, the penetration of MoS_2 layers by H_2 molecules is strongly hindered. Given also the fact, that in NRA we observed similar diffusion rates into the bulk for H^+/MoS_2 and H/MoS_2 over a large time frame, it can be assumed that recombined H_2 can dissociate again into atoms on MoS_2 matrix and traverse the layers in this form. The low accuracy of the exploited technique towards the extracted type of results, however, does not allow to make a firm statement in this regard.

The atom beam loaded crystals do not contain any significant amount of H_2 or H_2O molecules which are able to move fast enough to be detected within the spectroscopic window of our experiments. Therefore, the observed hydrogen species in H/MoS_2 are most probably H atoms, either neutral or in form of protons, as the latter move in almost the same way, as neutral atoms do [42]. In short-range the diffusion of H parallel to the MoS_2 basal planes is unobstructed and resembles Brownian motion. As compared to atomic H diffusion on a surface of currently the most active HER catalyst, platinum, in MoS_2 it is one order of magnitude slower. Faster movement signifies a possibility for more frequent interactions between adsorbed H atoms, which is an important part of Tafel recombination mechanism. Our MD simulations suggest that in MoS_2 the diffusion rate can be enhanced by destabilising the structure: Introducing heavy layer shearing and stacking defects. Of course, in a real crystal such alterations are improbable, at least, below the temper-

ature of hydrogen desorption. However, a specially prepared polycrystal with large number of grain boundaries and other 2D defects may be expected to provide enough free space for more swift H diffusion. Another important feature of atomic hydrogen mobility in MoS_2 is the relatively small temperature range between the initiation of fast diffusion and the complete desorption of the corresponding species. It starts around room temperature, where only 20 % of H atoms are mobile within the spectroscopic window of our experiment, continues at 400 K, where this value increases to almost 50 %, and ends between 450 and 500 K, where 100 % mobility can be anticipated. This means that the electrolysis at high temperature may be more efficient than at room temperature also because of enhanced hydrogen mobility. At the same time, this feature did not allow us to calculate the activation barrier, since the value obtained based on only two temperature points is unreliable. We note that there can still be some hydrogen species in MoS_2, which are immobile at 500 K, and which fall out of scope of the current study. The NRA measurement performed for the purposes of MoS_2 cleaning optimisation revealed the presence of hydrogen up to 700 K. The results of the XPS experiment suggest that H atoms in MoS_2 are stored both within -SH groups, as in a perfect structure, and in the vicinity of sulphur vacancies, where the binding energy in higher. They become mobile at different temperatures, and the data supports the idea that vacancies accommodate more H atoms than the perfect matrix. We note that the diffusion properties of these two types of hydrogen must be indistinguishable after the initiation of their migration.

The MoS_2 crystals that were soaked in water showed the presence of substantial amount of physisorbed H_2O molecules. They require the highest temperature among all the species to be desorbed, despite not being able to penetrate the perfect MoS_2 matrix. Most probably they settle around the voids and other large enough volume defects, where liquid-water-like diffusion is possible. Whether it is governed by the motion and collisions of the H_2O molecules within the volume of the void, or hopping of hydrogen atoms between oxygen and sulphur atoms is yet to be discovered. For the application part of the problem, it is important that liquid water can access defective regions of MoS_2, where more exposed S atoms, which are considered reactive, could be present. This effect was probably observed in our electrochemical experiments.

The voltammetry measurements considered not only MoS_2, but also Mo_2C powders, which are both considered catalytically moderately active. The MoS_2 powder that was infused in water exhibited extraordinary increase

in catalytic efficiency, while Mo_2C did not. This enhancement can be connected with the ability of water to squeeze into the grain boundaries of MoS_2. Indeed, if this is the case, then water would help the fragmentation of the powder, at the same time preventing its natural agglomeration, increasing the overall amount of exposed active sites. The structure of MoS_2 particles does not change after water infusion, supporting the idea that H_2O molecules cannot be intercalated into its matrix.

6.1 Outlook

The study presented in this work gives a broad picture of hydrogen diffusion in MoS_2, which is important for obtaining a better understanding of the processes, occurring during the catalysis of the hydrogen evolution reaction. We found that electrolysis results in significant amount of H_2 molecules being trapped inside the material. However, our MD simulations suggest that the energy barrier for the in-plane diffusion is not extremely large. With slight structural modifications, which would increase the distance between MoS_2 layers, this type of motion can be activated, and more H_2 could be released from the sample during electrolysis. This issue should be probably first addressed via DFT studies, and later tested in experiment. For the nanosized MoS_2 particles, due to high surface to volume ratio, there would not be any substantial rise in generated H_2 even if all of our assumptions are true. However, if the idea succeeds, then microsized powders could come closer to nanosized in terms of catalytic activity, and the former are more stable and much easier to produce.

The role of defects is sometimes underestimated in the modern numerical simulation studies on MoS_2, which are aimed at revealing the HER mechanism. However, our study shows that various structural defects may play an important role in the overall hydrogen diffusion mechanism, which is crucial for the Tafel reaction step, and also affects the Heyrovsky step. Of course, there exist investigations specialised on defect manufacturing for the purpose of enhancing the HER catalytic activity [37], and they are widely known. However, the studies, which compare the energetics of the Volmer, Tafel and Heyrovsky reaction steps, tend to use perfect MoS_2 structure as a substrate [30, 38, 41]. It would be important to make a similar comparison on a defective MoS_2 matrix.

The ability of MoS_2 crystals to hold large amount of H_2 is of a particu-

lar interest for the hydrogen storage community. Electrolysis is a relatively simple method for hydrogen incorporation, and, as we have seen in our test experiments (Fig. 4.1), approximately 20-30 min of baking at 700-750 K is enough to release all of the stored hydrogen. Unfortunately, the total amount of hydrogen stored in electrolytically loaded samples could not be established with confidence in the current work, hence it is problematic to compare MoS_2 to other hydrogen storage materials in terms of their performance. However, to be fair, it was not one of the aims we put for this study. For this purpose a much more meticulous NRA experiment would be required, with a carefully prepared and stored in vacuum samples, and a non-default type of data reduction, which would include corrections for the thick target approximation for the topmost layers of MoS_2. As our study suggests, various plane and volume defects are crucial for H_2 storage, since they provide valuable free space and S edge sites for H_2 recombination from H/H^+. This means that for further studies of MoS_2 as a hydrogen gas storing material it would make sense to investigate crystals of natural origin or powders produced via ball milling.

The cause of the catalytic activity spike, reached after MoS_2 powder infusion in water, remains veiled. Nevertheless, such a convenient method of catalyst efficiency enhancement could be used in industry to produce inexpensive decently reactive electrodes, although some difficulties may be encountered due to the long ageing period. It would be beneficial if this period was decreased to several days or hours. In order to achieve it, more experiments are required, aimed at discovering the cause of the activity increase. Most probably two main factors are powder fragmentation during ultrasonification with further absence of agglomeration due to water repulsive properties, and slow hydrogen adsorption from surrounding water and migration of adsorbed species one or two layers deep. The former factor can be easily sped up by running the ultrasonification for longer times, or in several successive runs. The adsorption is more complex. Elevated temperatures may help accelerating the process, but not to the level of several hours. If adsorption actually plays the major role, then structural modifications, probably via doping, may be required to achieve the desired time frame. To approach the issue of catalytic enhancement it would be efficient to start with preparing a series of MoS_2 nano-powder based samples (inks) with varying ultrasonification sequences/procedures. This will allow to asses the influence of powder fragmentation without taking too much time on ageing processes. The other set of samples would be MoS_2 powders infused in water for different periods

of time. These inks should only be briefly ultrasonificated once during the initial preparation, in order to isolate the effect of hydrogen adsorption on the voltammetry curves.

6.2 Conclusions

En résumé, nous avons étudié des cristaux MoS_2 chargés via trois méthodes, à savoir l'électrolyse (H^+/MoS_2), le bombardement par faisceau d'atomes H (H/MoS_2), et le trempage dans l'eau (H_2O/MoS_2). Les principaux moyens d'investigation étaient la diffusion quasi-élastique des neutrons via la spectroscopie de temps de vol et d'écho de spin, la spectroscopie de photoélectrons X et l'analyse des réactions nucléaires. De plus, les propriétés électrochimiques des poudres MoS_2 et Mo_2C ont été examinées au moyen de voltamétrie linéaire et cyclique.

Les cristaux chargés d'eau présentaient un mode de diffusion facilement distinguable des autres échantillons. Cela signifie que le signal provient de l'eau adsorbée, et que les autres échantillons n'en contiennent pas en quantité significative. Les cristaux MoS_2 chargés électrolytiquement ont donné un spectre QENS montrant clairement deux modes de diffusion : l'un est le plus rapide parmi tous les échantillons, et l'autre a un élargissement quasi-élastique dans la même plage que H/MoS_2. Dans le même temps, la dépendance Q de ces deux derniers modes est clairement différente. L'élargissement QENS détecté pour H/MoS_2 suit la loi DQ^2, tandis que celui pour H^+/MoS_2 est presque constant en fonction de Q. Par conséquent, dans notre interprétation, le ralentissement observé pour les cristaux chargés électrolytiquement ont été décrits en termes de diffusion rotationnelle de molécules H_2 recombinées. Cependant, nous n'excluons pas complètement la possibilité qu'il soit présenté par l'hydrogène atomique. Les protons, comme le rapportent les études DFT [42], ne doivent pas être considérés comme une espèce de diffusion distincte, car dans MoS_2 ils se lient au soufre, se neutralisent, et agissent de manière très similaire aux atomes H neutres. Ainsi, le mode de diffusion translationnelle rapide dans H^+/MoS_2 devrait être attribué aux molécules H_2, mais pas aux mêmes molécules que celles effectuant des rotations lentes. Nous avons constaté que l'eau adsorbée a tendance à occuper divers vides ou fissures dans le matériau, il est donc naturel de supposer que les molécules H_2 recombinées peuvent également accéder à des régions similaires et s'y déplacer assez librement.

Le fait que les cristaux de MoS_2 chargés électrolytiquement contiennent des molécules de H_2 recombinées, alors que ceux bombardés par le faisceau d'atomes H n'en contiennent pas, pourrait s'expliquer de différentes manières. En rappelant que H^+/MoS_2 contenait une quantité d'hydrogène beaucoup plus élevée que H/MoS_2, la recombinaison pourrait simplement être causée par une densité d'hydrogène élevée. Il est également possible que l'électrolyse elle-même ait favorisé la recombinaison des molécules H_2 en affectant la chimie de MoS_2. On pouvait s'y attendre puisque la génération d'hydrogène gazeux est l'un des objectifs de l'électrolyse de l'eau. Le H_2 recombiné est piégé à l'intérieur du matériau assez fortement et est toujours présent même lorsque le cristal est chauffé à 500 K, ce qui est une caractéristique indésirable en ce qui concerne la catalyse HER, car le but est généralement de générer et d'extraire de l'hydrogène. gaz, mais pas pour le garder à l'intérieur. Les molécules H_2 sont réparties autour du cristal : une partie d'entre elles est emprisonnée entre les atomes de soufre de deux couches MoS_2 adjacentes, tandis que d'autres résident dans les joints de grains ou l'agglomération des lacunes, où elles effectuent une diffusion parallèle rapide à longue distance. vers MoS_2 plans basaux avec D autour de $4 \cdot 10^{-8}\ m^2/s$. Comme le suggèrent les simulations MD, la pénétration des couches MoS_2 par les molécules H_2 est fortement entravée. Compte tenu également du fait que, dans la NRA, nous avons observé des taux de diffusion similaires dans la masse pour H^+/MoS_2 et H/MoS_2 sur une longue période, on peut supposer que recombiné H_2 peut se dissocier à nouveau en atomes sur la matrice MoS_2 et traverser les couches sous cette forme. La faible précision de la technique exploitée vis-à-vis du type de résultats extraits ne permet cependant pas de faire une déclaration ferme à cet égard.

Les cristaux chargés par le faisceau d'atomes ne contiennent aucune quantité significative de molécules H_2 ou H_2O capables de se déplacer suffisamment rapidement pour être détectées dans la fenêtre spectroscopique de nos expériences. Par conséquent, les espèces d'hydrogène observées dans H/MoS_2 doivent être des atomes H, soit neutres, soit sous forme de protons, car ces derniers se déplacent presque de la même manière que les atomes neutres [42]. A courte distance, la diffusion de H parallèlement aux plans basaux MoS_2 n'est pas obstruée et ressemble au mouvement brownien. Par rapport à la diffusion atomique de H sur une surface du catalyseur HER actuellement le plus actif, le platine, dans MoS_2, elle est d'un ordre de grandeur plus lente. Un mouvement plus rapide signifie une possibilité d'interactions plus fréquentes entre les atomes de H adsorbés, ce qui est une

partie importante du mécanisme de recombinaison de Tafel. Nos simulations MD suggèrent que dans MoS_2 le taux de diffusion peut être amélioré en déstabilisant la structure : en introduisant des défauts de cisaillement et d'empilement de la couche lourde. Bien entendu, dans un cristal réel, de telles altérations sont improbables, du moins, en dessous de la température de désorption de l'hydrogène. Cependant, on peut s'attendre à ce qu'un polycristal spécialement préparé avec un grand nombre de joints de grains et d'autres défauts 2D fournisse suffisamment d'espace libre pour une diffusion H plus rapide. Une autre caractéristique importante de la mobilité de l'hydrogène atomique dans MoS_2 est la plage de température relativement petite entre l'initiation de la diffusion rapide et la désorption complète de l'espèce correspondante. Elle commence vers la température ambiante, où seuls 20 % des atomes H sont mobiles dans la fenêtre spectroscopique de notre expérience, se poursuit à 400 K, où cette valeur augmente à près de 50 %, et se termine entre 450 et 500 K , où une mobilité de 100 % peut être anticipée. Cela signifie que l'électrolyse à haute température peut être plus efficace qu'à température ambiante également en raison de la mobilité accrue de l'hydrogène. Dans le même temps, cette fonctionnalité ne nous a pas permis de calculer la barrière d'activation, car la valeur obtenue sur la base de seulement deux points de température n'est pas fiable. Nous notons qu'il peut encore y avoir des espèces d'hydrogène dans MoS_2, qui sont immobiles à 500 K, et qui sortent du cadre de l'étude actuelle. La mesure NRA réalisée dans le cadre de l'optimisation du nettoyage du MoS_2 a révélé la présence d'hydrogène jusqu'à 700 K. Les résultats de l'expérience XPS suggèrent que les atomes H dans MoS_2 sont stockés à la fois dans les groupes -SH, comme dans une structure parfaite, et au voisinage des lacunes de soufre, où l'énergie de liaison est plus élevée. Ils deviennent mobiles à différentes températures, et les données soutiennent l'idée que les lacunes accueillent plus d'atomes H que la matrice parfaite. Notons que les propriétés de diffusion de ces deux types d'hydrogène doivent être indiscernables après l'initiation de leur migration.

Les cristaux de MoS_2 qui ont été trempés dans l'eau ont montré la présence d'une quantité substantielle de molécules de H_2O physisorbées. Ils nécessitent la température la plus élevée parmi toutes les espèces pour être désorbés, bien qu'ils ne puissent pas pénétrer la matrice MoS_2 parfaite. Très probablement, ils se déposent autour des vides et d'autres défauts de volume suffisamment important, où une diffusion semblable à de l'eau liquide est possible. Reste à savoir s'il est régi par le mouvement et les col-

lisions des molécules H_2O dans le volume du vide, ou par le saut d'atomes d'hydrogène entre les atomes d'oxygène et de soufre. Pour la partie application du problème, il est important que l'eau liquide puisse accéder aux régions défectueuses de MoS_2, où des atomes de S plus exposés, qui sont considérés comme réactifs, pourraient être présents. Cet effet a probablement été observé dans nos expériences électrochimiques.

Les mesures de voltamétrie ont considéré non seulement MoS_2, mais aussi les poudres Mo_2C, qui sont toutes deux considérées comme modérément actives sur le plan catalytique. La poudre de MoS_2 qui a été infusée dans l'eau a montré une augmentation extraordinaire de l'efficacité catalytique, contrairement au Mo_2C. Cette amélioration peut être liée à la capacité de l'eau à se faufiler dans les joints de grains de MoS_2. En effet, si c'est le cas, alors l'eau aiderait à la fragmentation de la poudre, empêchant en même temps son agglomération naturelle, augmentant la quantité globale de sites actifs exposés. La structure des particules MoS_2 ne change pas après l'infusion d'eau, soutenant l'idée que les molécules H_2O ne peuvent pas être intercalées dans sa matrice.

6.3 Perspectives

L'étude présentée dans ce travail donne une vue d'ensemble de la diffusion de l'hydrogène dans MoS_2, ce qui est important pour obtenir une meilleure compréhension des processus se produisant lors de la catalyse de la réaction de dégagement d'hydrogène. Avec ces informations, il est maintenant temps de passer d'investigations plus théoriques à des recherches plus orientées vers les applications. Nous avons constaté que l'électrolyse entraîne une quantité importante de molécules H_2 piégées à l'intérieur du matériau. Cependant, nos simulations MD suggèrent que la barrière d'énergie pour la diffusion dans le plan n'est pas extrêmement grande. Avec de légères modifications structurelles, qui augmenteraient la distance entre les couches de MoS_2, ce type de mouvement peut être activé, et plus de H_2 pourrait être libéré de l'échantillon pendant l'électrolyse. Cette question devrait probablement être d'abord abordée via des études DFT, puis testée expérimentalement. Pour les particules MoS_2 nanométriques, en raison du rapport surface/volume élevé, il n'y aurait pas d'augmentation substantielle de H_2 généré, même si toutes nos hypothèses sont vraies. Cependant, si l'idée réussit, les poudres microscopiques pourraient se rapprocher de la taille nanométrique en termes

d'activité catalytique, et les premières sont plus stables et beaucoup plus faciles à produire.

Le rôle des défauts est parfois sous-estimé dans les études modernes de simulation numérique sur MoS_2, qui visent à révéler le mécanisme HER. Cependant, notre étude montre que divers défauts structuraux peuvent jouer un rôle important dans le mécanisme global de diffusion de l'hydrogène, qui est crucial pour l'étape de réaction de Tafel, et affecte également l'étape de Heyrovsky. Bien sûr, il existe des recherches spécialisées sur la fabrication de défauts dans le but d'améliorer l'activité catalytique HER [37], et elles sont largement connues. Cependant, les études, qui comparent l'énergétique des étapes de réaction de Volmer, Tafel et Heyrovsky, ont tendance à utiliser la structure parfaite de MoS_2 comme substrat [30, 38, 41]. Il serait important de faire une comparaison similaire sur une matrice MoS_2 défectueuse.

La cause du pic d'activité catalytique, atteint après infusion de poudre de MoS_2 dans l'eau, reste voilée. Néanmoins, une telle méthode pratique d'amélioration de l'efficacité du catalyseur pourrait être utilisée dans l'industrie pour produire des électrodes peu coûteuses et convenablement réactives, bien que certaines difficultés puissent être rencontrées en raison de la longue période de vieillissement. Il serait avantageux que cette période soit réduite à plusieurs jours ou heures. Pour y parvenir, d'autres expériences sont nécessaires, visant à découvrir la cause de l'augmentation de l'activité. Très probablement, deux facteurs principaux sont la fragmentation de la poudre lors de l'ultrasonification avec une absence supplémentaire d'agglomération due aux propriétés répulsives de l'eau, et l'adsorption lente de l'hydrogène de l'eau environnante et la migration des espèces adsorbées sur une ou deux couches de profondeur. Le premier facteur peut être facilement accéléré en exécutant l'ultrasonification pendant des durées plus longues ou en plusieurs cycles successifs. L'adsorption est plus complexe. Des températures élevées peuvent aider à accélérer le processus, mais pas au niveau de plusieurs heures. Si l'adsorption joue réellement le rôle principal, des modifications structurelles, probablement par dopage, peuvent être nécessaires pour atteindre le délai souhaité. Pour aborder la question de l'amélioration catalytique, il serait efficace de commencer par préparer une série d'échantillons (encres) à base de nano-poudre MoS_2 avec différentes séquences/procédures d'ultrasonification. Cela permettra d'évaluer l'influence de la fragmentation des poudres sans prendre trop de temps sur les processus de vieillissement. L'autre ensemble d'échantillons serait des poudres de MoS_2 infusées dans de l'eau pendant différentes périodes de temps. Ces encres ne doivent être

désonifiées brièvement qu'une seule fois lors de la préparation initiale, afin d'isoler l'effet de l'adsorption d'hydrogène sur les courbes de voltamétrie.

Bibliography

[1] Ashwin Rode, Tamma Carleton, Michael Delgado, Michael Greenstone, Trevor Houser, Solomon Hsiang, Andrew Hultgren, Amir Jina, Robert E. Kopp, Kelly E. McCusker, Ishan Nath, James Rising, and Jiacan Yuan. Estimating a social cost of carbon for global energy consumption. *Nature*, 598(7880):308–314, 2021.

[2] Myles R. Allen, David J. Frame, Chris Huntingford, Chris D. Jones, Jason A. Lowe, Malte Meinshausen, and Nicolai Meinshausen. Warming caused by cumulative carbon emissions towards the trillionth tonne. *Nature*, 458(7242):1163–1166, 2009.

[3] Martin Leduc, H. Damon Matthews, and Ramón de Elía. Regional estimates of the transient climate response to cumulative CO2 emissions. *Nature Climate Change*, 6(5):474–478, 2016.

[4] Matthew R. Smith and Samuel S. Myers. Impact of anthropogenic CO2 emissions on global human nutrition. *Nature Climate Change*, 8(9):834–839, 2018.

[5] European Commission. State of the Energy Union Report, including EU Climate Action Progress Report, 2021 and earlier.

[6] Yeru Liang, Chen-Zi Zhao, Hong Yuan, Yuan Chen, Weicai Zhang, Jia-Qi Huang, Dingshan Yu, Yingliang Liu, Maria-Magdalena Titirici, Yu-Lun Chueh, Haijun Yu, and Qiang Zhang. A review of rechargeable batteries for portable electronic devices. *InfoMat*, 1(1):6–32, 2019.

[7] Michel Armand, Peter Axmann, Dominic Bresser, Mark Copley, Kristina Edström, Christian Ekberg, Dominique Guyomard, Bernard Lestriez, Petr Novák, Martina Petranikova, Willy Porcher, Sigita

Trabesinger, Margret Wohlfahrt-Mehrens, and Heng Zhang. Lithium-ion batteries – Current state of the art and anticipated developments. *Journal of Power Sources*, 479:228708, 2020.

[8] Yang Jin, Sa Li, Akihiro Kushima, Xiaoquan Zheng, Yongming Sun, Jin Xie, Jie Sun, Weijiang Xue, Guangmin Zhou, Jiang Wu, Feifei Shi, Rufan Zhang, Zhi Zhu, Kangpyo So, Yi Cui, and Ju Li. Self-healing SEI enables full-cell cycling of a silicon-majority anode with a coulombic efficiency exceeding 99.9%. *Energy & Environmental Science*, 10(2):580–592, 2017.

[9] Marc A. Rosen and Seama Koohi-Fayegh. The prospects for hydrogen as an energy carrier: an overview of hydrogen energy and hydrogen energy systems. *Energy, Ecology and Environment*, 1(1):10–29, 2016.

[10] Ramin Moradi and Katrina M. Groth. Hydrogen storage and delivery: Review of the state of the art technologies and risk and reliability analysis. *International Journal of Hydrogen Energy*, 44(23):12254–12269, 2019.

[11] D. Stephens, P. Shawcross, G. Stout, E. Sullivan, J. Saunders, S. Risser, and J. Sayre. Lithium-ion battery safety issues for electric and plug-in hybrid vehicles. Technical Report DOT HS 812 418, Washington, DC: National Highway Traffic SafetyAdministration, 2017.

[12] Ram Gupta. *Hydrogen fuel : production, transport, and storage*. CRC Press, Boca Raton, 2009.

[13] Henning Lohse-Busch, Kevin Stutenberg, Michael Duoba, Xinyu Liu, Amgad Elgowainy, Michael Wang, Thomas Wallner, Brad Richard, and Martha Christenson. Automotive fuel cell stack and system efficiency and fuel consumption based on vehicle testing on a chassis dynamometer at minus 18 °C to positive 35 °C temperatures. *International Journal of Hydrogen Energy*, 45(1):861–872, 2020.

[14] Jun Chi and Hongmei Yu. Water electrolysis based on renewable energy for hydrogen production. *Chinese Journal of Catalysis*, 39(3):390–394, 2018.

[15] European Commission. Statistical Office of the European Union. *Energy balance sheets: 2020 edition.* Publications Office, 2020.

[16] Jason Marcinkoski, Jacob Spendelow, Adria Wilson, and Dimitrios Papageorgopoulos. Fuel Cell System Cost - 2015. Technical Report 15015, Department of Energy, United States of America, 2015.

[17] Xuefeng Ren, Qianyuan Lv, Lifen Liu, Bihe Liu, Yiran Wang, Anmin Liu, and Gang Wu. Current progress of Pt and Pt-based electrocatalysts used for fuel cells. *Sustainable Energy & Fuels*, 4(1):15–30, 2020.

[18] Yagya N. Regmi, Gregory R. Waetzig, Kyle D. Duffee, Samantha M. Schmuecker, James M. Thode, and Brian M. Leonard. Carbides of group IVA, VA and VIA transition metals as alternative HER and ORR catalysts and support materials. *Journal of Materials Chemistry A*, 3(18):10085–10091, 2015.

[19] Carlos G. Morales-Guio, Lucas-Alexandre Stern, and Xile Hu. Nanostructured hydrotreating catalysts for electrochemical hydrogen evolution. *Chemical Society Reviews*, 43(18):6555, 2014.

[20] Ya Yan, BaoYu Xia, Zhichuan Xu, and Xin Wang. Recent Development of Molybdenum Sulfides as Advanced Electrocatalysts for Hydrogen Evolution Reaction. *ACS Catalysis*, 4(6):1693–1705, 2014.

[21] Jesse D. Benck, Thomas R. Hellstern, Jakob Kibsgaard, Pongkarn Chakthranont, and Thomas F. Jaramillo. Catalyzing the Hydrogen Evolution Reaction (HER) with Molybdenum Sulfide Nanomaterials. *ACS Catalysis*, 4(11):3957–3971, 2014.

[22] Zhebo Chen, Dustin Cummins, Benjamin N. Reinecke, Ezra Clark, Mahendra K. Sunkara, and Thomas F. Jaramillo. Core–shell MoO3–MoS2 Nanowires for Hydrogen Evolution: A Functional Design for Electrocatalytic Materials. *Nano Letters*, 11(10):4168–4175, 2011. PMID: 21894935.

[23] Xiaoping Dai, Kangli Du, Zhanzhao Li, Hui Sun, Ying Yang, Wen Zhang, and Xin Zhang. Enhanced hydrogen evolution reaction on few–layer MoS2 nanosheets–coated functionalized carbon nanotubes. *International Journal of Hydrogen Energy*, 40(29):8877 – 8888, 2015.

[24] Xiaoxin Zou and Yu Zhang. Noble metal-free hydrogen evolution catalysts for water splitting. *Chem. Soc. Rev.*, 44:5148–5180, 2015.

[25] Sami Tuomi, Rut Guil-Lopez, and Tanja Kallio. Molybdenum carbide nanoparticles as a catalyst for the hydrogen evolution reaction and the effect of pH. *Journal of Catalysis*, 334:102–109, 2016.

[26] R. Murray and B. Evans. The thermal expansion of 2H-MoS2and 2H-WSe2between 10 and 320 K. *Journal of Applied Crystallography*, 12(3):312–315, 1979.

[27] E. Parthé and V. Sadogopan. The structure of dimolybdenum carbide by neutron diffraction technique. *Acta Crystallographica*, 16(3):202–205, 1963.

[28] Christopher J. Wright, Christopher Sampson, David Fraser, Richard B. Moyes, Peter B. Wells, and Christian Riekel. Hydrogen sorption by molybdenum sulphide catalysts. *Journal of the Chemical Society, Faraday Transactions 1: Physical Chemistry in Condensed Phases*, 76(0):1585, 1980.

[29] Timothy T. Yang, Teck Leong Tan, and Wissam A. Saidi. High Activity toward the Hydrogen Evolution Reaction on the Edges of MoS2-Supported Platinum Nanoclusters Using Cluster Expansion and Electrochemical Modeling. *Chemistry of Materials*, 32(3):1315–1321, 2020.

[30] Qing Tang and De-en Jiang. Mechanism of Hydrogen Evolution Reaction on 1T-MoS2 from First Principles. *ACS Catalysis*, 6(8):4953–4961, 2016.

[31] Tian Zhang, Houyu Zhu, Chen Guo, Shoufu Cao, Chi-Man Lawrence Wu, Zhaojie Wang, and Xiaoqing Lu. Theoretical investigation on the hydrogen evolution reaction mechanism at MoS2 heterostructures: the essential role of the 1T/2H phase interface. *Catalysis Science & Technology*, 10(2):458–465, 2020.

[32] M. Bée. *Quasielastic neutron scattering : principles and applications in solid state chemistry, biology and materials science*. Bristol and Philadelphia : Adam Hilger, 1988.

[33] Rolf Hempelmann. *Quasielastic Neutron Scattering and Solid State Diffusion*. Oxford University Press, 2000.

[34] U. Stuhr, T. Striffler, H. Wipf, H. Natter, B. Wettmann, S. Janssen, R. Hempelmann, and H. Hahn. An investigation of hydrogen diffusion in nanocrystalline Pd by neutron spectroscopy. *Journal of Alloys and Compounds*, 253-254:393–396, 1997.

[35] Daniel Merki, Stéphane Fierro, Heron Vrubel, and Xile Hu. Amorphous molybdenum sulfide films as catalysts for electrochemical hydrogen production in water. *Chem. Sci.*, 2(7):1262–1267, 2011.

[36] Damien Voiry, Maryam Salehi, Rafael Silva, Takeshi Fujita, Mingwei Chen, Tewodros Asefa, Vivek B. Shenoy, Goki Eda, and Manish Chhowalla. Conducting mos2 nanosheets as catalysts for hydrogen evolution reaction. *Nano Lett.*, 13:6222 – 6227, 2013.

[37] Yixin Ouyang, Chongyi Ling, Qian Chen, Zilu Wang, Li Shi, and Jinlan Wang. Activating Inert Basal Planes of MoS2 for Hydrogen Evolution Reaction through the Formation of Different Intrinsic Defects. *Chemistry of Materials*, 28(12):4390–4396, 2016.

[38] Charlie Ruffman, Calum K. Gordon, Egill Skúlason, and Anna L. Garden. Mechanisms and Potential-Dependent Energy Barriers for Hydrogen Evolution on Supported MoS2 Catalysts. *The Journal of Physical Chemistry C*, 124(31):17015–17026, 2020.

[39] Ni Zhao, Lu Wang, Zixiang Zhang, and Youyong Li. Activating the MoS2 Basal Planes for Electrocatalytic Hydrogen Evolution by 2H/1T′ Structural Interfaces. *ACS Applied Materials & Interfaces*, 11(45):42014–42020, 2019.

[40] Yang Cao. Roadmap and Direction toward High-Performance MoS2 Hydrogen Evolution Catalysts. *ACS Nano*, 15(7):11014–11039, 2021.

[41] Wang Li, Guihua Liu, Jingde Li, Yanji Wang, Luis Ricardez-Sandoval, Yongguang Zhang, and Zisheng Zhang. Hydrogen evolution reaction mechanism on 2H-MoS2 electrocatalyst. *Applied Surface Science*, 498:143869, 2019.

[42] Yun An, Agnieszka Kuc, Petko Petkov, Marcelo Lozada-Hidalgo, and Thomas Heine. On the chemistry and diffusion of hydrogen in the interstitial space of layered crystals h -BN, MoS_2 , and graphite. *Small*, 15(43):1901722, 2019.

[43] Yong Pan. Role of S-S interlayer spacing on the hydrogen storage mechanism of MoS 2. *International Journal of Hydrogen Energy*, 43(6):3087–3091, 2018.

[44] S. Hu, M. Lozada-Hidalgo, F. C. Wang, A. Mishchenko, F. Schedin, R. R. Nair, E. W. Hill, D. W. Boukhvalov, M. I. Katsnelson, R. A. W. Dryfe, I. V. Grigorieva, H. A. Wu, and A. K. Geim. Proton transport through one-atom-thick crystals. *Nature*, 516(7530):227–230, 2014.

[45] F. Traeger, M. Kauer, Ch. Wöll, D. Rogalla, and H.-W. Becker. Analysis of surface, subsurface, and bulk hydrogen in ZnO using nuclear reaction analysis. *Phys. Rev. B*, 84:075462, 2011.

[46] Toshio Sakurai, M. J. Cardillo, and H. D. Hagstrum. Kinetics of the generation of atomic hydrogen and its adsorption on Si(110). *Journal of Vacuum Science and Technology*, 14(1):397–399, 1977.

[47] G. Schulze and M. Henzler. Adsorption of atomic hydrogen on clean cleaved silicon (111). *Surface Science*, 124(2-3):336–350, 1983.

[48] G. E. Bacon. *Neutron diffraction*. Clarendon Press, Oxford England, 1975.

[49] Stefano Caporali, Francesco Grazzi, Filomena Salvemini, Ulf Garbe, Steven Peetermans, and Giovanni Pratesi. Structural Characterization of Iron Meteorites through Neutron Tomography. *Minerals*, 6(1):14, 2016.

[50] Oliver Wrede, Yvonne Reimann, Stefan Lülsdorf, Daniel Emmrich, Kristina Schneider, Andreas Josef Schmid, Diana Zauser, Yvonne Hannappel, André Beyer, Ralf Schweins, Armin Gölzhäuser, Thomas Hellweg, and Thomas Sottmann. Volume phase transition kinetics of smart N-n-propylacrylamide microgels studied by time-resolved pressure jump small angle neutron scattering. *Scientific Reports*, 8(1), 2018.

[51] T. Jenke, G. Cronenberg, J. Burgdörfer, L. A. Chizhova, P. Geltenbort, A. N. Ivanov, T. Lauer, T. Lins, S. Rotter, H. Saul, U. Schmidt, and H. Abele. Gravity Resonance Spectroscopy Constrains Dark Energy and Dark Matter Scenarios. *Physical Review Letters*, 112(15):151105, 2014.

[52] Y. Drees, D. Lamago, A. Piovano, and A. C. Komarek. Hour-glass magnetic spectrum in a stripeless insulating transition metal oxide. *Nature Communications*, 4(1), 2013.

[53] Léon Van Hove. Correlations in Space and Time and Born Approximation Scattering in Systems of Interacting Particles. *Physical Review*, 95(1):249–262, 1954.

[54] Varley F. Sears. Neutron scattering lengths and cross sections. *Neutron News*, 3(3):26–37, 1992.

[55] N. Wakabayashi, H. G. Smith, and R. M. Nicklow. Lattice dynamics of hexagonal MoS2 studied by neutron scattering. *Physical Review B*, 12(2):659–663, 1975.

[56] C. Ataca, M. Topsakal, E. Aktürk, and S. Ciraci. A Comparative Study of Lattice Dynamics of Three- and Two-Dimensional MoS2. *The Journal of Physical Chemistry C*, 115(33):16354–16361, aug 2011.

[57] C. T. Chudley and R. J. Elliott. Neutron Scattering from a Liquid on a Jump Diffusion Model. *Proceedings of the Physical Society*, 77(2):353–361, 1961.

[58] Peter L. Hall and D.K. Ross. Incoherent neutron scattering functions for random jump diffusion in bounded and infinite media. *Molecular Physics*, 42(3):673–682, 1981.

[59] V. F. Sears. Cold neutron scattering by molecular liquids: iii. methane. *Canadian Journal of Physics*, 45(2):237–254, 1967.

[60] M. Bée. A physical insight into the elastic incoherent structure factor. *Physica B: Condensed Matter*, 182(4):323 – 336, 1992. Quasielastic Neutron Scattering.

[61] F. Volino and A.J. Dianoux. Neutron incoherent scattering law for diffusion in a potential of spherical symmetry: general formalism and application to diffusion inside a sphere. *Molecular Physics*, 41(2):271–279, 1980.

[62] V. F. Sears. Theory of cold neutron scattering by homonuclear diatomic liquids: II. hindered rotation. *Canadian Journal of Physics*, 44(6):1299–1311, 1966.

[63] T. R. Prisk, M. S. Bryan, and P. E. Sokol. Diffusive and rotational dynamics of condensed n-H2confined in MCM-41. *Phys. Chem. Chem. Phys.*, 16(33):17960–17974, 2014.

[64] Alexander J. O'Malley and C. Richard A. Catlow. Sorbate Dynamics in Zeolite Catalysts. In *Neutron Scattering - Applications in Biology, Chemistry, and Materials Science*, pages 349–401. Elsevier, 2017.

[65] I. Calvo-Almazán, S. Miret-Artés, and P. Fouquet. A theoretical study of rotational and translational diffusion dynamics of molecules with a six-fold point symmetry adsorbed on a hexagonal lattice by neutron scattering. *Journal of Physics: Condensed Matter*, 24(10):104007, 2012.

[66] H. Jobic. Observation of single-file diffusion in a MOF. *Physical Chemistry Chemical Physics*, 18(26):17190–17195, 2016.

[67] S.-H. Chen, P. Gallo, F. Sciortino, and P. Tartaglia. Molecular-dynamics study of incoherent quasielastic neutron-scattering spectra of supercooled water. *Phys. Rev. E*, 56:4231–4243, 1997.

[68] Andrew N. Vavreck and William Thompson. Some novel infinite series of spherical bessel functions. *Quarterly of Applied Mathematics*, 42(3):321–324, 1984.

[69] L. E. Bove, S. Klotz, Th. Strässle, M. Koza, J. Teixeira, and A. M. Saitta. Translational and Rotational Diffusion in Water in the Gigapascal Range. *Physical Review Letters*, 111(18):185901, 2013.

[70] Shathabish NaraseGowda, Craig M. Brown, Madhusudan Tyagi, Timothy Jenkins, and Tabbetha A. Dobbins. Quasi-Elastic Neutron Scattering Studies of Hydrogen Dynamics for Nanoconfined NaAlH4. *The Journal of Physical Chemistry C*, 120(27):14863–14873, 2016.

[71] James F. Ziegler, M. D. Ziegler, and J. P. Biersack. SRIM - The stopping and range of ions in matter (2010). *Nuclear Instruments and Methods In Physics Research Section B-Beam Interactions with Materials and Atoms*, 268(11-12):1818–1823, 2010. 19th International Conference on Ion Beam Analysis, Univ Cambridge, Cambridge, ENGLAND, SEP 07-11, 2009.

[72] Hans-Werner Becker and Detlef Rogalla. *Nuclear Reaction Analysis*, pages 315–336. Springer International Publishing, Cham, 2016.

[73] T. Liu, I. Temprano, D. A. King, S. M. Driver, and S. J. Jenkins. Epitaxial growth of few-layer MoS2(0001) on FeS2{100}. *Chemical Communications*, 51(3):537–540, 2015.

[74] Cedric Powell. Nist electron inelastic-mean-free-path database , nist standard reference database 71, 1999.

[75] J.J. Yeh and I. Lindau. Atomic subshell photoionization cross sections and asymmetry parameters: $1 \leq Z \leq 103$. *Atomic Data and Nuclear Data Tables*, 32(1):1 – 155, 1985.

[76] Noémie Elgrishi, Kelley J. Rountree, Brian D. McCarthy, Eric S. Rountree, Thomas T. Eisenhart, and Jillian L. Dempsey. A Practical Beginner's Guide to Cyclic Voltammetry. *Journal of Chemical Education*, 95(2):197–206, 2017.

[77] P. Hohenberg and W. Kohn. Inhomogeneous Electron Gas. *Physical Review*, 136(3B):B864–B871, 1964.

[78] Kieron Burke and Lucas O. Wagner. DFT in a nutshell. *International Journal of Quantum Chemistry*, 113(2):96–101, 2012.

[79] Musa Ozboyaci, Daria B. Kokh, Stefano Corni, and Rebecca C. Wade. Modeling and simulation of protein–surface interactions: achievements and challenges. *Quarterly Reviews of Biophysics*, 49, 2016.

[80] Daan Frenkel and Berend Smit. *Understanding Molecular Simulation: From Algorithms to Applications*. Elsevier, 2002.

[81] Adri C. T. van Duin, Siddharth Dasgupta, Francois Lorant, and William A. Goddard. ReaxFF: A Reactive Force Field for Hydrocarbons. *The Journal of Physical Chemistry A*, 105(41):9396–9409, sep 2001.

[82] Thomas P Senftle, Sungwook Hong, Md Mahbubul Islam, Sudhir B Kylasa, Yuanxia Zheng, Yun Kyung Shin, Chad Junkermeier, Roman Engel-Herbert, Michael J Janik, Hasan Metin Aktulga, Toon Verstraelen, Ananth Grama, and Adri C T van Duin. The ReaxFF reactive force-field: development, applications and future directions. *npj Computational Materials*, 2(1), 2016.

[83] Thomas E. Gartner and Arthi Jayaraman. Modeling and Simulations of Polymers: A Roadmap. *Macromolecules*, 52(3):755–786, 2019.

[84] M. P. Allen. *Computer simulation of liquids*. Clarendon Press Oxford University Press, Oxford England New York, 1987.

[85] M.A. González. Force fields and molecular dynamics simulations. *École thématique de la Société Française de la Neutronique*, 12:169–200, 2011.

[86] Thomas A. Halgren. Merck molecular force field. I. Basis, form, scope, parameterization, and performance of MMFF94. *Journal of Computational Chemistry*, 17(5-6):490–519, 1996.

[87] A. K. Rappe, C. J. Casewit, K. S. Colwell, W. A. Goddard, and W. M. Skiff. UFF, a full periodic table force field for molecular mechanics and molecular dynamics simulations. *Journal of the American Chemical Society*, 114(25):10024–10035, 1992.

[88] Wendy D. Cornell, Piotr Cieplak, Christopher I. Bayly, Ian R. Gould, Kenneth M. Merz, David M. Ferguson, David C. Spellmeyer, Thomas Fox, James W. Caldwell, and Peter A. Kollman. A Second Generation Force Field for the Simulation of Proteins, Nucleic Acids, and Organic Molecules. *Journal of the American Chemical Society*, 117(19):5179–5197, 1995.

[89] A. D. MacKerell, D. Bashford, M. Bellott, R. L. Dunbrack, J. D. Evanseck, M. J. Field, S. Fischer, J. Gao, H. Guo, S. Ha, D. Joseph-McCarthy, L. Kuchnir, K. Kuczera, F. T. K. Lau, C. Mattos, S. Michnick, T. Ngo, D. T. Nguyen, B. Prodhom, W. E. Reiher, B. Roux, M. Schlenkrich, J. C. Smith, R. Stote, J. Straub, M. Watanabe, J. Wiórkiewicz-Kuczera, D. Yin, and M. Karplus. All-Atom Empirical Potential for Molecular Modeling and Dynamics Studies of Proteins. *The Journal of Physical Chemistry B*, 102(18):3586–3616, 1998.

[90] J. R. Maple, M.-J. Hwang, T. P. Stockfisch, U. Dinur, M. Waldman, C. S. Ewig, and A. T. Hagler. Derivation of class II force fields. i. methodology and quantum force field for the alkyl functional group and alkane molecules. *Journal of Computational Chemistry*, 15(2):162–182, 1994.

[91] H. Sun. COMPASS: An ab Initio Force-Field Optimized for Condensed-Phase ApplicationsOverview with Details on Alkane and Benzene Compounds. *The Journal of Physical Chemistry B*, 102(38):7338–7364, 1998.

[92] H. J. C. Berendsen, J. P. M. Postma, W. F. van Gunsteren, A. DiNola, and J. R. Haak. Molecular dynamics with coupling to an external bath. *The Journal of Chemical Physics*, 81(8):3684–3690, 1984.

[93] Hans C. Andersen. Molecular dynamics simulations at constant pressure and/or temperature. *The Journal of Chemical Physics*, 72(4):2384–2393, 1980.

[94] Shuichi Nosé. A unified formulation of the constant temperature molecular dynamics methods. *The Journal of Chemical Physics*, 81(1):511–519, 1984.

[95] William G. Hoover. Canonical dynamics: Equilibrium phase-space distributions. *Physical Review A*, 31(3):1695–1697, 1985.

[96] Alex A. Samoletov, Carl P. Dettmann, and Mark A. J. Chaplain. Thermostats for "Slow" Configurational Modes. *Journal of Statistical Physics*, 128(6):1321–1336, 2007.

[97] Alexei Nefedov and Christof Wöll. Advanced Applications of NEXAFS Spectroscopy for Functionalized Surfaces. In *Surface Science Techniques*, pages 277–303. Springer Berlin Heidelberg, 2013.

[98] D. A. Shirley. High-Resolution X-Ray Photoemission Spectrum of the Valence Bands of Gold. *Phys. Rev. B*, 5:4709–4714, 1972.

[99] Heinz Maier-Leibnitz Zentrum. TOFTOF: Cold neutron time-of-flight spectrometer. *Journal of large-scale research facilities*, 1:A15, 2015.

[100] O. Arnold, J.C. Bilheux, J.M. Borreguero, A. Buts, S.I. Campbell, L. Chapon, M. Doucet, N. Draper, R. Ferraz Leal, M.A. Gigg, V.E. Lynch, A. Markvardsen, D.J. Mikkelson, R.L. Mikkelson, R. Miller, K. Palmen, P. Parker, G. Passos, T.G. Perring, P.F. Peterson, S. Ren, M.A. Reuter, A.T. Savici, J.W. Taylor, R.J. Taylor, R. Tolchenov, W. Zhou, and J. Zikovsky. Mantid—Data analysis and visualization

package for neutron scattering and μSR experiments. *Nuclear Instruments and Methods in Physics Research Section A: Accelerators, Spectrometers, Detectors and Associated Equipment*, 764:156 – 166, 2014.

[101] Franziska Traeger and Peter Fouquet. Hydrogen diffusion in MoS_2, 2016.

[102] B. Farago. IN11C, medium-resolution multidetector extension of the IN11 NSE spectrometer at the ILL. *Physica B*, 241-243:113–116, 1998.

[103] M. P. Seah and W. A. Dench. Quantitative electron spectroscopy of surfaces: A standard data base for electron inelastic mean free paths in solids. *Surface and Interface Analysis*, 1(1):2–11, 1979.

[104] Ganta D., Sinha S., and Haasch Richard T. 2-D Material Molybdenum Disulfide Analyzed by XPS. *Surface Science Spectra*, 21(1):19–27, 2014.

[105] J.-G. Choi and L.T. Thompson. XPS study of as-prepared and reduced molybdenum oxides. *Applied Surface Science*, 93(2):143 – 149, 1996.

[106] Lena Trotochaud, Ashley R. Head, Sven Pletincx, Osman Karslıoğlu, Yi Yu, Astrid Waldner, Line Kyhl, Tom Hauffman, Herman Terryn, Bryan Eichhorn, and Hendrik Bluhm. Water Adsorption and Dissociation on Polycrystalline Copper Oxides: Effects of Environmental Contamination and Experimental Protocol. *The Journal of Physical Chemistry B*, 122(2):1000–1008, 2018. PMID: 29215283.

[107] Dhananjay I. Patel, Dhruv Shah, Stephan Bahr, Paul Dietrich, Michael Meyer, Andreas Thißen, and Matthew R. Linford. Water vapor, by near-ambient pressure XPS. *Surface Science Spectra*, 26(1):014026, 2019.

[108] Koichi Momma and Fujio Izumi. *VESTA3* for three-dimensional visualization of crystal, volumetric and morphology data. *Journal of Applied Crystallography*, 44(6):1272–1276, 2011.

[109] Emanuel Bahn, Leidy A. Hoyos Giraldo, Vitalii Kuznetsov, Irene Calvo-Almazán, Mohamed Zbiri, Michael M. Koza, Thomas C. Hansen, Paul F. Henry, Alain Lapp, Stephanie Pouget, Monica Mesa, and Peter Fouquet. Ultra-fast diffusion of hydrogen in a novel mesoporous N-doped carbon. *Carbon*, 166:307 – 315, 2020.

[110] K. S. Singwi and Alf Sjölander. Diffusive Motions in Water and Cold Neutron Scattering. *Phys. Rev.*, 119:863–871, 1960.

[111] Graham Andrew P., Menzel Alexander, and Toennies J. Peter. Quasielastic helium atom scattering measurements of microscopic diffusional dynamics of H and D on the Pt(111) surface. *The Journal of Chemical Physics*, 111(4):1676–1685, 1999.

[112] Marcelo Carmo, David L. Fritz, Jürgen Mergel, and Detlef Stolten. A comprehensive review on PEM water electrolysis. *International Journal of Hydrogen Energy*, 38(12):4901 – 4934, 2013.

[113] F. Mezei, editor. *Neutron Spin Echo*, volume 128 of *Lecture Notes in Physics*. Springer, Berlin, 1980.

[114] Franziska Traeger, Peter Fouquet, Michael Marek Koza, and Vitalii Kuznetsov. Diffusion of water and hydrogen in mos2 (single crystal and powder), 2020.

[115] D. Brochier. Crysostat à température variable pour mesures neutroniques ou optiques. Technical Report 77/74, Institut Laue-Langevin, Grenoble, 1977.

[116] Huai Sun, Stephen J. Mumby, Jon R. Maple, and Arnold T. Hagler. An ab Initio CFF93 All-Atom Force Field for Polycarbonates. *Journal of the American Chemical Society*, 116(7):2978–2987, 1994.

[117] Alireza Ostadhossein, Ali Rahnamoun, Yuanxi Wang, Peng Zhao, Sulin Zhang, Vincent H. Crespi, and Adri C. T. van Duin. ReaxFF Reactive Force-Field Study of Molybdenum Disulfide (MoS2. *The Journal of Physical Chemistry Letters*, 8(3):631–640, jan 2017.

[118] Mostafa Hasanian, Bohayra Mortazavi, Alireza Ostadhossein, Timon Rabczuk, and Adri C.T. van Duin. Hydrogenation and defect formation control the strength and ductility of MoS2 nanosheets: Reactive molecular dynamics simulation. *Extreme Mechanics Letters*, 22:157–164, jul 2018.

[119] Roscoe G. Dickinson and Linus Pauling. The crystal structure of molybdenite. *Journal of the American Chemical Society*, 45(6):1466–1471, 1923.

[120] U Gelius, P F Hedén, J Hedman, B J Lindberg, R Manne, R Nordberg, C Nordling, and K Siegbahn. Molecular Spectroscopy by Means of ESCA III.Carbon compounds. *Physica Scripta*, 2(1-2):70–80, 1970.

[121] Line S. Byskov, Mikkel Bollinger, Jens K. Nørskov, Bjerne S. Clausen, and Henrik Topsøe. Molecular aspects of the H_2 activation on MoS_2 based catalysts - the role of dynamic surface arrangements. *Journal of Molecular Catalysis A: Chemical*, 163(1):117–122, 2000.

[122] Vitalii Kuznetsov, Wiebke Lohstroh, Detlef Rogalla, Hans-Werner Becker, Thomas Strunskus, Alexei Nefedov, Eva Kovacevic, Franziska Traeger, and Peter Fouquet. Neutron spectroscopy study of the diffusivity of hydrogen in MoS2. *Physical Chemistry Chemical Physics*, 23(13):7961–7973, 2021.

[123] C. Frondel and F.E. Wickman. Molybdenite polytypes in theory and occurrence; pt. 2, some naturally occurring polytypes of molybdenite. *American Mineralogist*, 55(11-12):1857–1875, 1970.